

ABSTRACT

Title of dissertation: **SEARCH FOR QUANTUM GRAVITY
WITH ICECUBE AND HIGH ENERGY
ATMOSPHERIC NEUTRINOS**

Warren Huelsnitz, Doctor of Philosophy, 2010

Dissertation directed by: **Professor Kara Hoffman
Department of Physics**

IceCube is a 1 km³ neutrino telescope nearing completion in the South Pole Ice. Designed to detect astrophysical neutrinos from 100 GeV to about an EeV, it will contribute to the fields of high energy astrophysics, particle physics, and neutrino physics. This analysis looks at the flux of atmospheric neutrinos detected by IceCube while it operated in a partially-completed, 40-string configuration, from April 2008 to May 2009. From this data set, a sample of about 20,000 up-going atmospheric muon neutrino events with negligible background was extracted using Boosted Decision Trees. A discrete Fourier transform method was used to constrain a directional asymmetry in right ascension. Constraints on certain interaction coefficients from the Standard Model Extension were improved by three orders of magnitude, relative to prior experiments. The event sample was also used to unfold the atmospheric neutrino spectrum at its point of origin, and seasonal and systematic variations in the atmospheric muon neutrino flux were studied. A likelihood method was developed to constrain perturbations to the energy and zenith angle

dependence of the atmospheric muon neutrino flux that could be due to Lorentz-violating oscillations or decoherence of neutrino flavor. Such deviations could be a signature of quantum gravity in the neutrino sector. The impact of systematic uncertainties in the neutrino flux and in the detector response on such a likelihood analysis were examined. Systematic uncertainties that need to be reduced in order to use a two-dimensional likelihood analysis to constrain phenomenological models for Lorentz or CPT violating neutrino oscillations were identified.

SEARCH FOR QUANTUM GRAVITY WITH ICECUBE
AND HIGH ENERGY ATMOSPHERIC NEUTRINOS

by

Warren Huelsnitz

Dissertation submitted to the Faculty of the Graduate School of the
University of Maryland, College Park in partial fulfillment
of the requirements for the degree of
Doctor of Philosophy
2010

Advisory Committee:
Professor Kara Hoffman, Chair/Advisor
Professor Gregory Sullivan
Professor Jordan Goodman
Professor Theodore Jacobson
Professor William McDonough

© Copyright by
Warren Huelsnitz
2010

Dedication

I dedicate this work to Samuel, whose curiosity and passion for knowledge has been an inspiration to me and will surely lead him to great discoveries.

Acknowledgments

First and foremost, I would like to thank my wife, Michelle. Without her support and encouragement, I would not have pursued my passion in physics. I would also like to thank my advisor, Kara Hoffman, for providing the opportunity to work on this incredibly fascinating experiment. In addition to giving me the flexibility to pursue my own interests and ideas, she created several opportunities for me to broaden my experience and knowledge base. She also steered me towards what looks like will be a very interesting and challenging Post-doctoral experience.

I would like to thank Greg Sullivan and Jordan Goodman, for the professional development and career advice they provided over the past few years, as well as the interesting, and at times challenging, questions they asked. Without Erik Blaufuss, I would still be stuck in some sort of Linux hell. So I certainly owe him my gratitude, for always being available and quick with solutions to computing problems. I also want to thank Alex Olivas and Henrike Wissing for discussions of the science, and support with simulation. I want to express my appreciation for my fellow grad students: Pete Redl, Kevin Meagher, Brian Christy, and Phil Roth. These guys were incredibly helpful, and tolerant of my many questions.

This analysis is the cumulative result of the efforts of the entire collaboration. However, there have been several people who were singularly helpful with key requirements, or at key moments when I needed a push over a certain obstacle to keep making progress. These people include Jon Dumm, Sean Grullon, Paolo Desiati, David Boersma, and Dima Chirkin. Tom Gaisser has been enormously helpful in

supporting my work, and in putting the science in context. Without the insight and vision of Francis Halzen, there probably would not have been an IceCube experiment for me to be a part of. Francis' goal to squeeze the maximum amount of science as possible out of IceCube inspired me to take on such an ambitious topic as this for my dissertation.

I would like to acknowledge financial support from the University of Maryland Graduate School and the Department of Physics, in the form of research assistantships and fellowships.

Table of Contents

List of Figures	viii
List of Abbreviations	xiii
1 Introduction	1
1.1 Neutrinos and Quantum Gravity Phenomenology	1
1.2 Neutrinos and the IceCube Neutrino Observatory	5
2 Neutrino Particle Physics and Astrophysics	10
2.1 Neutrinos In and Beyond the Standard Model	10
2.1.1 Neutrino Oscillations	11
2.1.2 Standard Model Extension	18
2.2 Cosmic Rays	19
2.2.1 Conventional Atmospheric Neutrino Flux	26
2.2.2 Prompt Atmospheric Neutrino Flux	27
3 Phenomenology	32
3.1 Violation of Lorentz Invariance	32
3.2 Decoherence	39
3.3 Violation of Rotational Invariance	45
3.4 Additional Models	50
3.4.1 CPT Violating Oscillation of Antineutrinos	50
3.4.2 Bicycle Model	52
3.5 Constraining Quantum Gravity With Astrophysical Neutrinos	53
4 The IceCube Neutrino Observatory	57
4.1 Construction	60
4.2 Digital Optical Modules	61
4.3 Electronics and Data Acquisition	63
4.4 Calibration and Verification	64
4.4.1 Timing	64
4.4.2 Digital Optical Modules	64
4.4.3 Geometry	66
4.5 Ice Properties	67
5 Neutrino Detection with IceCube	71
5.1 Neutrino-Nucleon Cross Sections	71
5.2 Cherenkov Radiation	74
5.3 Muon Propagation and Energy Loss	75
5.4 Event Signatures	77
5.5 Triggering	79
5.6 Filtering	80
5.7 Event Reconstruction	81

5.7.1	Waveform Calibration	81
5.7.2	DOM Launch Cleaning	82
5.7.3	Feature Extraction	83
5.7.4	Time Window Cleaning	83
5.7.5	LineFit	84
5.7.6	Maximum Likelihood Reconstructions	85
5.7.7	Single Photoelectron Fit	88
5.7.8	Multiple Photoelectron Fit	88
5.7.9	PhotoRec	89
5.7.10	Paraboloid	90
5.7.11	Bayesian	90
5.7.12	Umbrella	91
5.7.13	SplitTrack	91
5.7.14	Additional Cut Parameters	92
6	Event Selection	94
6.1	Backgrounds	94
6.2	Simulation	95
6.2.1	Atmospheric Muons	95
6.2.2	Atmospheric Neutrinos	96
6.2.3	Light Propagation	97
6.2.4	Detector Hardware	97
6.2.5	Neutrino Flux Weighting	98
6.3	Muon Filter	99
6.4	Data Processing Cuts	101
6.5	Pre-selection Cuts	101
6.6	Boosted Decision Trees	102
6.6.1	Training, Testing, and Choice of BDT Cut Values.	105
6.7	Final Event Selection	107
6.7.1	Effective Area	112
6.7.2	Final Event Sample	113
7	Analysis Methodology	116
7.1	Likelihood Ratio Test	116
7.2	Discrete Fourier Transform Analysis	124
7.3	Unfolding of the Atmospheric Neutrino Spectrum	128
8	Systematic Uncertainties	132
8.1	Uncertainties in Atmospheric Neutrino Flux Predictions	132
8.2	Uncertainties in DOM Sensitivity and Ice Properties	133
8.3	Other Sources of Uncertainty	135
8.4	Summary of Nuisance Parameters	136
8.5	Additional Uncertainty Evidenced by Data/Simulation Mismatch	136
8.6	Seasonal Variability in the Data	143
8.7	Other Possible New Physics Effects: Neutrino Cross Sections	156

9	Results	160
9.1	Atmospheric Neutrino Flux Unfolding	160
9.2	DFT Analysis: Violation of Rotational Invariance	171
9.3	Likelihood Analyses	174
9.3.1	Atmospheric Neutrino Spectrum	174
9.3.2	VLI Models	177
9.3.3	Decoherence Models	180
10	Conclusions and Outlook	182
10.1	Summary of Results	182
10.2	Future Prospects and Refinements to the Methodology	184
	Bibliography	185

List of Figures

2.1	Schematic of neutrino production, propagation, and detection.	14
2.2	Possible mass spectra for neutrino mass and flavor eigenstates.	15
2.3	Atmospheric muon neutrino survival probability for mass-induced oscillations.	17
2.4	Energy dependence and composition of cosmic ray primaries.	20
2.5	All-particle spectrum from air shower measurements.	22
2.6	Particle production in cosmic ray air shower.	24
2.7	Seasonal variation in atmospheric muon flux.	25
2.8	Survival probability as neutrinos propagate through the Earth.	27
2.9	Energy and zenith dependence of conventional atmospheric muon neutrino flux.	28
2.10	Theoretical predictions for the prompt atmospheric muon neutrino flux.	29
2.11	Components of the muon neutrino flux in IceCube.	30
2.12	Energy and zenith dependence of atmospheric muon neutrino flux, conventional and prompt combined.	31
3.1	Atmospheric muon neutrino survival probability for $n = 1$ VLI model.	36
3.2	Predicted sensitivity to $n = 1$ VLI oscillations.	37
3.3	Predicted sensitivity to $n = 1$ VLI oscillations after an additional cut at $\cos \theta_Z < -0.12$	38
3.4	Predicted sensitivity to $n = 2$ VLI oscillations.	38
3.5	Predicted sensitivity to $n = 3$ VLI oscillations.	39
3.6	Limits for VLI oscillations from prior experiments.	40
3.7	Atmospheric muon neutrino survival probability for $n = 2$ decoherence model.	43
3.8	Atmospheric muon neutrino survival probability for $n = 2$ decoherence model.	44

3.9	Atmospheric muon neutrino survival probability for $n = 2$ decoherence model.	44
3.10	Predicted sensitivity for the $n = 2$ decoherence model.	46
3.11	Predicted sensitivity for the $n = 2$ decoherence model after an additional cut at $\cos \theta_Z < -0.12$	46
3.12	Predicted sensitivity for the $n = 1$ decoherence model.	47
3.13	Predicted sensitivity for the $n = 3$ decoherence model.	47
3.14	Atmospheric muon neutrino survival probability for the vector model.	49
3.15	Atmospheric muon neutrino survival probability for the vector model.	49
3.16	Atmospheric muon neutrino survival probability for CPTV oscillations of antineutrinos.	51
3.17	Predicted sensitivity to CPTV oscillations of antineutrinos.	52
3.18	Atmospheric muon neutrino survival probability for the bicycle model.	54
3.19	Atmospheric muon neutrino survival probability for the bicycle model.	54
3.20	Predicted sensitivity to bicycle model.	55
4.1	IceCube Neutrino Observatory and its component arrays.	58
4.2	Digital Optical Module (DOM).	63
4.3	Optical properties of deep South Pole ice.	69
4.4	Scattering and absorption coefficients as functions of depth.	70
5.1	CC and NC neutrino-nucleon interactions.	72
5.2	CC and NC cross sections.	73
5.3	Cherenkov light in the IceCube Neutrino Observatory.	75
5.4	Energy loss mechanisms for muons.	76
5.5	Up-going muon neutrino event in IceCube.	78
5.6	Horizontal muon neutrino event in IceCube.	79

5.7	Reconstruction of photoelectron pulses from waveform data.	83
5.8	Geometry of the signal detection process.	86
5.9	CPandel PDF for two values of the time resolution parameter.	87
6.1	Schematic view of a decision tree.	103
6.2	Efficiency of the boosted decision trees.	108
6.3	Output of the boosted decision trees.	109
6.4	Progression of event rate for various cut levels for simulated atmospheric neutrinos.	110
6.5	Progression of event rate for various cut levels for data.	111
6.6	Ratio, data to simulation, as a function of BDT cut value.	111
6.7	Final effective area for up-going muon neutrinos as a function of neutrino energy.	112
6.8	Energy reach of final neutrino sample.	113
6.9	Number of events in each bin of the observables histogram.	114
6.10	Distributions of observables for likelihood analysis.	115
6.11	Distributions of observables for likelihood analysis after re-binning.	115
7.1	R-values, under the $n = 1$ VLI model, with no systematic uncertainties.	120
7.2	R-values, under the $n = 1$ VLI model, with systematic uncertainties.	121
7.3	R-values, under the $n = 2$ decoherence model, with no systematic uncertainties.	122
7.4	R-values, under the $n = 2$ decoherence model, with systematic uncertainties.	123
7.5	Predicted acceptance regions for the $n = 1$ VLI model.	125
7.6	Predicted acceptance regions for the $n = 2$ decoherence model.	126
8.1	Excess of horizontal events in data.	138

8.2	Bin-wise data/simulation comparison.	139
8.3	Bin-wise data/simulation comparison after additional zenith cut.	140
8.4	Z component of the COG variable for horizontal events in data and simulation.	141
8.5	Bin-wise data/simulation comparison after forward fit.	144
8.6	Bin-wise data/simulation comparison with highlighted regions of systematic disagreement.	145
8.7	Monthly variability in event rate.	147
8.8	dE/dX and $\cos\theta_Z$ distributions for each of four seasons.	147
8.9	Azimuth distributions for each of four seasons, for the $\cos\theta_Z$ band -0.4 to -0.5	148
8.10	RA distributions for each of four seasons, for the $\cos\theta_Z$ band -0.4 to -0.5	149
8.11	Bin-wise comparison of data in each season to entire year of data.	151
8.12	Statistical significance for bin-wise, seasonal comparison of data.	152
8.13	Bin-wise comparison of data in each season to simulation.	153
8.14	Statistical significance for bin-wise, seasonal comparison of data to simulation.	154
8.15	E_ν and $\cos\theta_Z$ distributions for each of five South Pole atmospheres, from CORSIKA.	156
8.16	Bin-wise comparison of the neutrino event rates from the July and October CORSIKA samples, to the average of all five samples.	157
8.17	Bin-wise comparison of the neutrino event rates from the March and December CORSIKA samples, to the average of all five samples.	158
8.18	Bin-wise comparison of the neutrino event rates from January CORSIKA sample, to the average of all five samples.	159
9.1	Distributions of the dE/dX observable, for data and simulation.	161
9.2	Results of the atmospheric neutrino spectrum unfolding.	161

9.3	Forward folding fit.	162
9.4	Statistical uncertainties in the unfolded result.	163
9.5	Possible variability in the true flux allowed by DOM and ice property uncertainties.	164
9.6	Comparison of unfolded spectra for different zenith regions.	165
9.7	Unfolded result for various values of <i>kterm</i>	167
9.8	Introduction of errors through event weighting in simulation.	167
9.9	Uncertainties in the unfolded result.	168
9.10	Uncertainties in the unfolded result.	169
9.11	Comparison of Honda and Bartol models to unfolded result.	170
9.12	Comparison of the minimum and maximum of the Sarcevic prompt flux to unfolded result.	170
9.13	Comparison of various prompt flux models to unfolded result.	171
9.14	RA distribution for events used in the vector model analysis.	172
9.15	Energy reach of the neutrino sample in the vector model analysis.	173
9.16	Likelihood ratios for prompt flux nuisance parameters treated as physics parameters.	175
9.17	Upper limit on prompt flux normalization from likelihood analysis.	176
9.18	Likelihood ratios for data under the $n = 1$ VLI model.	178
9.19	Likelihood ratios for data under the $n = 1$ VLI model, minimum of prompt flux amplitude assumed to be 0.	178
9.20	Likelihood ratios for AMANDA-II data under the $n = 1$ VLI model.	179
9.21	Likelihood ratios for data under the $n = 2$ decoherence model.	180
9.22	Likelihood ratios for data under the $n = 2$ decoherence model, mini- mum of prompt flux amplitude assumed to be 0.	181

List of Abbreviations

ATWD	Analog Transient Waveform Digitizer
CC	Charged Current
CL	Confidence Level
COG	Center of Gravity (of PMT charge)
CP	Charge conjugation and Parity inversion symmetry
CPT	Charge conjugation, Parity inversion, and Time reversal symmetry
CPTV	CPT Violation
DCT	Discrete Cosine Transform
DFT	Discrete Fourier Transform
DIS	Deep Inelastic Scattering
DOM	Digital Optical Module
DST	Discrete Sine Transform
EM	Electromagnetic
EP	Equivalence Principle
fADC	fast Analog-to-Digital Converter
GR	General Relativity
LHC	Large Hadron Collider
LI	Lorentz Invariance
MAV	Maximum Attainable Velocity
MB	Main Board
MC	Monte Carlo
MPE	Multiple Photoelectrons
NC	Neutral Current
NPE	Number of Photoelectrons
PDF	Probability Distribution Function or Parton Distribution Function
PE	Photoelectron
PMT	Photomultiplier Tube
PnF	Processing and Filtering
QD	Quantum Decoherence
QFT	Quantum Field Theory
QG	Quantum Gravity
RA	Right Ascension
SM	Standard Model
SME	Standard Model Extension
SPADE	South Pole Archival and Data Exchange system
SPE	Single Photoelectron
V-A	Vector-Axial
VEP	Violation of Equivalence Principle
VLI	Violation of Lorentz Invariance

Chapter 1

Introduction

1.1 Neutrinos and Quantum Gravity Phenomenology

Neutrinos have been in the spot-light since they provided the first indication of physics beyond the Standard Model (SM) of particle physics when neutrino oscillations were confirmed. Neutrinos are now playing a key role in sorting out a variety of mysteries, including grand unification, extensions to the SM, CP (Charge-conjugation and Parity transformation), and CPT (Charge-conjugation, Parity transformation, and Time reversal) violating processes, supersymmetry, electroweak symmetry breaking, and searches for signatures of extra dimensions. Neutrinos may help explain the matter/antimatter asymmetry in the universe through “leptogenesis”, and may play a role in understanding dark energy.

Quantum Field Theory (QFT) and General Relativity (GR) are the theoretical and mathematical foundations of modern physics. Lorentz invariance (LI) and CPT symmetry are built into these theories. Also, the equivalence principle (EP) provides the foundational basis for GR. To date, no experimental evidence for a violation of any of these symmetries has been found. Despite the overwhelming theoretical and experimental support for these symmetries, it remains worthwhile to continue to test them in as many ways and in as many particle sectors as possible, at higher energy scales or with improved precision. Observation of a violation of one of these

symmetries would be an indication of new physics.

Lorentz invariance means that a property or process remains invariant under a Lorentz transformation. That is, it is independent of the coordinate system and independent of the location or motion of the observer, and the location or motion of the system. Lorentz invariant properties or processes are not changed by boosts, rotations, or translations. Characteristic signals of violation of Lorentz invariance (VLI) in the neutrino sector [1] include unconventional energy dependencies for oscillation lengths and mixing angles, $L-E$ conflicts manifesting as experiments probing the same L/E phase space having conflicting results, compass asymmetries or periodic variations due to rotation symmetry breaking, and $\nu \leftrightarrow \bar{\nu}$ mixing.

The EP is the idea that the effects of acceleration are indistinguishable from the effects of a uniform gravitational field. The EP requires that gravitational and inertial mass are equivalent, that a particle's coupling to a gravitational field is proportional to its inertial mass. In some neutrino oscillation models, violation of the equivalence principle (VEP) is phenomenologically equivalent to VLI.

The operation of charge conjugation, represented by C , is the swapping of a particle for its antiparticle in an interaction. Parity reversal, P , is the reversal of the coordinates used to describe a system, $x \rightarrow -x$, $y \rightarrow -y$, and $z \rightarrow -z$, equivalent to a mirror image, or changing the sign of the momentum for the particles involved in an interaction. Time reversal symmetry, T , is the invariance of a physical process when all motions are reversed, that is, incoming and outgoing states are swapped and the direction of motion is reversed. CP is the combined operation of charge conjugation and parity reversal. Most particle interactions are invariant to each of

these operations. However, there are a few isolated examples of particle interactions that violate C , P , CP , or T symmetries. No cases of CPT violation (CPTV) are known and CPT symmetry is currently held to be an exact symmetry of the universe. A violation of CPT in the neutrino sector would manifest itself as a flavor-changing process in which

$$P_{\nu_\alpha \rightarrow \nu_\beta} \neq P_{\bar{\nu}_\beta \rightarrow \bar{\nu}_\alpha}. \quad (1.1)$$

Physicists have so far been unable to reconcile the two paradigms of modern physics, QFT and GR, and produce a coherent theory of quantum gravity (QG). The theory must be able to predict the outcome of situations where both quantum effects and strong-field gravity are important. Such a theory is required in order to understand problems involving the combination of very high energy and very small dimensions of space, such as black hole singularities, the origin of the universe, or the unification of gravity with the other three fundamental forces. An understanding of quantum gravity may also be necessary to explain dark energy.

Much of the difficulty in meshing GR and QFT at all energy scales comes from the different assumptions that these theories make concerning how the universe works. QFT depends on particle fields embedded in the flat spacetime of special relativity. GR models gravity as a curvature within spacetime that changes as a gravitational mass moves. The most straight-forward ways of combining the two theories are non-renormalizable. This problem is related to the fact that all particles attract each other gravitationally, and energy as well as mass causes spacetime curvature. New, infinite terms in a calculation proliferate at each order in

perturbation theory. Attempts at a workable theory of quantum gravity include string theory [2, 3], loop quantum gravity [4], and noncommutative geometry [5].

Common to many philosophical or phenomenological approaches to QG is the possibility that LI and CPT symmetry may not hold at extremely small distance scales (high energy scales), due to a discrete structure of spacetime. Additionally, interactions with a spacetime foam or virtual black holes may induce quantum decoherence in which pure quantum states evolve into mixed states [6]. Lorentz invariance and/or unitarity may not hold in highly curved spacetimes with boundaries, such as in the vicinity of a microscopic black hole or the cosmological horizon of an inflationary universe [7, 8]. If different neutrino eigenstates interact differently with a spacetime foam or with a gravitational potential, the EP may be violated.

Moreover, there are various arguments that imply there may be detectable signatures below the Planck scale related to breaking of these symmetries. Arguments for seeing these effects at the TeV scale, which is the center-of-mass energies for the neutrinos in this analysis, are similar to arguments for seeing black hole production at the Large Hadron Collider (LHC). For example, warped extra dimensions can lead to gravity becoming important at the TeV scale [9]. Although QG provides the philosophical motivation for suspecting that LI and CPT symmetry may not hold in a final theory, the phenomenological models discussed here can be considered to be a generic search for VLI or CPTV, independent of the origin of the new physics. Neutrinos, lacking any gauge interactions other than weak and having extremely high Lorentz factors, are sensitive probes of these effects.

1.2 Neutrinos and the IceCube Neutrino Observatory

Neutrinos have played a fascinating role in the quest to understand matter and energy throughout the past century. By 1914, an inescapable paradox had arisen with regard to radioactive β decays. With only two particles in the final state, the resultant nucleus and the electron, conservation of energy and momentum demanded that the electron have a monochromatic energy spectrum. However, what was observed was that the electron had a continuous energy spectrum. It wasn't until 1930 that an idea was proposed to explain this without abandoning the principle of the conservation of energy. Wolfgang Pauli proposed a “desperate way out” by postulating a new particle. This hypothetical particle was initially called the neutron, but later renamed the neutrino. Neutrinos were first detected in 1958, in a reactor neutrino experiment performed by Fred Reines and Clyde Cowan [10].

Atmospheric neutrinos were first detected in the 1960's, in underground experiments that were only sensitive to horizontal muons [11, 12]. And in 1968, measurements of the solar ν_e flux found an anomalous deficit, sparking a debate over whether the problem was with neutrinos, the solar model, or with the experiment. This debate lasted for three decades. In the 1970's and 1980's, several detectors were built to search for proton decay to test grand unified theories that predicted finite lifetimes for protons. These detectors were either water Cherenkov detectors or iron calorimeters, and atmospheric neutrinos were a background for the experiments. Primarily, these detectors measured the ratio of ν_μ to ν_e in the flux of atmospheric neutrinos, since the prediction of this quantity was better constrained

than an absolute flux level. Some of the experiments found that the ratio was lower than expected. Whether this was due to a deficit of ν_μ , an excess of ν_e , or systematic errors in the detector(s), was far from clear.

Finally, in 1998, oscillations of atmospheric neutrinos were confirmed by Super-Kamiokande [13] (water Cherenkov) by observing an up-down asymmetry to the deficit, with strong support by results from Soudan2 [14] and MACRO [15] (both iron calorimeters). Oscillations were later confirmed by K2K and NuMI. In 2002, oscillations of solar neutrinos were confirmed by SNO and KamLAND.

Neutrinos are abundantly produced in stars as part of the fusion process that sustains them, as well as during supernova explosions. A handful of neutrinos from SN1987a, a supernova in the Large Magellanic Cloud, were detected by Kamiokande-II, IMB, and Baksan. Neutrinos were also produced as relics of the big bang. They are produced in nuclear reactors, particle accelerators, and in cosmic ray interactions in the Earth's atmosphere. Long baseline and reactor neutrino oscillation experiments, now underway or in development, such as NUMI/MINOS, K2K, NoVa, T2K, and Double Chooz, will play a key role in validating and clarifying neutrino physics with new and more precise measurements.

Atmospheric neutrinos are produced in the decay chains of particles created by the interaction of cosmic rays with the Earth's atmosphere [16, 17]. The most likely explanation to-date for the apparent disappearance of ν_μ in the flux of atmospheric neutrinos is that they are oscillating into ν_τ , as described in Chapter 2 and Eqn. 2.10. According to the prevailing model, the oscillations are due to coherent combinations of mass eigenstates that compose the flavor eigenstates. However, several other

mechanisms have been proposed that could lead to $\nu_\mu \rightarrow \nu_\tau$ flavor transitions. Such mechanisms include VLI [18, 19, 20] and/or violation of CPT symmetry [21, 22, 23], VEP [24, 25, 26, 27], and decoherence of neutrino flavor states [6]. Signals of Lorentz and CPT violating physics are expected to be suppressed by some power of the Planck mass, $M_P \sim 10^{19}$ GeV.

The IceCube neutrino telescope [28], currently under construction in the glacial ice at the South Pole, detects the Cherenkov radiation emitted by charged particles produced by neutrino interactions in the ice or rock. IceCube is capable of detecting neutrino interactions of all three flavors (electron, muon, and tau neutrinos) from atmospheric and astrophysical sources. Determining the origin and production mechanisms for cosmic rays is a primary goal of IceCube and led to the design and scale of the detector [29]. IceCube will open up an unexplored realm of neutrino astrophysics with unprecedented energies, from TeV to PeV scales [30]. IceCube can also be used for a wide range of particle physics analyses, such as indirect searches for dark matter, tests of TeV scale gravity and supersymmetry, and monopole searches.

Over its lifetime, IceCube will provide a significant increase in the energy coverage and event statistics for atmospheric neutrinos. Gonzalez-Garcia, et al., [31], estimate that IceCube will be able to accumulate more than 700 thousand atmospheric neutrino events with energies above 100 GeV over its ten-year lifetime. With this large data set, it may be possible to detect deviations from the assumption that the mass-induced oscillations model fully explains flavor transitions [31]. Additionally, the energy spectrum, zenith angle dependence, and flavor distribution of atmospheric neutrinos have been extensively studied, and will help calibrate Ice-

Cube in the energy range 100 GeV to several hundred TeV, and can be used to study systematic uncertainties in IceCube.

The deep glacial ice at the South Pole is optically transparent, making it an ideal medium for a large volume Cherenkov detector. Also, deep in the ice, particles such as cosmic ray muons that are an undesirable background for most analyses planned for IceCube are attenuated. Upward moving particles will have had to result from particles that penetrated the Earth and can readily be identified as due to neutrino interactions. Even with a cubic-kilometer detector, and with the exception of atmospheric neutrinos, event rates on the order of a few to a few hundred per year are all that is expected by the most optimistic predictions for many of the astrophysical phenomena for which IceCube is being built. For the more speculative physics issues, such as dark matter, quantum gravity, and topological defects, IceCube is expected to significantly improve constraints on various models even if it does not make a discovery.

IceCube has already collected a large sample of atmospheric muon neutrinos while operating in a partially completed 40-string configuration from 17 April, 2008, to 20 May, 2009. This data was used to unfold the spectrum of atmospheric neutrinos at their point of origin in the atmosphere, over the neutrino energy range 100 GeV to 400 TeV. Boosted decision trees were used to obtain an event sample of up-going atmospheric muon neutrinos with negligible background contamination from mis-reconstructed atmospheric muons. Seasonal variations in the atmospheric neutrino flux were also studied.

The Standard Model Extension (SME) provides a phenomenological frame-

work for studying possible low energy signatures of Lorentz and CPT violation [32]. Using a discrete Fourier transform method, constraints were placed on certain coefficients contained within the SME, in the context of a neutrino oscillation model that violates rotational invariance. The limits from other experiments were improved by more than three orders of magnitude. A likelihood analysis method was developed, with events binned in energy and direction, to analyze a variety of VLI, CPTV, and decoherence models. The impact of systematic uncertainties in theoretical predictions for the neutrino flux, as well as in the detector response, simulation, and reconstruction, on the two-dimensional likelihood analysis were studied. Areas in which the systematic uncertainties need to be reduced were identified.

Chapter 2

Neutrino Particle Physics and Astrophysics

2.1 Neutrinos In and Beyond the Standard Model

The SM is based on the strong and electroweak gauge groups

$$G_{SM} = SU(3)_C \times SU(2)_L \times U(1)_Y. \quad (2.1)$$

The symmetry properties of the three gauge groups on the right hand side explain the behavior of the strong, weak, and electromagnetic forces, and the interactions of particles subject to these forces. The three neutrino flavor states, ν_e , ν_μ , and ν_τ , are paired with their charged lepton counterparts, e , μ , and τ . The lepton doublets in the SM are

$$\begin{pmatrix} e^- \\ \nu_e \end{pmatrix}, \begin{pmatrix} \mu^- \\ \nu_\mu \end{pmatrix}, \text{ and } \begin{pmatrix} \tau^- \\ \nu_\tau \end{pmatrix}.$$

The gauge structure of the SM, and the representations of the physical states observed in nature, leads to lepton flavor symmetries. The number of each of the three flavors of leptons are individually conserved in any SM interaction. Anti-neutrinos have opposite signed lepton numbers. Neutrino mixing and CP violation in the lepton sector are not accounted for in the SM.

Neutrinos undergo only weak and gravitational interactions. In charged current (CC) weak interactions, they exchange a W^\pm boson with a nucleon and transform into a charged lepton. The charged lepton is the same lepton flavor as the

original neutrino, i.e. an electron, a muon, or a tau. In neutral current (NC) weak interactions, they exchange a Z^0 boson with a nucleon and remain a neutrino. According to the SM and vector-axial (V-A) theory, only left-handed neutrinos and right-handed anti-neutrinos are active, and both are massless. The SM contains a Higgs boson doublet. The vacuum expectation value (vev) of the Higgs is responsible for breaking the gauge symmetry, giving us the three massive vector bosons which are responsible for the short range of the weak force.

Fermion masses are generated by terms that include Yukawa couplings, a right-handed fermion, its left-handed doublet, and the Higgs boson. Since the SM does not include right-handed neutrinos (left-handed antineutrinos), neutrinos can not acquire mass in this same way. Nor can they acquire mass through loop corrections in the SM without violating the conservation of lepton number inherent in the model. Although experimental and astrophysical constraints indicate that neutrino masses are very small, their masses have not yet been directly measured. The discovery of neutrino oscillations, however, implies that neutrinos do have mass [33, 34, 35]. As a result, the helicity of a neutrino is not Lorentz invariant.

2.1.1 Neutrino Oscillations

The theory of mass-induced oscillations requires that neutrino flavor states exist as linear combinations (coherent sums) of three mass eigenstates

$$|\nu_\alpha\rangle = \sum_{i=1}^n U_{\alpha i}^* |\nu_i\rangle, \quad (2.2)$$

where the ν_α are the flavor eigenstates, ν_i are the mass eigenstates, and $U_{\alpha i}^*$ are the elements of an $n \times n$ mixing matrix. n is the number of active neutrino species (i.e. light enough to play a role in the oscillations and sharing a common eigenstate basis). For the general 3×3 case, the mixing matrix can be parametrized by three mixing angles, θ_{12} , θ_{23} , and θ_{13} , as well as a CP violating phase δ . A convenient factorization is

$$U = \begin{pmatrix} 1 & 0 & 0 \\ 0 & c_{23} & s_{23} \\ 0 & -s_{23} & c_{23} \end{pmatrix} \begin{pmatrix} c_{13} & 0 & s_{13}e^{-i\delta} \\ 0 & 1 & 0 \\ -s_{13}e^{+i\delta} & 0 & c_{13} \end{pmatrix} \begin{pmatrix} c_{12} & s_{12} & 0 \\ -s_{12} & c_{12} & 0 \\ 0 & 0 & 1 \end{pmatrix}, \quad (2.3)$$

where $c_{jk} = \cos(\theta_{jk})$ and $s_{jk} = \sin(\theta_{jk})$. In this factorization, the first matrix on the right-hand side leads to atmospheric and accelerator neutrino oscillation experiments, the second describes reactor experiments and the CP violating phase, and the third describes solar neutrino oscillations.

Fig. 2.1, from [36], shows the two pictures of neutrino interactions and propagation, based on the flavor and mass eigenstates. The time evolution of a neutrino flavor eigenstate as a neutrino propagates is given by

$$|\nu_\alpha(t)\rangle = \sum_{i=1}^n U_{\alpha i}^* |\nu_i(t)\rangle. \quad (2.4)$$

When detected in a CC interaction, the probability that a neutrino produced in flavor state α will be detected in flavor state β is given by

$$P_{\alpha\beta} = |\langle \nu_\beta | \nu_\alpha(t) \rangle|^2 = \left| \sum_{i=1}^n \sum_{j=1}^n U_{\alpha i}^* U_{\beta j} \langle \nu_j | \nu_i(t) \rangle \right|^2. \quad (2.5)$$

Technically, to calculate the effects of neutrino mixing requires quantum field theory and an accounting of individual, overlapping wave packets for each mass eigenstate

[37]. However, the standard method is to treat the mass eigenstates as plane waves

$$|\nu_i(t)\rangle = e^{-iE_i t} |\nu_i(0)\rangle, \quad (2.6)$$

and use an approximation for the dispersion equation

$$E_i = \sqrt{p_i^2 + m_i^2} \simeq p + \frac{m_i^2}{E}. \quad (2.7)$$

These approximations greatly simplify the calculations and, after accounting for smearing of the energy and detection time (or location), and the energy and momentum uncertainty, the more rigorous methods give the same results. Furthermore, neutrino production and detection via CC interactions depends on flavor state; experiments are not sensitive to the different contributions of different mass eigenstates. Energy and momentum uncertainty in the detection processes are large enough to make a determination of the mass of the incident neutrino impossible.

From the above equations, the oscillation probability is a function of neutrino energy and propagation distance, mass-squared differences of the mass eigenstates, and the elements of the neutrino mixing matrix [38]:

$$P_{\alpha\beta} = \delta_{\alpha\beta} - 4 \sum_{i<j}^n \text{Re} [U_{\alpha i} U_{\beta i}^* U_{\alpha j}^* U_{\beta j}] \sin^2 X_{ij} + 2 \sum_{i<j}^n \text{Im} [U_{\alpha i} U_{\beta i}^* U_{\alpha j}^* U_{\beta j}] \sin 2X_{ij}, \quad (2.8)$$

where

$$X_{ij} = \frac{(m_i^2 - m_j^2) L}{4E} = 1.27 \frac{\Delta m_{ij}^2}{\text{eV}^2} \frac{L/E}{\text{km/GeV}}. \quad (2.9)$$

L is the propagation distance, from production to detection. For relativistic neutrinos, L ($\approx t$), and E have the same behavior under Lorentz transformations and

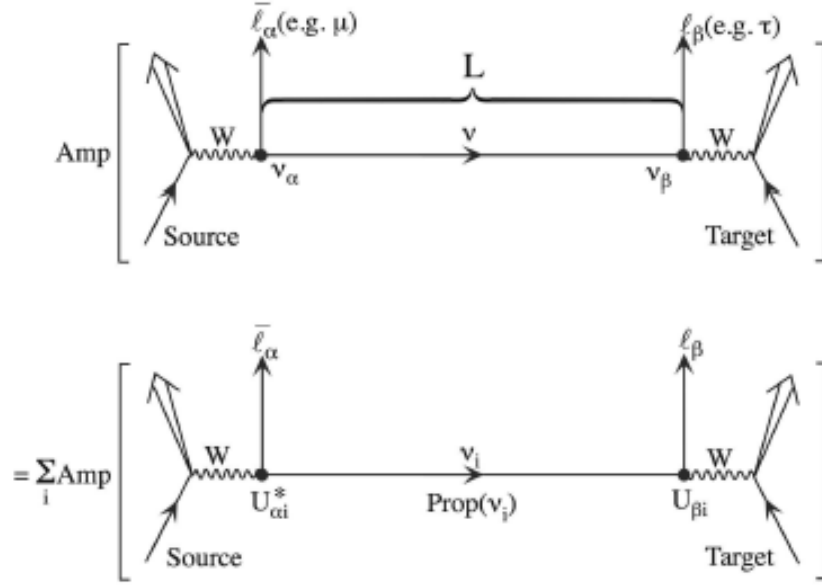


Figure 2.1: Schematic of neutrino production, propagation, and detection. Two pictures, based on flavor eigenstates (top) and on mass eigenstates (bottom). From [36].

the ratio L/E remains Lorentz invariant. Since there are three neutrino mass eigenstates, we can define two independent mass-squared differences, Δm_{12}^2 and Δm_{23}^2 . Current experimental results indicate that $\Delta m_{12}^2 \approx 10^{-4} \text{eV}^2$ and $\Delta m_{23}^2 \approx 10^{-3} \text{eV}^2$.

Oscillation experiments are sensitive to the difference of the squares of the masses for the different mass eigenstates, but they do not offer a determination of the absolute mass scale and hierarchy. The mass hierarchy refers to the ordering of the masses; normal ordering assumes they follow the ordering of masses in the quark families, as opposed to an inverted hierarchy (see Fig. 2.2). Ongoing attempts to directly measure the absolute mass scale include high-resolution analysis of the tail end of the electron energy spectrum in beta decay and searches for neutrino-less double beta decay. Neutrino-less double beta decay would also be direct evidence

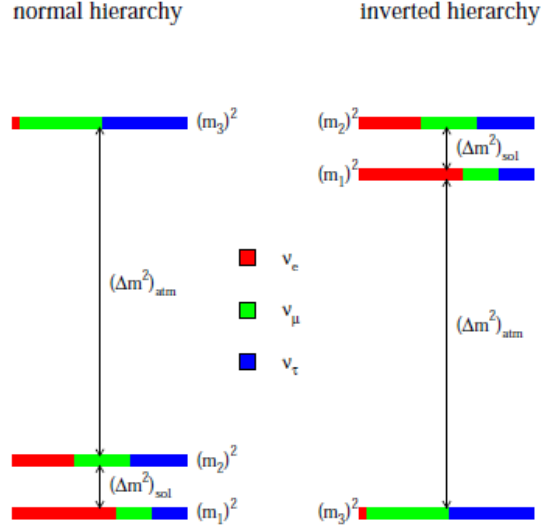


Figure 2.2: Possible mass spectra for neutrino mass and flavor eigenstates. Normal (assumed to be analogous to quark mass ordering) and inverted. From [39].

for whether B-L (baryon number – lepton number) is a fundamental symmetry of nature and whether neutrinos are Majorana or Dirac particles, i.e., whether they are their own antiparticles or they have distinct antiparticles [40, 41].

Atmospheric neutrino oscillations are dominated by transitions between just two neutrino flavors, ν_μ and ν_τ . The data from various experiments are not consistent with appearance of ν_e . Additionally, the appearance of ν_τ is supported by Super-K data [42]. An excellent approximation for atmospheric neutrino oscillations is a 2×2 mixing matrix that depends on just one mixing angle, θ_{23} , (θ below), and just one mass-squared difference, Δm_{23}^2 , (Δm^2 below). The oscillation probability is then

$$P_{\nu_\mu \rightarrow \nu_\tau} = \sin^2 2\theta \sin^2 \left(1.27 \frac{\Delta m^2 L}{E} \right). \quad (2.10)$$

The ν_μ survival probability is

$$P_{\nu_\mu \rightarrow \nu_\mu} = 1 - \sin^2 2\theta \sin^2 \left(1.27 \frac{\Delta m^2 L}{E} \right). \quad (2.11)$$

The following values are used for the parameters for mass-induced oscillation of atmospheric muon neutrinos [43]:

$$\begin{aligned} \Delta m^2 &= 2.39 \times 10^{-3} \text{ eV}^2, \\ \sin^2 2\theta &= 0.9954. \end{aligned} \quad (2.12)$$

Fig. 2.3 shows the ν_μ survival probability as a function of neutrino energy and zenith angle for these mass-induced oscillations. Mass-induced oscillations of atmospheric neutrinos, with a wavelength proportional to energy, are negligible above 100 GeV. The phenomenological models discussed in Chapter 3 will include oscillations that become important at higher energies.

Neutrino propagation length, L , is calculated using the equation [44]:

$$L = \sqrt{(R_\oplus + h)^2 - (R_\oplus - d)^2 \sin^2(\theta_Z)} - (R_\oplus - d) \cos(\theta_Z). \quad (2.13)$$

R_\oplus is the radius of the Earth, h is the height in the atmosphere that the neutrino was produced, d is the depth at which the neutrino interacted in the detector, and θ_Z is the zenith angle of the neutrino. We assume the Earth is spherical and also neglect the direction and energy dependence of mean production height. Average values of $R_\oplus = 6371$ km and $h = 20$ km are assumed [45, 46]. The depth of the center of the detector (2 km) is used for d . These approximations are only used for calculating the neutrino propagation length when estimating muon neutrino survival probability under various phenomenological models for oscillation or decoherence.

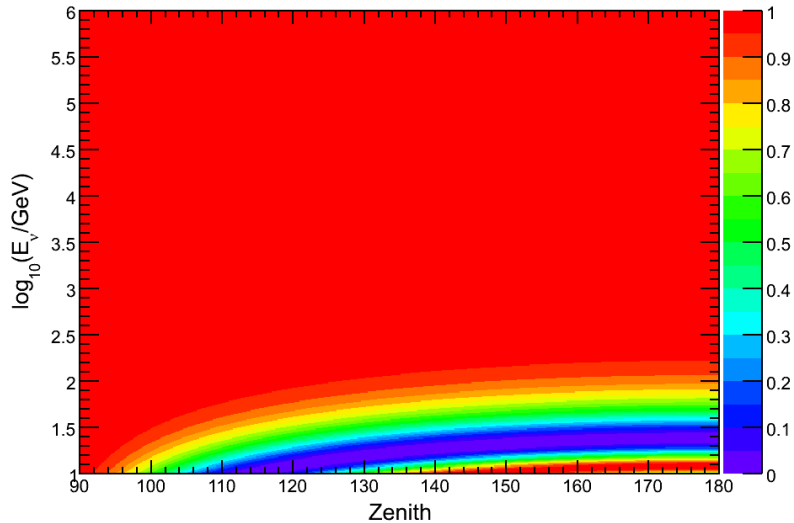


Figure 2.3: Atmospheric muon neutrino survival probability for mass-induced oscillations (Eqn. 2.11). The color scale represents the oscillation survival probability.

They are not used in the detailed numerical simulation of neutrino production in the atmosphere, propagation and interaction through the Earth, and interaction in or near the detector, as discussed in Chapter 6.

Attempts have been made to explain neutrino flavor appearance and disappearance data with non-standard interactions or new oscillation mechanisms, CPT violating processes or quantum gravity-induced decoherence, neutrino decay, mixing with sterile neutrinos that have no gauge interactions, or ultra-heavy right-handed neutrinos [40, 47, 48], or some combination of the above. Some of these scenarios have been excluded, others still remain plausible.

2.1.2 Standard Model Extension

To date, no evidence for VLI or CPTV has been seen and the symmetries of GR and the SM are holding firm against a wide variety of experimental investigations. However, as previously mentioned, there is some motivation to expect that these symmetries may not hold at all scales, and to look for signs of departure from them. The SM is believed to be the low-energy limit of a more fundamental theory. This more fundamental theory is typically assumed to unite quantum field theory and general relativity at the Planck scale. To look for signatures of quantum gravity at energies reachable in current experiments without a formal theory, a phenomenological description of low-energy effects is necessary. The Standard Model Extension (SME) is an effective-field-theory framework that fills this gap [49, 50].

The SME contains the SM and GR as limiting cases. It adds to the SM Lagrangian terms that can be constructed with SM and gravitational fields, but that may also violate Lorentz symmetry. The coefficients for these interactions have Lorentz indices and represent background tensor fields. Physically observable phenomena depend on contractions between these tensorial coefficients and the particle momentum. A subset of the SME, known as the “minimal” SME [51], includes all observer-independent, renormalizable (i.e. operators with mass dimension 4), Lorentz and CPT violating interactions. Energy and momentum are still conserved, spin-statistics and gauge invariance are maintained. Right-handed neutrinos are still assumed to decouple and remain undetectable. Neutrino masses are handled the same way as in the SM.

The SME has served as the phenomenological guide for numerous experimental searches for signatures of Lorentz and CPT violation [52], including protons, neutrons, electrons, photons, mesons, and gravity. The SME also provides the basis for searching for a variety of Lorentz and CPT violating signals in the neutrino sector, signals that include oscillations with unique energy dependencies and direction-dependent oscillations [1]. The effective Hamiltonian for the propagation of free neutrinos, with Lorentz-violating terms, is [51]

$$(h_{eff})_{ab} = E\delta_{ab} + \frac{(m^2)_{ab}}{2E} + \frac{1}{E} [(a_L)^\mu p_\mu - (c_L)^{\mu\nu} p_\mu p_\nu]_{ab}, \quad (2.14)$$

where E is the neutrino energy and p_μ is the neutrino four-momentum. The indices a and b range over the three generations of leptons, $e, \mu,$ and τ . The second term on the right leads to mass-induced oscillations, the third term leads to Lorentz and CPT violating oscillations. Coefficients $(a_L)_{ab}^\mu$ have mass dimension one and lead to LI and CPT violating interactions. For antineutrinos, the sign of a_L is reversed. Coefficients $(c_L)_{ab}^{\mu\nu}$ are dimensionless and lead to interactions that violate LI, but not CPT symmetry. The SME includes mixing between neutrinos and antineutrinos, $\nu \leftrightarrow \bar{\nu}$, but that will not be considered here because IceCube can not distinguish between neutrinos and antineutrinos.

2.2 Cosmic Rays

Cosmic rays are high energy particles, mostly protons and helium nuclei, but also heavier ionized nuclei, that are accelerated in various astrophysical phenomena. The origin of cosmic rays is still an area of very active research. Included in the

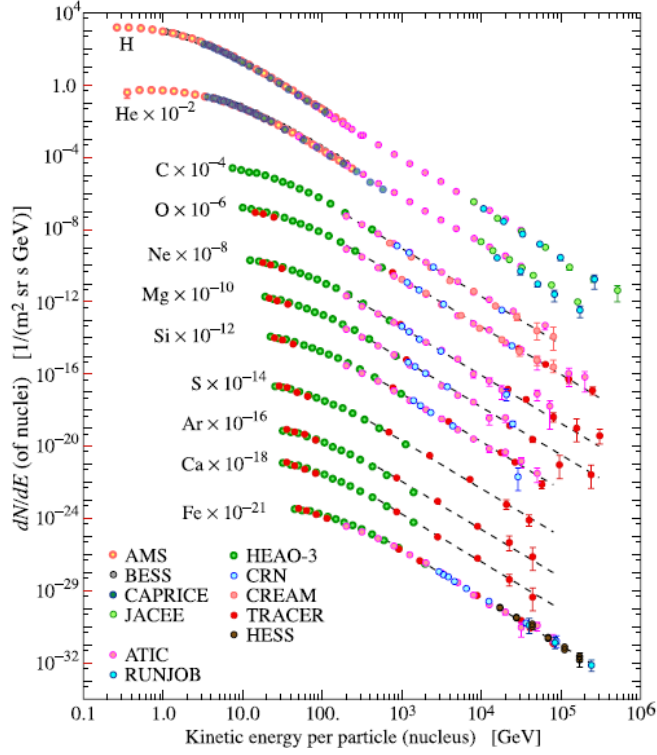


Figure 2.4: Energy dependence and composition of flux of cosmic ray primaries. From [53].

primary cosmic rays are electrons, protons, helium, carbon, oxygen, iron, and other nuclei synthesized in stars [53]. Fig. 2.4 shows the composition of the cosmic ray flux. Particles produced in the interactions of cosmic ray primaries with the interstellar medium are known as secondaries. Lithium, beryllium and boron, as well as positrons and antiprotons, are mostly secondaries [53]. Low energy cosmic rays are modulated by the solar wind and deflected by the Earth's geomagnetic field. However, these effects are negligible for the energy range of this analysis. Higher energy cosmic rays arrive isotropically, with deviations on the order of a very small fraction of a percent [54].

There are only a few known production sites for cosmic rays. Possible origins (depending on energy scale and flux level) include AGN, GRB, supernova explosions, evaporating black holes, topological defects, and decay products of exotic particles. Most cosmic rays originate from within the galaxy, likely from supernova shock acceleration. Charged particles can diffuse across the plasma shock boundary many times, gaining energy each time in a process known as Fermi acceleration. The highest energy cosmic rays would not be confined by the galactic magnetic field, however, and are believed to be from extragalactic sources [55].

If cosmic rays are produced in hadronic interactions, neutrinos should be produced in conjunction with them. Hadrons accelerated at these sources should interact with matter and/or radiation fields, producing charged pions and kaons. These mesons will then decay, producing neutrinos as part of their decay products, analogous to the production of atmospheric neutrinos by cosmic rays. IceCube will be able to detect these neutrinos, and after several years of data collection, it should be possible to correlate neutrino point sources with the sources of high energy gamma rays [56]. Detecting neutrinos from objects that are believed to be the source of at least some of the cosmic rays would narrow down the production and acceleration mechanism, by verifying associated production of neutrinos in hadronic processes.

The energy spectrum of cosmic rays is rather steep, $dN/dE \propto E^{-2.7}$, and steepens to $dN/dE \propto E^{-3}$ above the “knee”, or about 10^6 GeV [57]. This steepening could be related to a turnover between galactic origins (below the knee) to extragalactic origins above a second knee. This second knee is a steepening to about $E^{-3.2}$ above about 5×10^8 GeV, which could be associated with a rigidity-dependent cutoff.

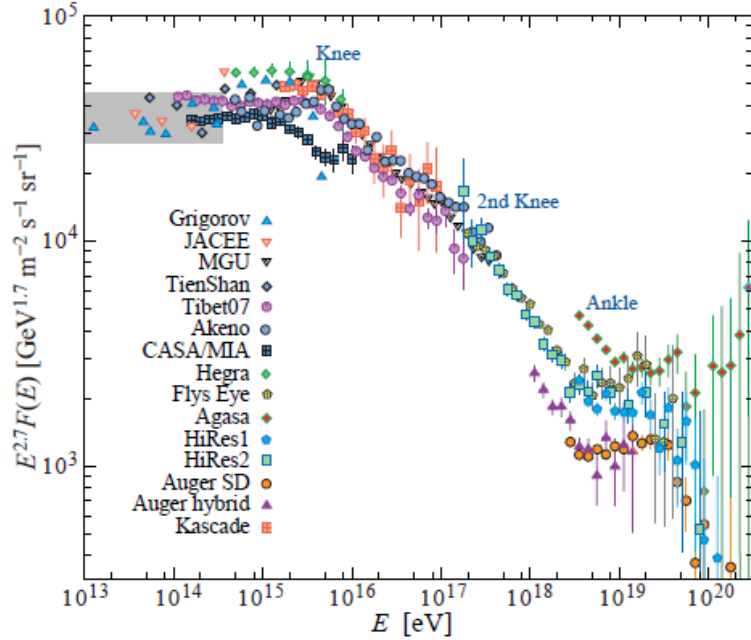


Figure 2.5: All-particle spectrum from air shower measurements. From [53].

Higher energy cosmic rays diffuse out of the galaxy [58]. Fig. 2.5 shows the cosmic ray spectrum. Both knees and the ankle are identified in the figure.

Hadronic interactions between cosmic rays and particles in the atmosphere produce large numbers of mesons, primarily pions and kaons. In fact, hundreds or even thousands of these mesons can be produced in the shower that ensues the interaction of a single high energy cosmic ray. Neutrinos are produced in the leptonic or semi-leptonic decays of charged pions or kaons, as well as in the subsequent decays

of the muons:

$$\begin{aligned}
\pi^+(K^+) &\rightarrow \mu^+ + \nu_\mu, \\
\pi^-(K^-) &\rightarrow \mu^- + \bar{\nu}_\mu, \\
\mu^+ &\rightarrow \bar{\nu}_\mu + e^+ + \nu_e, \\
\mu^- &\rightarrow \nu_\mu + e^- + \bar{\nu}_e.
\end{aligned}
\tag{2.15}$$

Fig. 2.6, from [59], shows the particle production from a cosmic ray air shower.

ν_e are produced in the muon decays, but ν_μ are created in the meson decays as well as the muon decays. Additionally, many muons range out before they have a chance to decay. Hence, the ratio of ν_μ to ν_e is a function of direction and energy [60]. For this analysis, ν_e events are not included in the final event sample. Event selection cuts used to isolate track-like events (from the muons resulting from ν_μ CC interactions) eliminate localized events from the electromagnetic showers induced by ν_e CC interactions. Production of ν_τ by cosmic ray interactions is negligible.

Fig. 2.7 shows the seasonal variation of the down-going flux of atmospheric muons in IceCube [61]. T_{eff} is a weighted average of the temperature of the South Pole atmosphere, from the surface to the top of the atmosphere. The yearly seasonal temperature variation in the upper atmosphere is highly correlated with the high energy muon rate observed deep in the ice, leading to a 10% seasonal variation in the muon event rate. This is due to the kinematics of meson propagation in a less dense, or more dense, atmosphere and the likelihood of producing a muon through decay before collision. The seasonal variation of the rate of up-going atmospheric neutrinos in IceCube is a function of the latitude of their origin, and is expected to be about 3.5% for neutrinos originating from high latitudes, and less than 0.5% for

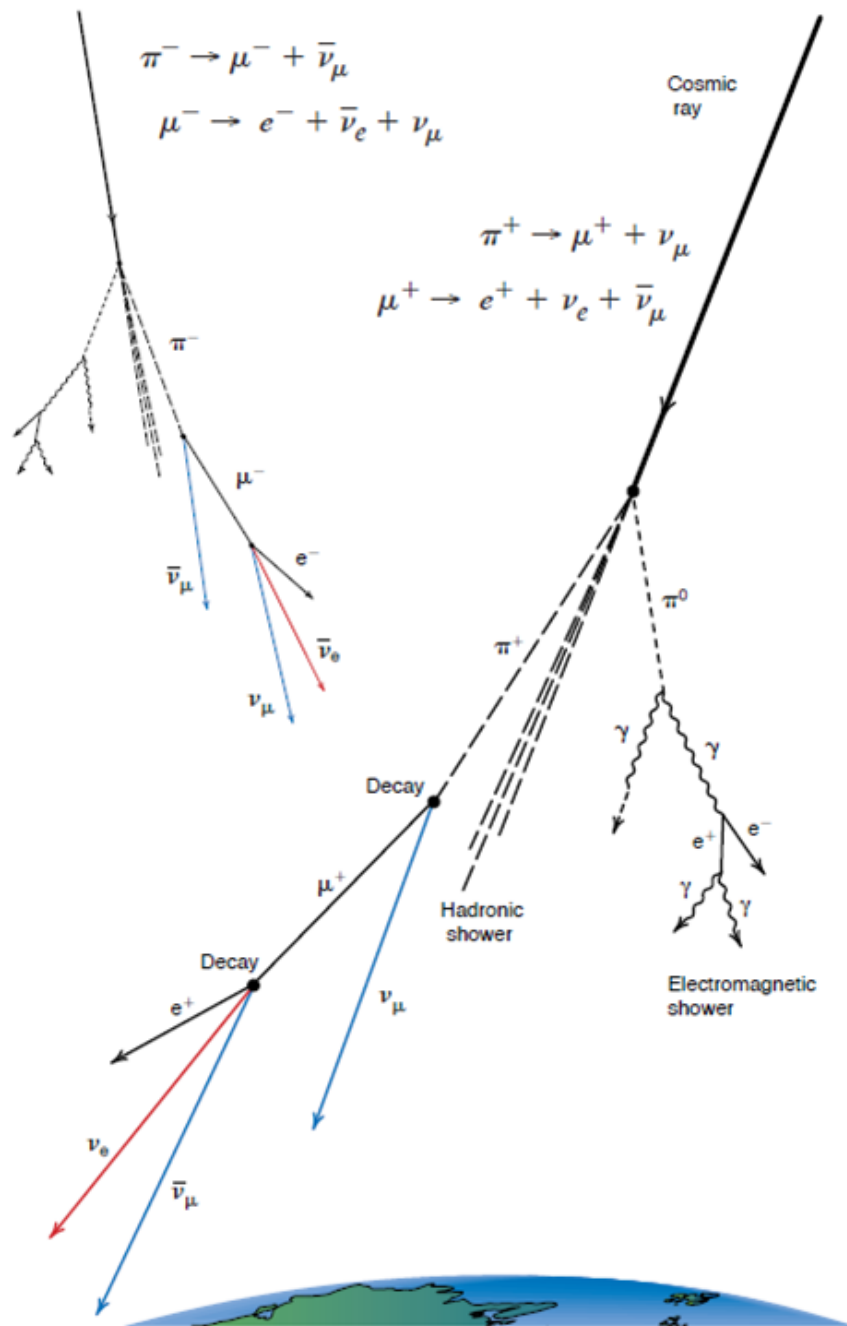


Figure 2.6: Particle production in cosmic ray air shower. From [59].

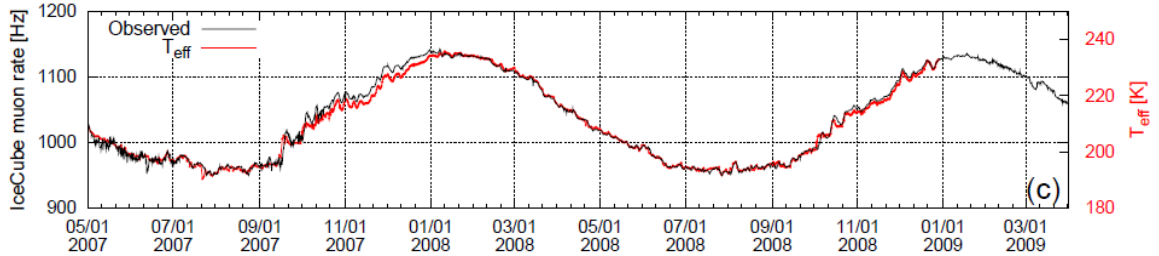


Figure 2.7: Seasonal variation in atmospheric muon flux for IceCube 22-string configuration [61].

neutrinos originating from low latitudes [62].

The dominant parent particles for atmospheric neutrinos depends on the energy and is related to the critical energy, E_{crit} , of the parent particle. E_{crit} is the energy of the parent particle for which decay and interaction lengths are equal. Above E_{crit} , energy loss through collisions is likely prior to decay. Below E_{crit} , the particle is more likely to decay before interacting. E_{crit} is a function of the lifetime of the parent particle as well as the density profile of the atmosphere. The critical energies for various parent particles are listed in Table 2.1.

The zenith angle dependence of atmospheric neutrinos is more complicated than cosmic rays. Mesons in inclined showers spend more time in the tenuous atmosphere where they are more likely to decay rather than interact. For this reason the spectra of highly inclined neutrinos are flatter than those of almost vertical neutrinos. Additionally, neutrino absorption in the Earth is a function of energy and zenith angle. Fig. 2.8 shows the attenuation of the atmospheric neutrino flux in the Earth. Above about 100 TeV, neutrinos have a high probability of interacting as they transit the diameter of the Earth.

Table 2.1: Critical energies for various parent particles that contribute to the atmospheric neutrino flux. From [63] and based on an isothermal atmosphere with a scale height of 6.4 km.

Particle	Elementary Contents	mc^2 (MeV)	$c\tau$	E_{crit} (GeV)
D^+, D^-	$c\bar{d}, \bar{c}d$	1870	317 μm	3.8×10^7
D^0, \bar{D}^0	$c\bar{u}, \bar{c}u$	1865	124 μm	9.6×10^7
D_s^+, D_s^-	$c\bar{s}, \bar{c}s$	1969	149 μm	8.5×10^7
Λ_c^+	udc	2285	62 μm	2.4×10^8
μ^+, μ^-	lepton	106	659 m	1.0
π^+, π^-	$u\bar{d}, \bar{u}d$	140	7.8 m	115
K^+, K^-	$u\bar{s}, \bar{u}s$	494	3.7 m	855
Λ^0	uds	1116	7.9 cm	9.0×10^4

2.2.1 Conventional Atmospheric Neutrino Flux

The conventional atmospheric neutrino flux [16, 17] consists of ν_μ and ν_e produced in the decays of pions and kaons. Pions and kaons that decay in-flight, often after losing some of their energy in collisions, are the dominant source of atmospheric neutrinos up to about 10 TeV. The loss of energy in the collisions of the parent particle leads to lower energy neutrinos among the daughter products, and the spectral slope of conventional atmospheric neutrinos is about -3.7 , as compared to -2.7 for cosmic rays. Some of the muons produced in the decay of these mesons also decay in-flight in the atmosphere, producing additional neutrinos, while others reach the ground and range out before decaying. Charged pions decay mostly into muons, so the flux of ν_μ from these air showers is much larger than the flux of ν_e .

The ratio π/K (ratio of pion production to kaon production) can have an affect on the zenith angle distribution of conventional atmospheric neutrinos. The impact that this ratio has depends on propagation lengths in the atmosphere, pion

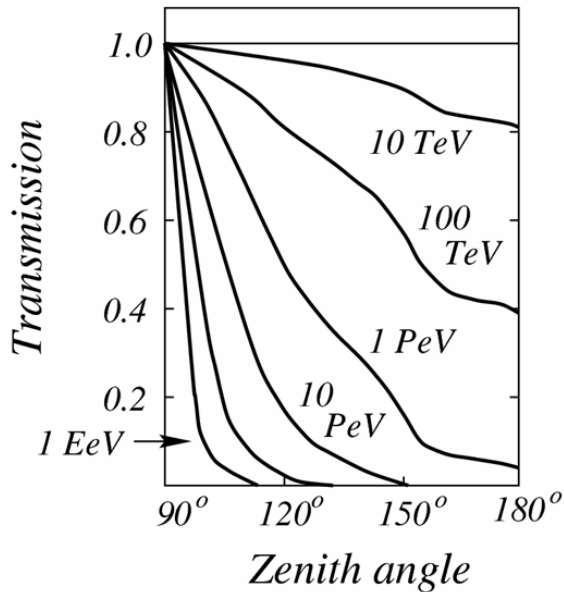


Figure 2.8: Zenith angle and energy dependence of survival probability as neutrinos propagate through the Earth. From [64].

and kaon lifetimes, kinematics of decay, and energy loss due to scatterings before decay [65]. Uncertainty in kaon production dominates the uncertainty in this ratio. Fig. 2.9 shows the conventional atmospheric muon neutrino flux, including the sum of ν_μ and $\bar{\nu}_\mu$.

2.2.2 Prompt Atmospheric Neutrino Flux

Charmed mesons and baryons can play an important role when sufficient energy is available. The prompt atmospheric neutrino flux [66, 67, 68] is made up of neutrinos produced in the decays of charmed D mesons and Λ_c hyperons [63] produced in the atmosphere:

$$D \rightarrow K + \mu + \nu \quad \text{and} \quad \Lambda_c \rightarrow \Lambda_0 + \mu + \nu, \quad (2.16)$$

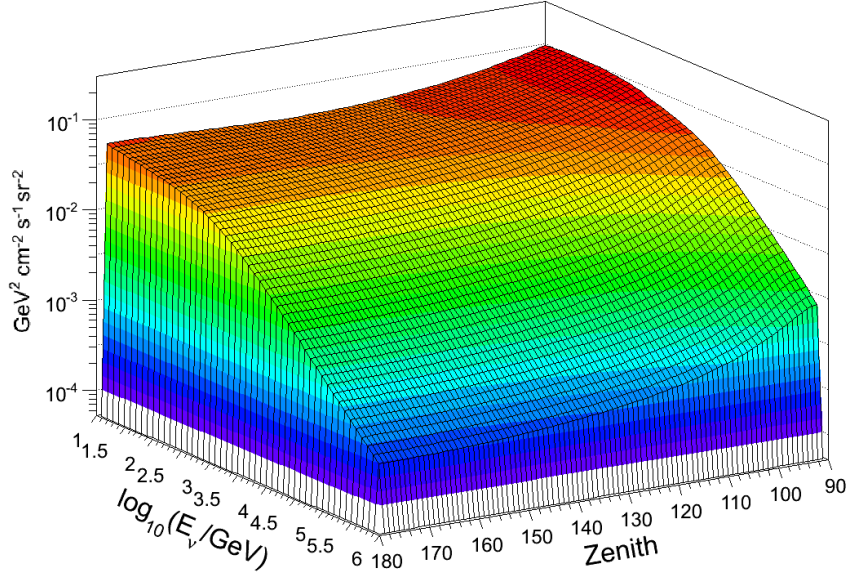


Figure 2.9: Energy and zenith dependence of conventional atmospheric muon neutrino flux. Based on the model of [17].

but is not expected to become important until above a few tens of TeV. Charmed mesons and baryons decay almost immediately, before losing energy in collisions. Hence, the spectrum for the prompt flux is about one power harder than the conventional flux and, with a spectral index of about -2.7 , more closely follows the cosmic ray spectrum. Since charmed mesons are equally likely to decay into electrons or muons, the prompt neutrino flux for muon neutrinos and anti-neutrinos is the same as that for electron neutrinos and anti-neutrinos. The prompt flux is also independent of zenith angle.

The production of charmed mesons at cosmic ray energies is not well-measured by accelerators. Uncertainties associated with the prompt flux, due to charm production cross sections and fragmentation functions, etc., are much larger than for the

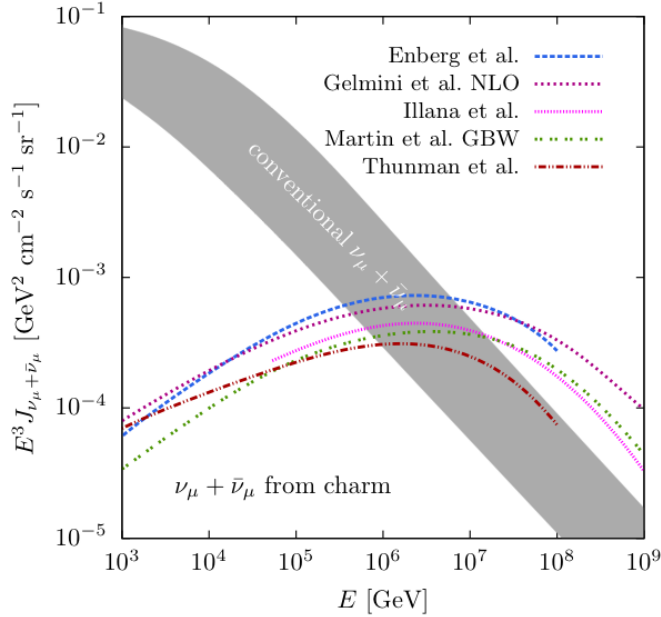


Figure 2.10: Theoretical predictions for the prompt atmospheric muon neutrino flux. From IceCube Yellow Book.

conventional component. There is a significant amount of uncertainty concerning the exact turnover energy between conventional and prompt sources of atmospheric neutrinos, estimates vary from about 10 TeV to 1 PeV. Enberg *et al.* [66] find that, for the vertical flux of atmospheric muon neutrinos, the prompt component begins to dominate over the conventional component between about 10^5 GeV and $10^{5.5}$ GeV, just above the energy reach of this analysis.

Fig. 2.10 shows theoretical predictions for the prompt flux in relation to predictions for the conventional flux. The predictions for the prompt flux can be seen in Fig. 2.11, as well as the estimated overlap between the atmospheric neutrino flux and an anticipated diffuse flux of astrophysical neutrinos. A diffuse flux of astrophysical neutrinos is ignored in this analysis.

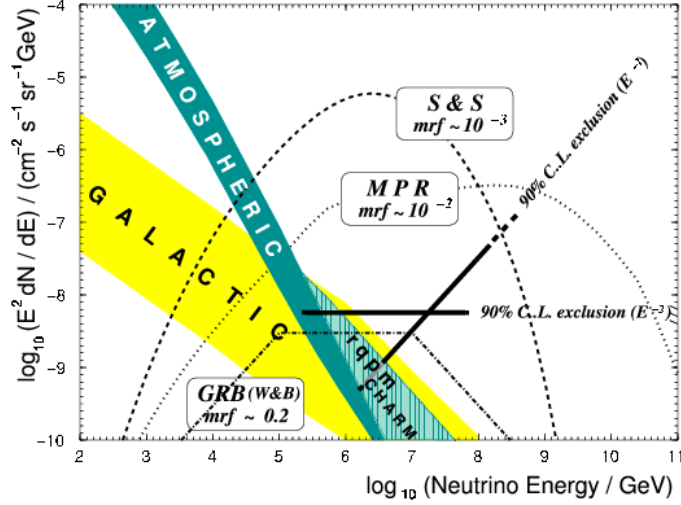


Figure 2.11: Components of the muon neutrino flux in IceCube. The uncertainty in charm production models, (light green) as well as the diffuse background (yellow). From [69].

Fig. 2.12 shows the combined atmospheric neutrino flux, including conventional and prompt components. The prompt component is only visible at the highest energies in Fig. 2.12 (compare to Fig. 2.9).

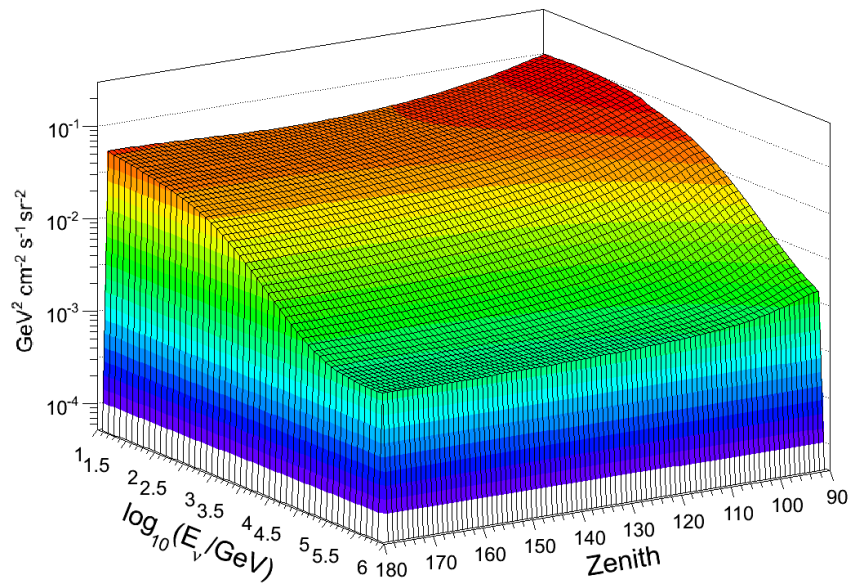


Figure 2.12: Energy and zenith dependence of atmospheric muon neutrino flux, including prompt and conventional components. Based on the models of [17] and [66].

Chapter 3

Phenomenology

Mass-induced oscillations are suppressed at the energy scale of this analysis, which is about 100 GeV to several tens of TeV, since the oscillation wavelength is proportional to energy. On the contrary, certain VLI and decoherence models contain neutrino flavor oscillations with wavelengths that are inversely proportional to energy, or some power thereof. Additionally, some models contain oscillations that depend on the direction of the neutrino momentum. The high energy and high statistics reach of IceCube, for atmospheric neutrinos, provides unique sensitivity to these unconventional models.

3.1 Violation of Lorentz Invariance

We can arrive at an equation for Lorentz-violating oscillations of atmospheric neutrinos a variety of different ways. Instead of the usual dispersion relationship that leads to the derivation of the mass-induced neutrino oscillation equation, we can start with a modified dispersion equation:

$$E^2 = m^2 + p^2 + f(p^2, E, m). \quad (3.1)$$

f is some function, suppressed by the Planck mass, M_P , that may be flavor-dependent. Depending on the nature of f and the physics behind it, this may lead to a deformed Lorentz symmetry. The Lorentz transformation may be changed

but Lorentz invariance and observer-independence could still hold. If Eqn. 3.1 takes a form such as [70]

$$E^2 \approx m^2 + p^2 - \eta \left(\frac{E}{M_P} \right)^n p, \quad (3.2)$$

where η is assumed to be order one, then Lorentz symmetry is broken. The neutrino oscillation equation derived using Eqn. 3.2, instead of the usual dispersion relation (Eqn. 2.7), violates Lorentz invariance.

Alternatively, we can use the SME. If we restrict ourselves to rotationally-invariant interactions in a Sun-centered frame, with the only non-zero components of the tensorial interaction coefficients being the time components, we have a class of models known as “fried-chicken” models [1]. We also make the simplification of a two neutrino system, with $\nu_\mu \leftrightarrow \nu_\tau$ oscillations, borrowing from the precedence set by mass-induced oscillations. There is no a priori reason why this would have to be the case, but we are looking for a disappearance of ν_μ . If a deficit of muon neutrinos with energy and zenith angle dependence consistent with this model were found, it would still be necessary to test the prediction that they were oscillating to ν_τ . The result of these assumptions is a 2×2 matrix c_L^{TT} . Physically, the eigenvalues of this matrix can be interpreted as a new set of eigenstates, each state with a different limiting velocity that is slightly less than the speed of light in vacuum. These new eigenstates are referred to as Maximum Attainable Velocity (MAV) eigenstates.

Another approach [22, 31] is to use a Lorentz-violating Hamiltonian with ar-

bitrary energy-dependence for some new physics:

$$H_{\pm} = \frac{\Delta m^2}{4E} U_{\theta} \begin{pmatrix} -1 & 0 \\ 0 & 1 \end{pmatrix} U_{\theta}^{\dagger} + \sum_n \sigma_n^{\pm} \frac{\Delta \delta_n E^n}{2} U_{\xi_n, \pm \eta_n} \begin{pmatrix} -1 & 0 \\ 0 & 1 \end{pmatrix} U_{\xi_n, \pm \eta_n}^{\dagger}. \quad (3.3)$$

The first term on the right-hand side is the familiar mass-induced mixing, the second term is the Lorentz, and possibly also CPT violating, mixing. σ_n^{\pm} allows for a possible sign difference (CPT violating effect) between neutrinos (+1) and anti-neutrinos (-1), and $\Delta \delta_n$ is the strength of the new physics terms. The mixing matrix for the new physics is

$$U_{\xi_n, \pm \eta_n} = \begin{pmatrix} \cos \xi_n e^{-i\eta_n} & \sin \xi_n e^{\pm i\eta_n} \\ -\sin \xi_n e^{\mp i\eta_n} & \cos \xi_n e^{-i\eta_n} \end{pmatrix}. \quad (3.4)$$

If the new physics interaction (parameterized by the $\Delta \delta_n$) is constant along the neutrino path, the equation for oscillation survival probability becomes [22, 31]

$$P_{\nu_{\mu} \rightarrow \nu_{\mu}} = 1 - \sin^2 2\Theta \sin^2 \left(\frac{\Delta m^2 L}{4E} \mathfrak{R} \right), \quad (3.5)$$

where

$$\mathfrak{R} = \sqrt{1 + R_n^2 + 2R_n (\cos 2\theta \cos 2\xi_n + \sin 2\theta \sin 2\xi_n \cos \eta_n)}, \quad (3.6)$$

$$\sin^2 2\Theta = \frac{1}{\mathfrak{R}^2} (\sin^2 2\theta + R_n^2 \sin^2 2\xi_n + 2R_n \sin 2\theta \sin 2\xi_n \cos \eta_n), \quad (3.7)$$

and

$$R_n = \sigma_n^{\pm} \frac{\Delta \delta_n E^n}{2} \frac{4E}{\Delta m^2}. \quad (3.8)$$

R_n is the ratio of the new physics oscillation length to the standard oscillation length. \mathfrak{R} is the ratio of the effective oscillation length to the standard oscillation length.

If the new oscillations are caused by neutrino eigenstates with different MAV, then the notation used for the physics parameters is $\Delta\delta_1 = \delta c/c$, (the fractional difference in these MAVs relative to the speed of light), and a mixing angle $\xi_1 = \theta_c$. In this case, the ratio between VLI and mass-induced oscillation wavelengths is

$$R = \frac{\delta c}{c} \frac{E}{2} \frac{4E}{\Delta m^2}. \quad (3.9)$$

If we assume that mass-induced and VLI oscillations are maximal (i.e. $\theta_c = \theta = \pi/4$), then Eqn. 3.5 becomes

$$P_{\nu_\mu \rightarrow \nu_\mu} = 1 - \sin^2 \left(\frac{\Delta m^2 L}{4E} + \frac{\delta c}{c} \frac{LE}{2} \right). \quad (3.10)$$

We will use Eqn. 3.5 for the likelihood analysis, with physics parameters θ_c and $\delta c/c$. The phase η is assumed to be zero. Since mass-induced oscillations are suppressed at the energy scale of this analysis, interference between mass-induced and VLI oscillations is negligible. Fig. 3.1 shows the ν_μ survival probability as a function of neutrino energy and zenith angle for the case $\delta c/c = 10^{-27}$ and $\sin^2(2\theta_c) = 1$.

In addition to the $n = 1$ case just discussed, we can generalize this model to arbitrary integral powers of the neutrino energy. The notation (and energy dependence) is then

$$\frac{\delta c}{c} \rightarrow \Delta\delta_n, \text{ and } E \rightarrow E^n. \quad (3.11)$$

The units of $\Delta\delta_n$ are GeV^{-n+1} . An $n = 2$ energy dependence has, for example, been proposed in phenomenological models based on loop quantum gravity [71], or non-renormalizable VLI effects induced by a spacetime foam [72].

If there is non-universal coupling of neutrino eigenstates to a gravitational potential φ , i.e. $\gamma_1 \neq \gamma_2$, where γ_i is the gravitational coupling for eigenstate i , then

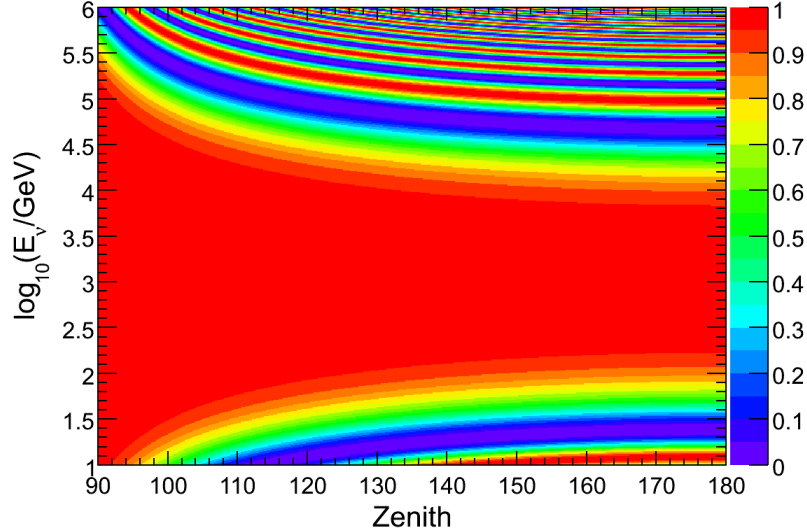


Figure 3.1: Atmospheric muon neutrino survival probability for $n = 1$ VLI model with $\delta c/c = 10^{-27}$ and $\sin^2(2\theta_c) = 1$. The color scale represents the oscillation survival probability. Oscillations visible below about 100 GeV are due to mass-induced oscillations.

the EP is violated [24]. If the gravitational potential is constant along the neutrino path, then this VEP model is phenomenologically equivalent to VLI [19, 73], with the transformation $\delta c/c \rightarrow 2|\varphi|\delta\gamma$. Models with $n = 1$ and $n = 3$ energy dependencies have been associated with VEP [24, 26, 27].

Fig. 3.2 shows the sensitivity of 40-string IceCube to the $n = 1$ VLI model, for the live time of this analysis. This sensitivity estimate, as well as similar plots to follow, is based on a χ^2 analysis with no accounting for systematic uncertainties. The method is similar to that used in [31] to estimate the sensitivity of the 80-string configuration, but different binning is used here. Events are binned in ten $\cos\theta_Z$ bins from -1 to 0 , and ten dE/dX bins from -2 to 1 (dE/dX is an energy dependent observable that will be discussed later). For comparison, Fig. 3.3 shows

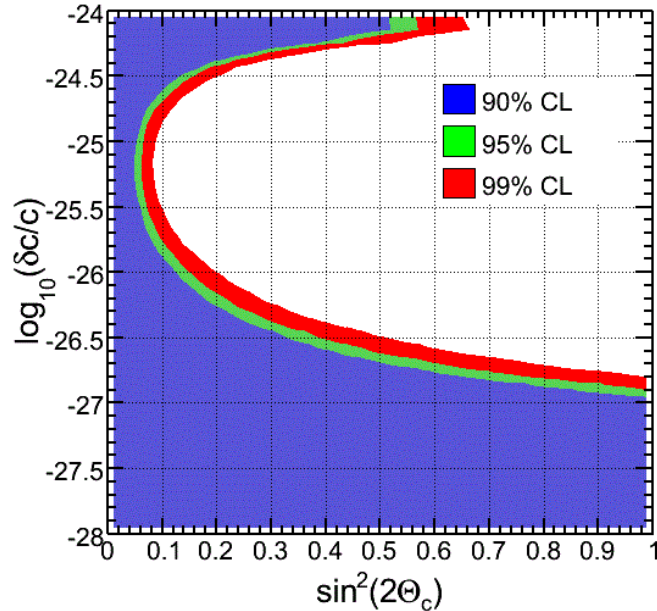


Figure 3.2: Predicted sensitivity of 40-string detector to $n = 1$ VLI oscillations.

the sensitivity after a cut at $\theta_z > 97^\circ$. The reason for this cut will be discussed in Chapter 8. Fig. 3.4 shows the sensitivity for the $n = 2$ VLI model and Fig. 3.5 shows the sensitivity for the $n = 3$ VLI model, (both plots based on the full 90 to 180 zenith coverage).

MACRO [74], Super-K [75], K2K, and AMANDA-II have set upper limits on this type of VLI model for neutrino oscillations with $n = 1$. For $\sin^2(2\theta_c) = 1$, a combined analysis of Super-K and K2K data [76] set an upper limit of $\delta c/c < 2.0 \times 10^{-27}$ at the 90% confidence level (CL). An upper limit of $\delta c/c < 2.8 \times 10^{-27}$ at the 90% CL was set with data from the AMANDA-II detector [77]. The AMANDA-II analysis was also used to set upper limits for the $n = 2$ and $n = 3$ models: $\Delta\delta < 2.7 \times 10^{-31}$ and $\Delta\delta < 1.9 \times 10^{-35}$ respectively. Fig. 3.6 shows the 90% CL

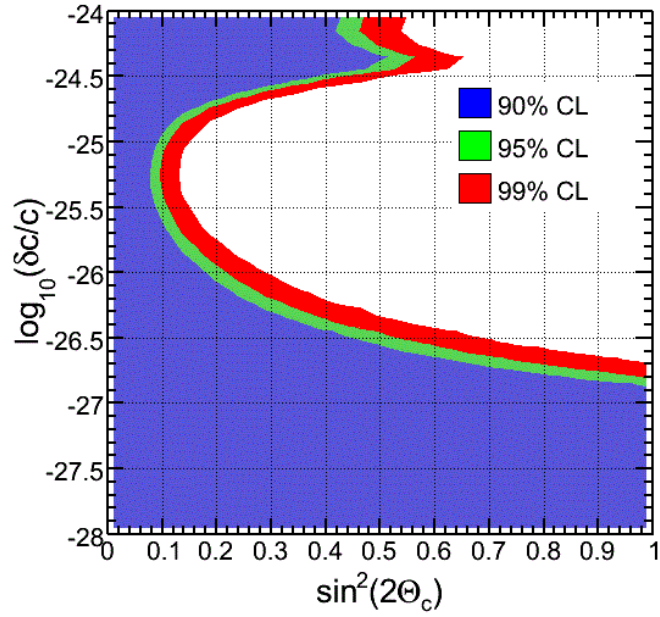


Figure 3.3: Predicted sensitivity of 40-string detector to $n = 1$ VLI oscillations after an additional cut at $\cos \theta_z < -0.12$.

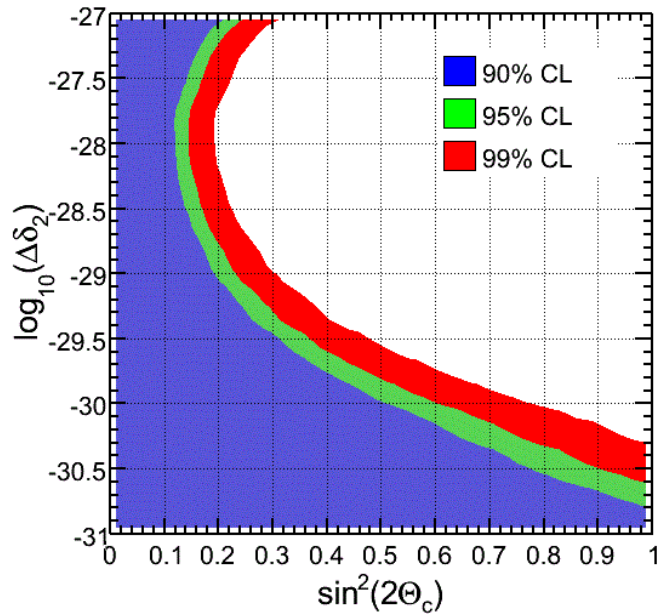


Figure 3.4: Predicted sensitivity of 40-string detector to $n = 2$ VLI oscillations.

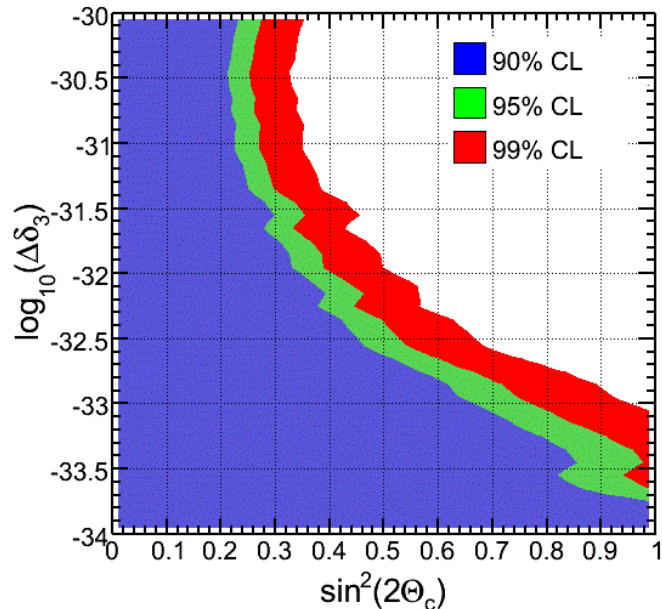


Figure 3.5: Predicted sensitivity of 40-string detector to $n = 3$ VLI oscillations.

limits set by AMANDA-II [77], and the combined Super-K + K2K analysis [76]. Also shown in Fig. 3.6 is a sensitivity estimate for 80-string IceCube [31].

3.2 Decoherence

Quantum fluctuations of spacetime can lead to a foam-like structure [78]. Interactions with this spacetime foam can also be thought of as interactions with virtual black holes [79], in which the virtual black holes pop in and out of existence on timescales allowed by the uncertainty principle. In scattering interactions with these virtual black holes, energy, angular momentum, and local or gauged quantum numbers (such as electric or color charge) would be conserved. Global quantum numbers may not be conserved. A neutrino would emerge from a scattering inter-

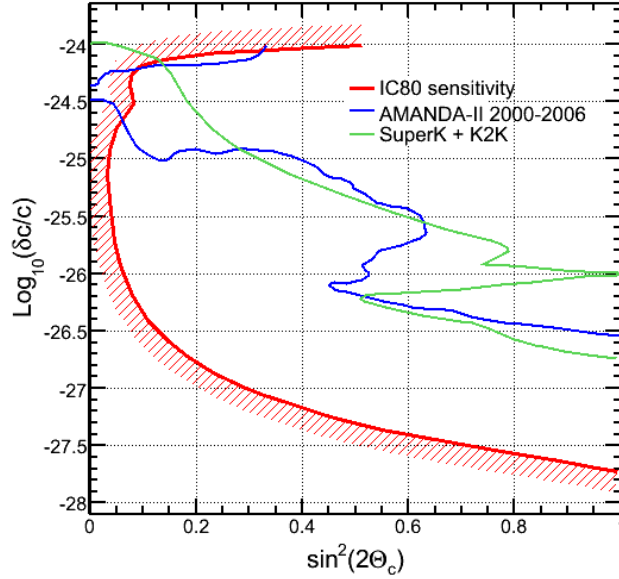


Figure 3.6: 90% CL limits for $n = 1$ VLI oscillations from AMANDA-II [77], and a combined Super-Kamiokande + K2K analysis [76]. Predicted sensitivity for 80-string IceCube from [31].

action with a virtual black hole as a neutrino, but lepton flavor may be different. Interactions with these virtual black holes could thus lead to randomization of neutrino flavor eigenstates.

These scattering processes are characterized by non-unitary scattering matrices and are not reversible in time. Pure quantum states evolve into mixed quantum states in irreversible processes that violate CPT symmetry. Transformations describing the time evolution of such open quantum systems are given by operators of Lindblad quantum dynamical semi-groups [80]. This approach does not require detailed knowledge of the environment, but it does maintain energy conservation, entropy increase, and complete positivity of the density matrix. The time evolution

of the density matrix is [81]

$$\frac{\partial \rho}{\partial t} = -i [H_{eff}, \rho] + D[\rho], \quad (3.12)$$

where the decoherence term is given by

$$D[\rho] = -\frac{1}{2} \sum_j \left([b_j, \rho b_j^\dagger] + [b_j \rho, b_j^\dagger] \right). \quad (3.13)$$

The operators b_j represent the interaction with the environment. The Lindblad part can not be written as a commutator; any environmental interactions that can be written in commutator form are part of H_{eff} .

Introducing a set of self-adjoint environmental operators A_j , the time evolution of the density matrix becomes [82]

$$\frac{\partial \rho}{\partial t} = -i [H_{eff}, \rho] + \frac{1}{2} \sum_j ([A_j, \rho A_j] + [A_j \rho, A_j]). \quad (3.14)$$

The dissipative term can be expanded in the Gell-Mann basis $F_\mu, \mu \in [0, 8]$ [82],

$$\frac{1}{2} \sum_j ([A_j, \rho A_j] + [A_j \rho, A_j]) = \sum_{\mu, \nu} L_{\mu\nu} \rho_\mu F_\nu. \quad (3.15)$$

For the decoherence model, we use a three-flavor model. The signatures of a two- or a three-neutrino flavor model are very similar, but there is no heuristic reason to assume that neutrinos would not decohere into all three flavors equally. Assuming the weak coupling limit in which $L_{\mu\nu}$ is diagonal, with $L_{00} = 0$ and $L_{ii} = -\gamma_i$, and neglecting mass-induced oscillations other than $\nu_\mu \leftrightarrow \nu_\tau$ mixing, leads to the probability for ν_μ survival (as a function of neutrino energy and propagation length)

[82, 83]

$$\begin{aligned}
P_{\nu_\mu \rightarrow \nu_\mu} = & \frac{1}{3} + \frac{1}{2} \left\{ e^{-\gamma_3 L} \cos^4 \theta_{23} + \frac{1}{12} e^{-\gamma_8 L} (1 - 3 \cos 2\theta_{23})^2 \right. \\
& + 4e^{-\frac{(\gamma_6 + \gamma_7)L}{2}} \cos^2 \theta_{23} \sin^2 \theta_{23} \left[\cos \left(\frac{L}{2} \sqrt{m'} \right) \right. \\
& \left. \left. + \sin \left(\frac{L}{2} \sqrt{m'} \right) (\gamma_6 - \gamma_7) / \sqrt{m'} \right] \right\}, \tag{3.16}
\end{aligned}$$

where

$$m' \equiv \left| (\gamma_6 - \gamma_7)^2 - (\Delta m_{23}^2 / E)^2 \right|. \tag{3.17}$$

The γ_i are characteristic length scales over which the decoherence occurs.

The intrinsic irreversibility of the decoherence process implies CPT violation [8]. Also, in general, the decoherence parameters for neutrinos could be different than for antineutrinos. We will assume they are the same. Further, we will set $\gamma_6 = \gamma_7$ and $\gamma_3 = \gamma_8$ to reduce the likelihood analysis to a two-parameter model. The survival probability then becomes

$$\begin{aligned}
P_{\nu_\mu \rightarrow \nu_\mu} = & \frac{1}{3} + \frac{1}{2} \left\{ e^{-\gamma_3 L} \cos^4 \theta_{23} + \frac{1}{12} e^{-\gamma_8 L} (1 - 3 \cos 2\theta_{23})^2 \right. \\
& \left. + 4e^{-\gamma_6 L} \cos^2 \theta_{23} \sin^2 \theta_{23} \cos(\Delta m_{23}^2 L / 2E) \right\}. \tag{3.18}
\end{aligned}$$

Fig. 3.7 shows the ν_μ survival probability as a function of neutrino energy and zenith angle for the case $\gamma_3 = \gamma_6 = \gamma_7 = \gamma_8 = 10^{-31}$ and $n = 2$. Note the 1/3 survival probability for the highest energies, since neutrino flavor has become fully randomized. To compare the relative contributions of the first and second terms on the right-hand side of Eqn. 3.18, Fig. 3.8 shows the ν_μ survival probability for $\gamma_3 = \gamma_8 = 10^{-31}$ with $\gamma_6 = \gamma_7 = 0$, and Fig. 3.9 shows the ν_μ survival probability for $\gamma_3 = \gamma_8 = 0$ and $\gamma_6 = \gamma_7 = 10^{-31}$.

The energy dependence of the decoherence terms can be generalized to integral

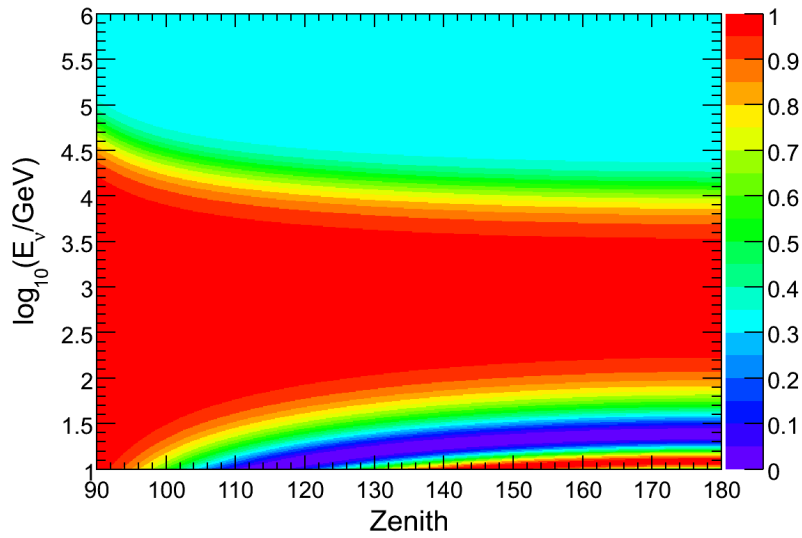


Figure 3.7: Atmospheric muon neutrino survival probability for $n = 2$ decoherence model with $\gamma_3 = \gamma_6 = \gamma_7 = \gamma_8 = 10^{-31}$. The color scale represents the decoherence survival probability. Oscillations below about 100 GeV are due to mass-induced oscillations. Note the 1/3 probability for the highest energies, where the flavor eigenstates are completely randomized.

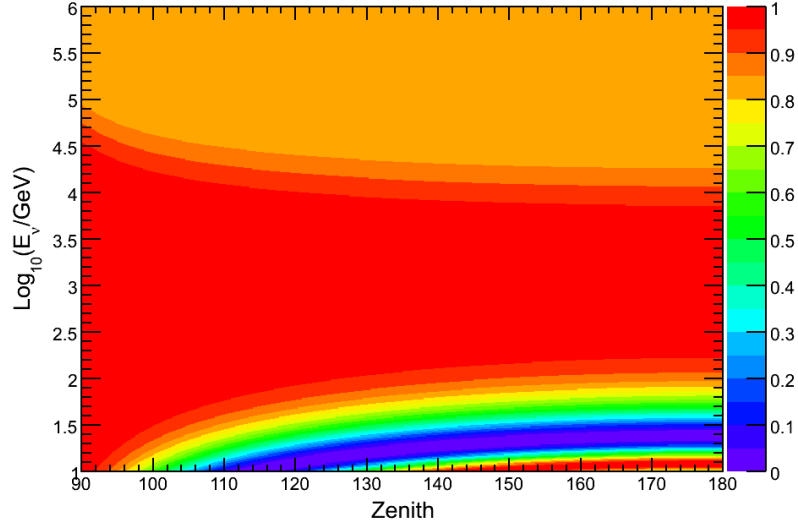


Figure 3.8: Atmospheric muon neutrino survival probability for $n = 2$ decoherence model for the 40-string detector. $\gamma_3 = \gamma_8 = 10^{-31}$ and $\gamma_6 = \gamma_7 = 0$. The color scale represents the decoherence survival probability. Oscillations below about 100 GeV are due to mass-induced oscillations.

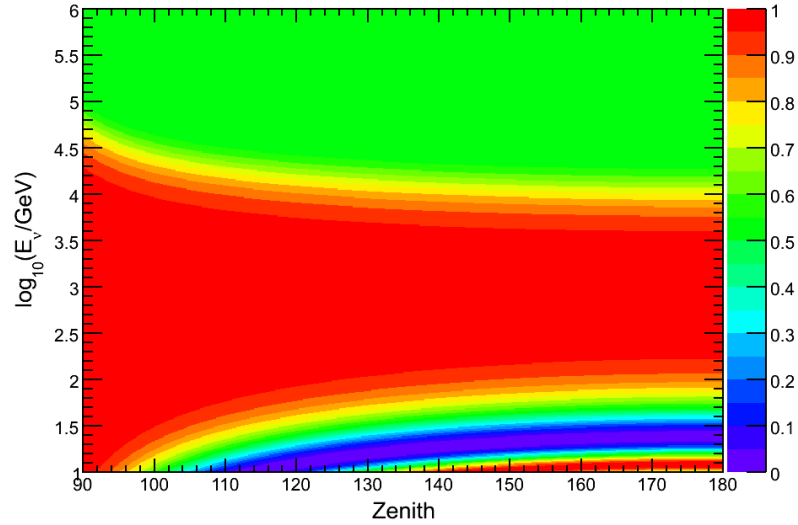


Figure 3.9: Atmospheric muon neutrino survival probability for $n = 2$ decoherence model for the 40-string detector. $\gamma_3 = \gamma_8 = 0$ and $\gamma_6 = \gamma_7 = 10^{-31}$. The color scale represents the decoherence survival probability. Oscillations below about 100 GeV are due to mass-induced oscillations.

powers of the neutrino energy:

$$\gamma_i = \gamma_i^* E_\nu^n, n \in [1, 3], \quad (3.19)$$

where the units of the γ_i^* are GeV^{-n+1} . The $n=2$ case, for example, arises in non-critical string theories [84, 85].

Fig. 3.10 shows the sensitivity of 40-string IceCube to the decoherence model with $n = 2$. For comparison, Fig. 3.11 shows the sensitivity after an additional cut at $\theta_Z > 97^\circ$. Fig. 3.12 shows the sensitivity for the $n = 1$ decoherence model. Fig. 3.13 shows the sensitivity for the $n = 3$ decoherence model. From the AMANDA-II analysis [77], upper limits were set for $\gamma_3^* = \gamma_8^* = \gamma_6^* = \gamma_7^*$ of 1.2×10^{-27} , 1.3×10^{-31} , and 6.3×10^{-36} , for $n = 1, 2$, and 3 , respectively. Using a two-flavor decoherence model, an upper limit of $\gamma^* < 9.0 \times 10^{-28} \text{GeV}^{-1}$ for $n = 2$, was set by Super-K [86].

3.3 Violation of Rotational Invariance

For this model, we start with the effective Hamiltonian for neutrino interactions in the SME (Eqn. 2.14). After some approximations applicable to the energies and propagation lengths for atmospheric neutrinos, a subset model known as the “vector model” can be derived [50]. This model is useful for looking for sidereal variations in the atmospheric neutrino flux. Under this model, the only non-zero coefficients are the real components of $(a_L)_{\mu\tau}^X$, $(a_L)_{\mu\tau}^Y$, $(c_L)_{\mu\tau}^{TX}$, and $(c_L)_{\mu\tau}^{TY}$. These assumptions are made in a Sun-centered frame for experimental convenience. Corrections due to the motion of the Earth around the sun ($\beta \approx 10^{-4}$), or relative to the cosmic microwave background ($\beta \approx 10^{-3}$), are ignored.

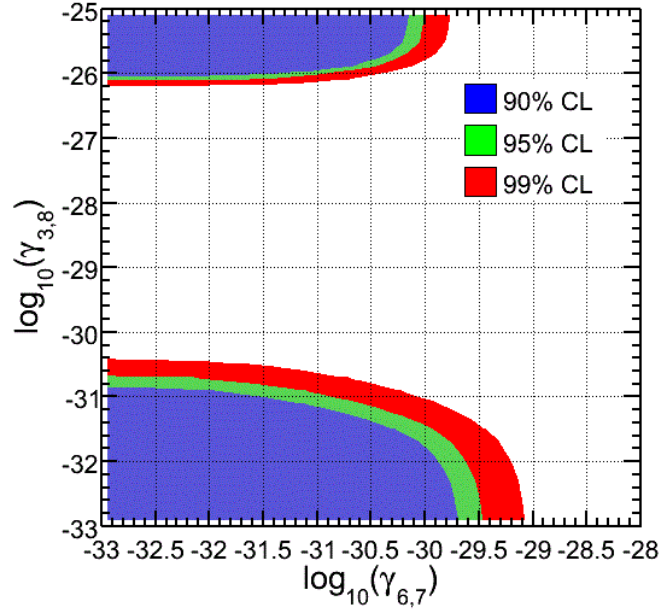


Figure 3.10: Predicted sensitivity for 40-string IceCube for the $n = 2$ decoherence model.

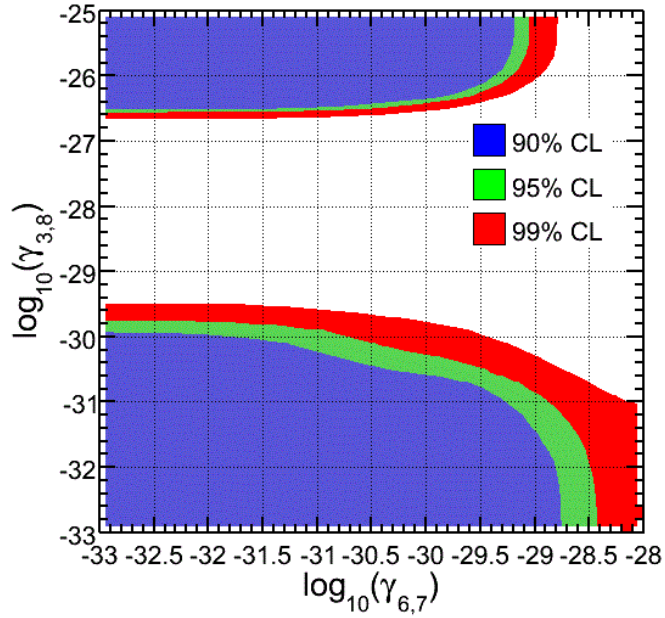


Figure 3.11: Predicted sensitivity for 40-string IceCube for the $n = 2$ decoherence model after an additional cut at $\cos \theta_z < -0.12$.

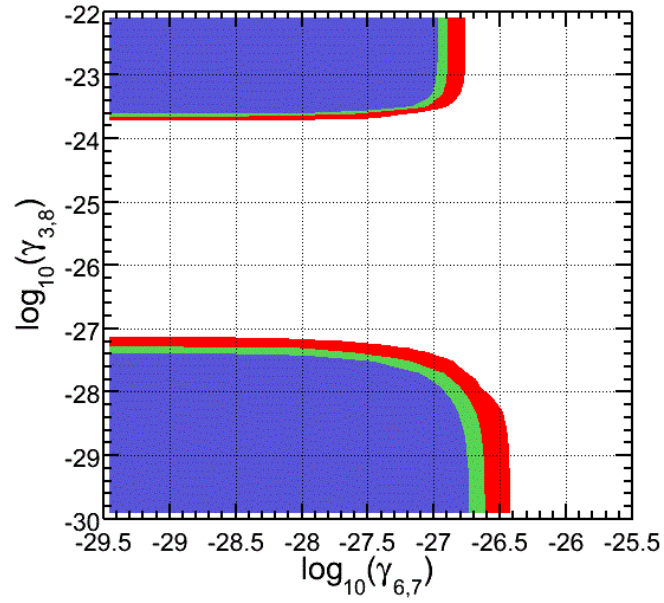


Figure 3.12: Predicted sensitivity for 40-string IceCube for the $n = 1$ decoherence model.

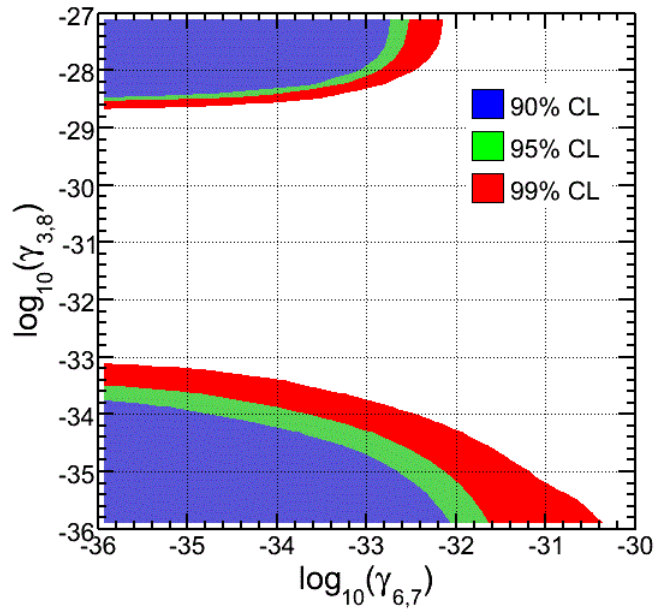


Figure 3.13: Predicted sensitivity for 40-string IceCube for the $n = 3$ decoherence model.

Under the vector model, the ν_μ survival probability is

$$P_{\nu_\mu \rightarrow \nu_\mu} = 1 - \sin^2 \left(L \left[(A_s)_{\mu\tau} \sin(RA + \varphi_0) + (A_c)_{\mu\tau} \cos(RA + \varphi_0) \right] \right), \quad (3.20)$$

where RA is the right ascension. Dropping the flavor subscripts,

$$A_s = \hat{N}^Y \left(a_L^X - 2E c_L^{TX} \right) - \hat{N}^X \left(a_L^Y - 2E c_L^{TY} \right), \quad (3.21)$$

and

$$A_c = -\hat{N}^X \left(a_L^X - 2E c_L^{TX} \right) - \hat{N}^Y \left(a_L^Y - 2E c_L^{TY} \right). \quad (3.22)$$

The $\hat{N}^{X(Y)}$ are unit propagation vectors for the neutrino:

$$\hat{N}^X = \sin(\theta) \cos(\varphi),$$

$$\hat{N}^Y = \sin(\theta) \sin(\varphi),$$

where $\theta = \pi/2 + \delta$ and $\varphi = \pi + \alpha$. δ is the declination of the incident neutrino and α its right ascension. The oscillation strength depends intrinsically on the direction that the neutrino propagates through space, violating rotational invariance. The survival probability for antineutrinos, $P_{\bar{\nu}_\mu \rightarrow \bar{\nu}_\mu}$, is given by changing the sign of the a_L coefficients.

Fig. 3.14 shows the ν_μ survival probability as a function of neutrino energy and RA for the case $a_L^X = 10^{-23}$ and $c_L^{TX} = 0$. Fig. 3.15 shows the ν_μ survival probability as a function of neutrino energy and RA for the case $a_L^X = 0$ and $c_L^{TX} = 10^{-27}$. In both figures, you can see the periodic structure of the survival probability, with power in the $n = 4$ mode of a Fourier transform. In Fig. 3.15, the oscillations don't kick in until higher energies, but then have a greater magnitude.

A Sun-centered celestial coordinate system, with z-axis aligned with the Earth's rotational axis and x-axis pointing towards the vernal equinox, is used. Given the

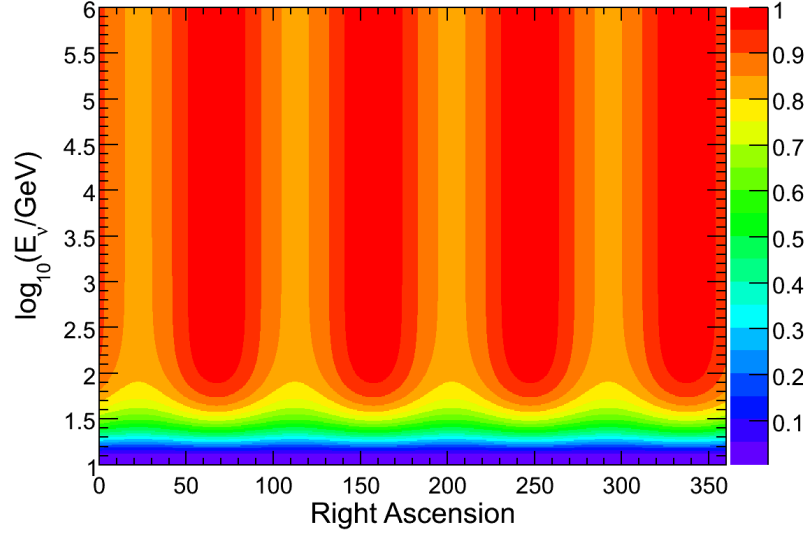


Figure 3.14: Atmospheric muon neutrino survival probability for the vector model with $a_L^X = 10^{-23}$ and $c_L^{TX} = 0$. The color scale represents the oscillation survival probability. Oscillations below about 100 GeV are mostly due to mass-induced oscillations.

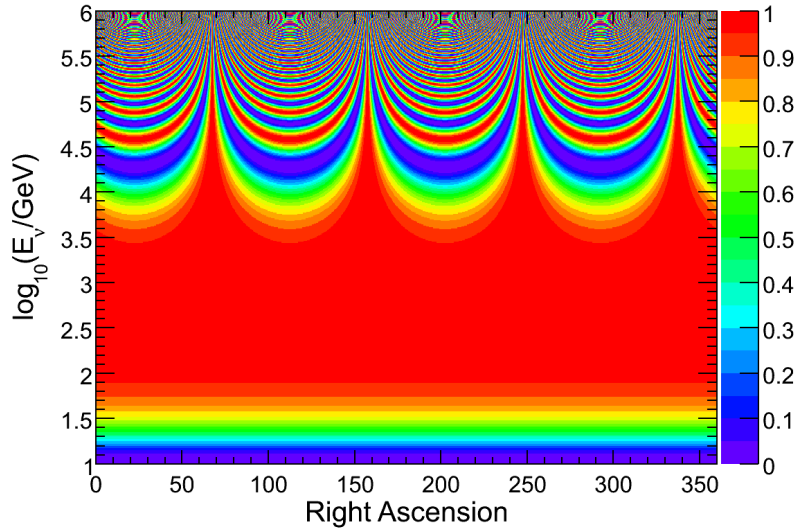


Figure 3.15: Atmospheric muon neutrino survival probability for the vector model with $a_L^X = 0$ and $c_L^{TX} = 10^{-27}$. The color scale represents the oscillation survival probability. Oscillations below about 100 GeV are due to mass-induced oscillations.

location of IceCube, zenith and azimuth are easily converted to declination and right ascension. An arbitrary offset (phase angle in right ascension) is allowed for the preferred direction, (the φ_0 in Eqn. 3.20).

Data from the LSND experiment was analyzed using a likelihood method [87]. No statistically significant modulation in sidereal time was found, but the allowed parameter range included values on the order of 10^{-19} GeV for a_L and for $E \times c_L$. A MINOS analysis [88] placed limits on the real components of a_L^X and $a_L^Y < 3 \times 10^{-20}$ GeV, as well as the real components of c_L^{TX} and $c_L^{TY} < 9 \times 10^{-23}$.

3.4 Additional Models

Two additional models of recent interest, testable with a likelihood analysis and atmospheric neutrinos, are discussed here. However, constraining these models does not necessarily benefit from the high energy reach of IceCube. Interesting results may be possible with the full IceCube detector, and DeepCore (see Chapter 4), which will extend the energy reach to lower values.

3.4.1 CPT Violating Oscillation of Antineutrinos

The possibility of CPTV oscillations of antineutrinos is motivated by some of the recent oscillation experiments (LSND, MiniBoone) [89]. Global fits of oscillation data imply there could be a unique mass-squared difference and mixing angle

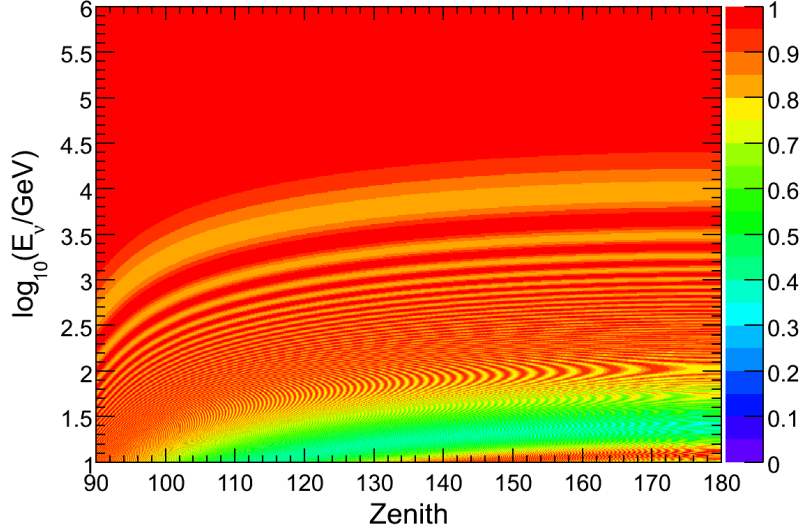


Figure 3.16: Atmospheric muon neutrino survival probability for CPTV oscillations of antineutrinos. The color scale represents the oscillation survival probability.

associated with muon antineutrino disappearance:

$$\begin{aligned} \Delta m_{CPTV}^2 &\sim 0.91\text{eV}^2, \\ \sin^2(2\theta_{CPTV}) &\sim 0.35. \end{aligned} \tag{3.23}$$

Fig. 3.16 shows the ν_μ survival probability as a function of neutrino energy and zenith angle for the case $\Delta m_{CPTV}^2 \sim 0.91\text{eV}^2$ and $\sin^2(2\theta_{CPTV}) \sim 0.35$. Below about 100 GeV, mass-induced oscillations of ν_μ and $\bar{\nu}_\mu$ are visible. Above about 100 GeV, only (CPTV) oscillations of $\bar{\nu}_\mu$ are occurring.

IceCube can not distinguish between neutrino and antineutrino events. We can, however, look for a net zenith and energy dependent deficit of events that could be the result of antineutrino disappearance. Fig. 3.17 shows the sensitivity of 40-string IceCube to this CPTV model, for the live time of this analysis. This plot is also based on the χ^2 calculation, with no accounting for systematic uncertainties.

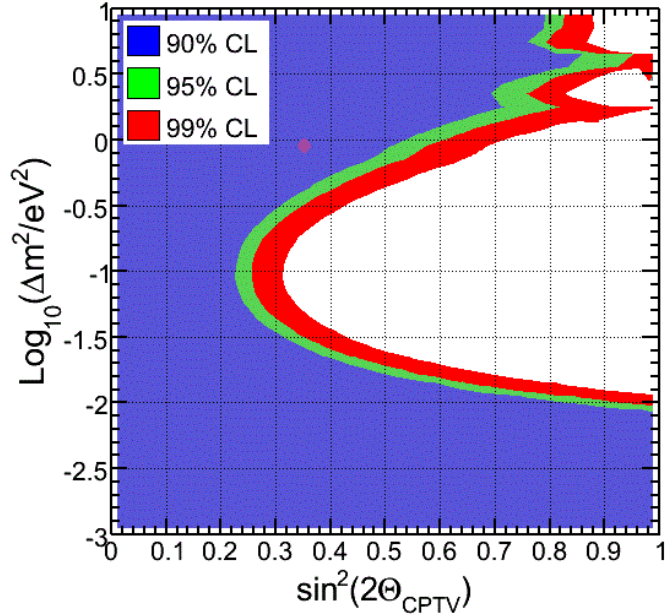


Figure 3.17: Predicted sensitivity to CPTV oscillations of antineutrinos. The purple diamond is the fit from [89].

40-string IceCube can not cover the best-fit values for the CPTV mixing parameters.

3.4.2 Bicycle Model

The bicycle model is another subset of the SME. This model attempts to reproduce the observed features of neutrino oscillations, but with massless neutrinos [1]. The non-zero elements of the relevant, tensorial interaction coefficients are $\frac{4}{3}(c_L)_{ee}^{TT} \equiv 2\hat{c} > 0$ and $(a_L)_{e\mu}^Z = (a_L)_{e\tau}^Z \equiv \tilde{a}/\sqrt{2}$. These assumptions are once again made in a Sun-centered frame.

With these assumptions, the ν_μ (and $\bar{\nu}_\mu$) survival probability is [1, 90]

$$\begin{aligned}
 P_{\nu_\mu \rightarrow \nu_\mu} = & 1 - \sin^2 \theta \sin^2 (\Delta_{21} L/2) \\
 & - \sin^2 \theta \cos^2 \theta \sin^2 (\Delta_{31} L/2) - \cos^2 \theta \sin^2 (\Delta_{32} L/2),
 \end{aligned}
 \tag{3.24}$$

where

$$\begin{aligned}
\Delta_{21} &= \sqrt{(\dot{c}E)^2 + (\tilde{a} \cos \Theta)^2} + \dot{c}E, \\
\Delta_{31} &= 2\sqrt{(\dot{c}E)^2 + (\tilde{a} \cos \Theta)^2}, \\
\Delta_{32} &= \sqrt{(\dot{c}E)^2 + (\tilde{a} \cos \Theta)^2} - \dot{c}E,
\end{aligned}
\tag{3.25}$$

and

$$\sin^2 \theta = \frac{1}{2} \left[1 - \dot{c}E / \sqrt{(\dot{c}E)^2 + (\tilde{a} \cos \Theta)^2} \right].
\tag{3.26}$$

Θ is the angle between the celestial north pole and the neutrino direction. It is also possible to generalize Θ , to be the angle between the neutrino's direction and some other preferred axis. It is convenient to define a critical energy $E_0 = |\tilde{a}|/\dot{c}$. For $E \gg E_0$, the oscillations reduce to $\nu_\mu \leftrightarrow \nu_\tau$ mixing, controlled by a direction-dependent pseudomass $\Delta m_\Theta^2 = \tilde{a}^2 \cos^2 \Theta / \dot{c}$.

Fig. 3.18 shows the ν_μ survival probability as a function of neutrino energy and zenith angle for the case $\tilde{a} = 10^{-23}$ and $\dot{c} = 10^{-26}$. Fig. 3.19 shows the ν_μ survival probability as a function of neutrino energy and zenith angle for the case $\tilde{a} = 10^{-22}$ and $\dot{c} = 10^{-25}$. Fig. 3.20 shows the sensitivity of 40-string IceCube for the bicycle model. An analysis of Super-K data [91] in the context of the bicycle model [49, 51] constrained E_0 to be less than 5 GeV at the 90% CL.

3.5 Constraining Quantum Gravity With Astrophysical Neutrinos

Just as cosmic rays and photons have intrinsic properties that can be exploited (i.e. charge and mass numbers for cosmic rays and polarization for photons), neutrinos have flavor. It may be possible to use neutrino flavor and flavor oscillations as specialized probes of spacetime, quantum gravity, and astrophysical objects.

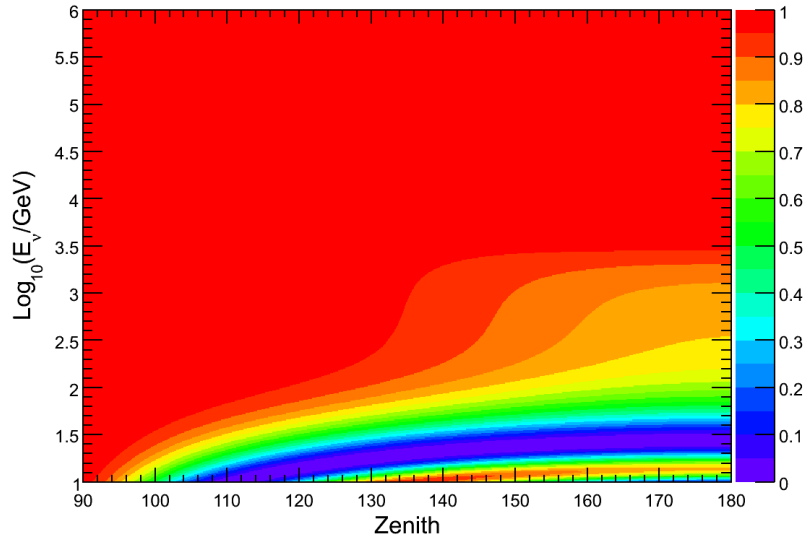


Figure 3.18: Atmospheric muon neutrino survival probability for the bicycle model, with physics parameters $\tilde{a} = 10^{-23}$ and $\tilde{c} = 10^{-26}$. The color scale represents the oscillation survival probability.

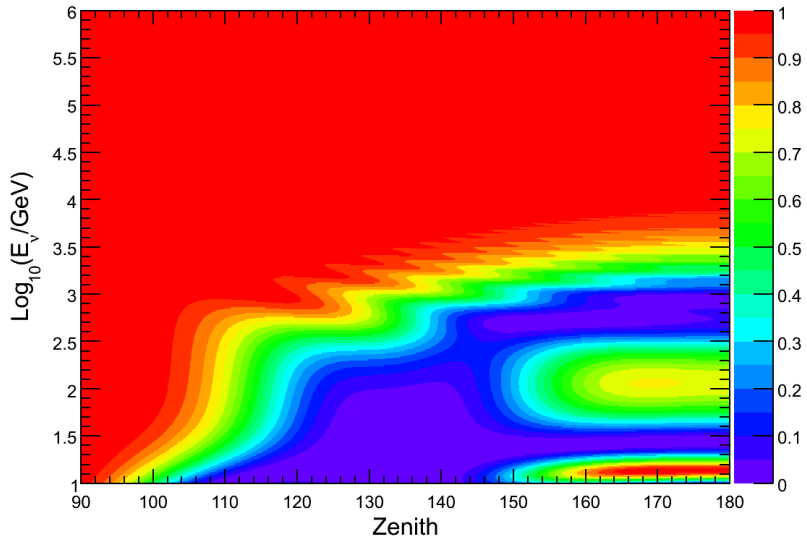


Figure 3.19: Atmospheric muon neutrino survival probability for the bicycle model, with physics parameters $\tilde{a} = 10^{-23}$ and $\tilde{c} = 10^{-26}$. The color scale represents the oscillation survival probability.

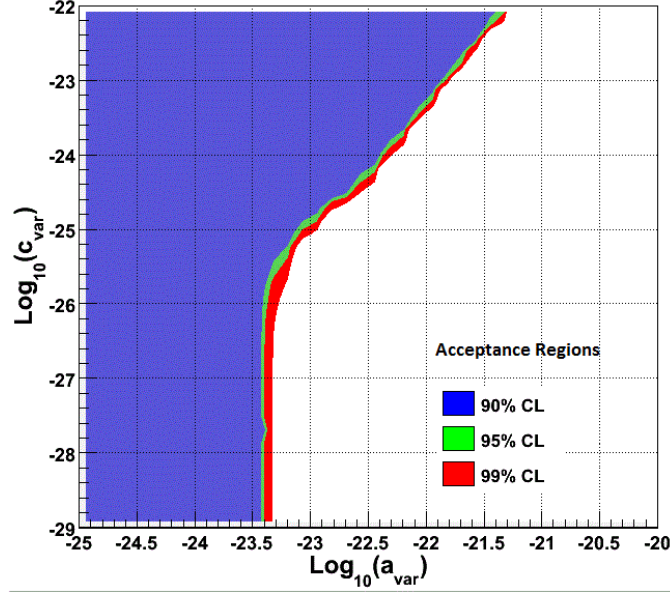


Figure 3.20: Predicted sensitivity to bicycle model for 40-string IceCube.

Flavor ratios for astrophysical neutrinos at their point of origin in cosmological sources should be 1:2:0 ($\nu_e : \nu_\mu : \nu_\tau$), due to the nature of their production via charged meson production and decay chains. Direct manufacture of tau neutrinos can occur in the decay chain of charmed mesons that are produced in the same hadronic interactions, but these quantities are significantly suppressed. If the propagation distance is large compared to the oscillation length, by the time neutrinos reach the Earth their flavor ratio will be modified to 1:1:1. Constraints could be placed on a Lorentz-violating model if a ratio other than 1:1:1 were detected from a distant astrophysical source. Anchordoqui, et al., [92], estimate that IceCube will be sensitive to quantum gravity-induced decoherence effects well below current experimental limits, as much as 17 orders of magnitude in some scenarios.

Anchordoqui, et al. [92], also suggest the use of the Cygnus spiral arm as a

source for which the initial neutrino flavor content and standard oscillation effects can be calculated. Some observations indicate that the Cygnus OB2 region may be a source of antineutrinos. In that case, they would not mix to a ratio of 1:1:1 in the standard oscillation model alone, over the distance of propagation. Observing a 1:1:1 ratio from this source may be an indication of some new oscillation or decoherence mechanism.

J. Christian [93] explored the predictions of various approaches to quantum gravity and the deviations from standard oscillation wavelengths that result from a modified dispersion relation. Effects that are suppressed by the square of the Planck mass may be observable through detection of ultra-high energy neutrinos that originate at cosmological distances [93].

Due to the temporal variability of some of the very distant and very energetic sources, such as AGN and GRB, detection of neutrinos from a known astrophysical source may enable precision tests of Lorentz invariance (i.e. different asymptotic values for the limiting speeds of different neutrino flavors) and the weak equivalence principle (i.e. different gravitational interactions for different neutrino flavors). This could be done by analyzing whether different flavors of neutrinos each have the same limiting speed and whether each experiences the same time delay passing through galactic gravitational fields. Due to increased energy coverage and event statistics, IceCube should be able to improve limits on violations of Lorentz invariance or the equivalence principle by two orders of magnitude using this method [94].

Chapter 4

The IceCube Neutrino Observatory

The IceCube Neutrino Observatory is actually three detectors working together. The design is a balance between energy resolution, angular resolution, energy range, and cost. A large detector is required due to extremely small cross-sections for neutrino interactions, as well as the low flux rates for astrophysical neutrinos. IceCube is optimized for the energy range 10^{11} to 10^{18} eV but will be sensitive to energies up to 10^{20} eV. IceCube is a cubic-kilometer of instrumented ice, deep in the South Pole glacial ice. DeepCore consists of six specialized, closely spaced strings of sensors at the center of IceCube, and IceTop is a surface array spanning the square kilometer over IceCube. The AMANDA neutrino telescope [95], operational from 1996 to 2009, was the predecessor and prototype for IceCube. AMANDA consisted of 677 optical modules on 19 strings, deployed between 1500 and 2000 m depth. In addition to being almost two orders of magnitude larger than AMANDA, IceCube uses improved photomultiplier tubes (PMT), improved time-stamping, and digitization of the waveforms. Fig. 4.1 shows the IceCube observatory and its component arrays.

IceCube will consist of eighty-six strings (counting the six DeepCore strings) of PMTs. Each string is one kilometer long and includes 60 digital optical modules (DOM). A DOM is a single PMT and associated electronics enclosed in a glass

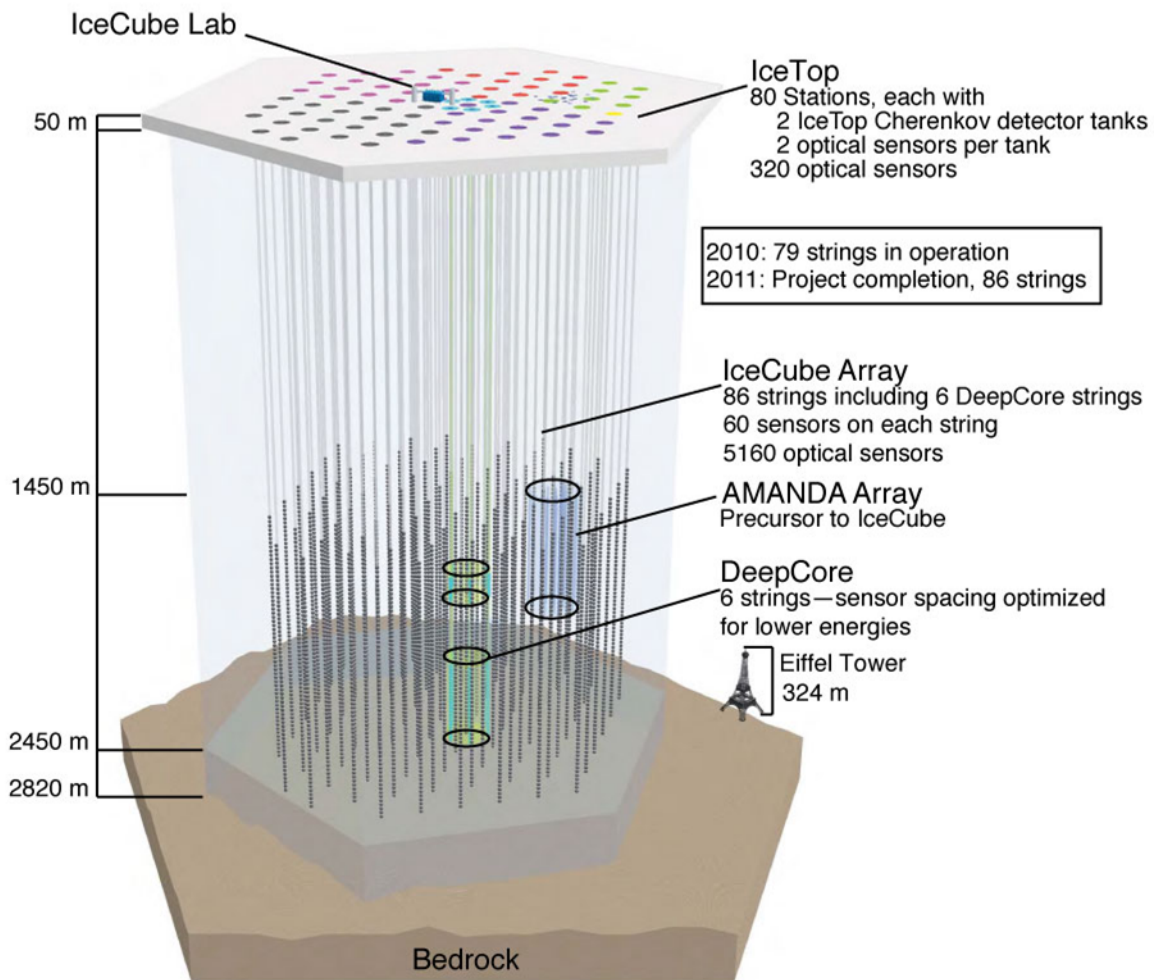


Figure 4.1: IceCube Neutrino Observatory and its component arrays.

pressure sphere. Vertical DOM spacing is 17 m for the eighty IceCube strings. Horizontally, the strings are 125 m apart and spread out in a hexagonal pattern over a square kilometer, so that the entire instrumented volume will be 1 km^3 of ice when construction is completed in 2011. The instrumented part of the array is between 1450 m and 2450 m below the surface of the ice. The bedrock is at a depth of 2800 m. The ice serves multiple roles: a stable platform for the DOMs, the propagation and detection medium for Cherenkov photons, and an overburden for attenuation of down-going atmospheric muons. At present, 79 strings are operational. This analysis is based on one year of data taken in the 40-string configuration.

The six DeepCore strings are closely spaced around the center IceCube string. These strings (and the seven around them) will contain high quantum efficiency DOMs optimized for low energy neutrino detection to push the detection threshold down to about 20 GeV. The DOMs on the DeepCore strings are more densely spaced below the dust layer (below about 2100 m). Surrounding strings will provide an active veto to allow 4π coverage for low energy neutrinos. The physics capabilities of DeepCore include lower neutrino energy reach for indirect searches for dark matter (including solar, galactic, and Earth core origins), studies of neutrino oscillation phenomenology, and searches for supersymmetric particles.

IceTop is a surface air shower detector covering 1 km^2 directly above IceCube. When complete, it will consist of 160 tanks, two near the location of each IceCube string (except for the DeepCore strings). Each 2.7 m^2 tank contains two DOMs frozen in ice to act as Cherenkov detectors. Two DOMs per tank provide redundancy and improved dynamic range. The two tanks are separated from each other

by 10 m, and offset from the in-ice hole by 25 m. IceTop will assist in the calibration of IceCube. Additionally, correlations with signals in IceTop can be used to reject background events. Cosmic ray physics with IceTop includes air shower measurements, measurements of the energy and mass of cosmic rays up to and beyond the knee, and measurements of the seasonal and directional variation of cosmic rays.

4.1 Construction

Construction of IceCube began in the 2004-2005 austral summer. Due to conditions at the South Pole, construction can only occur during a few months each year. In that first season, one IceCube string was deployed. Eight more strings were deployed in the 2005-2006 season, thirteen more during the 2006-2007 season, and eighteen during the 2007-2008 season. The strings became operational shortly after deployment, so data collection with a partially completed detector has been ongoing. A total of forty strings were available for collection of the data used in this analysis. An additional nineteen strings were deployed in the 2008-2009 season, and twenty more strings during the recently completed 2009-2010 season. Construction of the full detector should be completed by the end of the 2010-2011 season. Construction of the IceTop array has been ongoing in parallel with IceCube construction.

A firn drill is used to penetrate the snow layer. Then a hot water drill, called the “Enhanced Hot Water Drill”, is used to drill a 60 cm diameter hole through the ice, down to a depth of 2.4 km. A string of DOMs is then deployed into the hole and the DOMs freeze in place. In a small number of holes, a dust logger is deployed

and recovered prior to deploying the string of DOMs. The dust logger is a device for measuring the optical properties of the ice in the vicinity of the hole. Drilling takes about two days, and string deployment about 12 hours. Due to the natural thermocline in the ice, modules freeze-in from the top of the string down, and the process can take on the order of weeks before the last DOM is completely frozen in.

Due to the age and pressure of the ice, the ice below 1 km is essentially free of bubbles. Unfortunately, it does have some layers of dust and volcanic ash that lead to scattering of Cherenkov photons. Residual bubbles created in the drilling process and the interface between the original and refrozen ice can also change the optical properties around the DOM, causing scattering.

4.2 Digital Optical Modules

At the heart of each DOM is a 10 inch (25 cm) Hamamatsu PMT. The PMT is sensitive from 300 nm to 600 nm, with peak sensitivity around 420 nm. Associated electronics for operation and control, as well as local amplification, filtering, calibration and testing, are located on round circuit boards that are supported by the neck of the PMT. All this is housed inside a 35.6 cm glass pressure housing. The PMT has a spherical photocathode that rests in a silicone gel, which provides optical coupling to the glass pressure housing. The PMT also has ten dynodes and operates in the voltage range 1200 to 1400 V, for a gain of about 10^7 . A mu-metal wire cage around the photocathode provides magnetic shielding. The Hamamatsu PMT has a peak quantum efficiency of 0.25 at 390 nm and was chosen for its low

dark noise rate and good timing and charge resolution for single photons.

DOMs are designed to operate over a wide dynamic range, from a single photon to several thousand photons arriving within a few microseconds. The DOMs have been designed and tested to withstand the enormous forces and extremes of temperature experienced once deployed in the ice and have a fifteen year design life. So far, the survival rate for DOMs has been 98%. They are rigorously tested before shipping to the South Pole. All subsystem components are tested, and performance tests of fully assembled DOMs are performed. These performance tests subject the DOMs to the pressure and temperature variations they will see in the field, as well as the range of operations and signals they will need to process in the field.

Fig. 4.2 shows the PMT inside an assembled DOM. In addition to a mainboard (MB), each DOM contains a flasher board. The flasher boards contain twelve LEDs pointing radially outward. Six of the LEDs are horizontal and six point upwards at a 48° angle. These flashers are used to send light pulses between DOMs on the same string or on different strings, for timing and geometry calibration, energy reconstruction calibration, and for measuring the optical properties of the ice.

A DOM cable connects to a surface junction box located between the two associated IceTop tanks. Cables from the IceTop DOMs also connect to this junction box. Cabling between each of the surface junction boxes relays data to the central counting house, as well as provides power, timing, configuration and control signals back to the DOMs. $\pm 48\text{VDC}$ is provided to the DOMs via these cables.

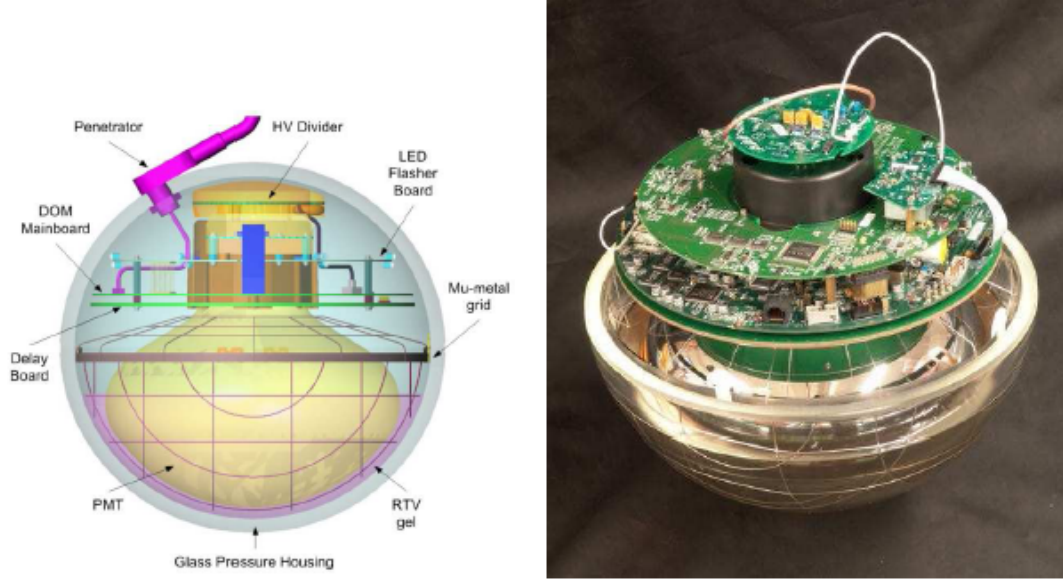


Figure 4.2: Digital Optical Module (DOM).

4.3 Electronics and Data Acquisition

Two methods are used for digitization of signals from the PMTs, to provide the desired resolution as well as time coverage and dynamic range [96]. An Analog Transient Waveform Digitizer (ATWD) records precise timing information of photons. It captures the same signal in three channels using three different gains. Each of the three channels includes 128 bins, with sampling at 300 MHz. The three ATWD channels, with gains differing by successive factors of eight, (0.25x, 2x, and 16x), cover a dynamic range up to 400 PE/15 ns. A fourth ATWD channel is used for calibration and monitoring. Two identical ATWDs are used alternately to eliminate dead time during readout. Longer duration signals are sampled at 40 MHz by a fast Analog to Digital Converter (fADC). 256 samples allows signals up to 6.4 μ s to be digitized.

4.4 Calibration and Verification

4.4.1 Timing

The Reciprocal Active Pulsing (RAPCal) procedure periodically synchronizes the surface time (based on a master, GPS-controlled oscillator) to the local DOM time (based on a local 20 MHz oscillator). These calibrations are done automatically every two seconds. First, the DOM Readout (DOR) card sends a short pulse to the DOM. By the time the waveform is received at the DOM, it has dispersed to microsecond length and the waveform can be sampled at the relatively slow 20 MHz communications rate. The DOM digitizes this pulse and records the arrival time. The DOM then waits a known amount of time and transmits an identical pulse, and the digitized pulse and arrival time, to the DOR card. The DOR card then digitizes and time-stamps the waveforms it receives. By comparing global and local timestamps for the two pulses, the timing offset can be determined. The ratio of the time interval between successive pulses transmitted by the DOR card to the time interval of successive pulses transmitted by the DOM gives the ratio of the frequency of the local oscillator to the frequency of the master oscillator. Improved precision is achieved by exploiting the reciprocity in the DOR-to-DOM and DOM-to-DOR transmission paths.

4.4.2 Digital Optical Modules

DOM-specific calibrations of the ATWD sampling frequency and voltage scale have to be performed, as well as measurements of the gains of the three ATWD

channels. The PMT gain response to anode-photocathode voltage is different for each DOM. This has to be measured and the proper voltage setting to achieve the desired gain has to be determined. These functions are accomplished periodically with a program called DOM-Cal that runs on the embedded DOM CPU.

DOM-Cal varies the ATWD bias voltage and determines the unique slope (V/ADC counts) and intercept for each ATWD bin [97]. The amplifier gains for each ATWD channel are determined in a two-step process. First, the high-gain channel is calibrated by using an artificial, single photoelectron (SPE)-like pulse of a known amplitude. This pulse (charge stored on a capacitor) is injected into the PMT cable connector on the DOM MB. The peak amplitude of the ATWD output is compared to the known pulse level. For the medium and lowest gain channels, light pulses from LEDs on the DOM MB generate the PMT signals. ATWD data is acquired for the channel to be calibrated as well as for the next higher-gain channel that has already been calibrated. The medium and lowest gain channels are thus calibrated in a boot-strap method, which is necessary so that an LED pulse amplitude can be chosen that will not saturate the higher gain channel yet provide sufficient amplitude in the lower gain channel.

To determine the PMT response to single photoelectrons as a function of high voltage setting, measurements are performed at high voltage settings from 1200 V to 1900 V in 100 V increments. At each setting, several thousand waveforms are captured, integrated, and converted to total charge. The gain is determined by fitting the charge spectrum to a Gaussian plus exponential function. Noise in the DOMs results from thermal background of the photocathode and radioactive decay

of contaminants in the glass pressure sphere. The exponential function describes this noise while the Gaussian describes the SPE response. The appropriate PMT voltage to achieve the desired gain is determined from calculations of the gains at each high voltage setting.

4.4.3 Geometry

The objective of geometry calibration is to determine the relative positions of all DOMs to within one meter. Geometry calibration is done in three stages: Stage 1 uses deployment data and surveys for a preliminary geometry released before station closing; Stage 2 involves fitting relative depths between strings using flasher data; Stage 3 (muon tomography) uses down-going muon data to track global changes in the relative geometry over time. The end product is a set of 3-dimensional coordinates for all DOMs (in-ice and IceTop) in the IceCube coordinate system.

The Stage 1 geometry uses data collected during string deployment and a pre-deployment survey of the drill tower. Deployment data includes pressure readings converted to water depth, distance from tower floor to water surface measured manually with a laser ranger, and DOM spacing measured manually with a laser ranger for every DOM pair. Pre-deployment survey data includes coordinates of the drill tower corners and coordinates for the center of the hole. Horizontal drift of the hole is reconstructed from inclinometer data from the drill head.

The Stage 2 geometry calibration uses inter-string flasher data to determine relative depth offsets between the strings. The offsets are relative to the Stage 1

geometry. The source (a flashing DOM) and the receiver DOMs are on different strings. Typically, data are taken for a few flashers on every string, and for every run all adjacent strings (up to six) are read out.

The Stage 3 geometry calibration uses muon tomography to track deformations of the array over time due to ice shear. The advantage over inter-string flasher measurements (the Stage 2 geometry calibration) is that DOMs can be tracked individually with muons whereas the inter-string fits typically assume straight strings. The disadvantage is that it relies on track reconstruction and is therefore subject to reconstruction systematics.

4.5 Ice Properties

The ice sheet is 2820 m thick and was created over a period of roughly 165,000 years [98]. The firn is the top 100 m of loosely packed snow. Optical properties of the ice are discussed in [99, 100, 101]. Scattering in the glacial ice is dominated by sub-millimeter air bubbles and micron-sized dust grains. Absorption is due to the intrinsic absorption properties of pure ice as well as absorption on dust grains. Variations with depth are due to the periodic build up of dust that resulted from the prevailing atmospheric conditions and climatological events that occurred while the layers of ice were being formed. There are layers of cleaner and dirtier ice, including a significant dust layer at 2050 m.

Shallower than about 1400 m, air bubbles trapped in the ice dominate the scattering. The mean free path for scattering on bubbles increases with depth as

bubbles are compressed with increasing pressure. Below 1400 m, a phase transition occurs and air bubbles become a solid air hydrate phase in which the gas molecules are trapped within the crystalline ice. The refractive index of these is approximately the same as the ice and the scattering they cause becomes negligible. Hence, below 1400 m scattering is dominated by the dust.

Absorption length λ_a is the distance over which photon survival probability drops by a factor of e . Scattering length λ_s is the average distance a photon travels between scatterings. The average mean angular change after multiple scattering interactions is denoted $\langle \cos \theta \rangle$. For Mie scattering, where the photon wavelength is comparable to the particle size, the scattering is peaked in the forward direction and $\langle \cos \theta \rangle \approx 0.94$ [99]. The effective scattering length, λ_e , is the distance after which a photon has its direction randomized. After n scatters, the effective displacement along the original direction is given by

$$\lambda_e = \lambda_s \sum_{i=0}^n \langle \cos \theta \rangle^i. \quad (4.1)$$

For large n , this is

$$\lambda_e = \frac{\lambda_s}{1 - \langle \cos \theta \rangle}. \quad (4.2)$$

Fig. 4.3, shows the depth and wavelength dependence of scattering and absorption as measured in the ice around the AMANDA detector. $a = 1/\lambda_a$ is the absorptivity, and $b_e = 1/\lambda_e$ is the scattering coefficient. Fig. 4.4, shows the depth dependence of scattering and absorption for photons with wavelength of 400 nm, a representative wavelength for Cherenkov photons detected by the DOMs. Ice properties were extrapolated to lower depths using ice core measurements taken at

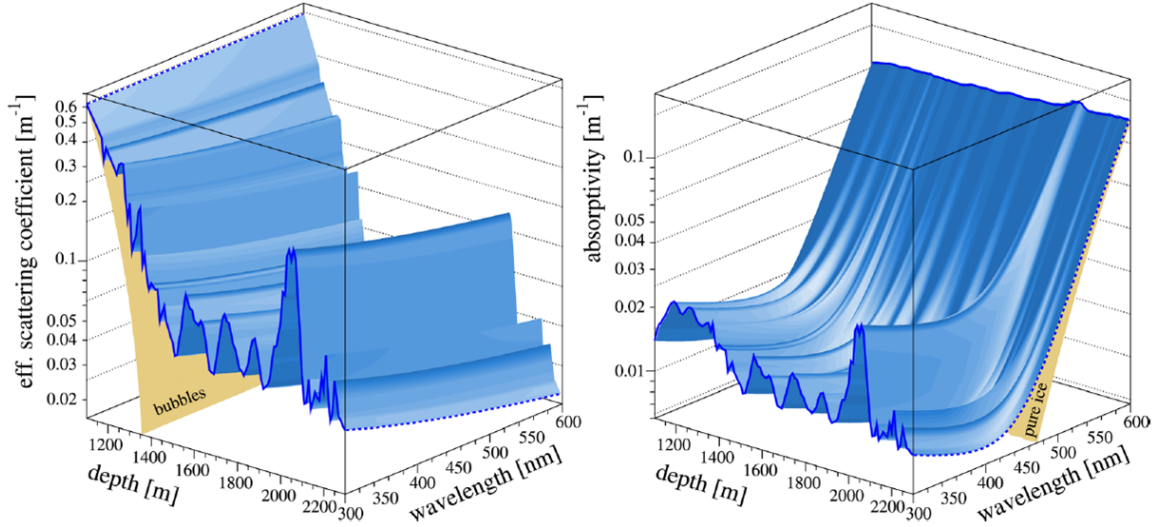


Figure 4.3: Optical properties of deep South Pole ice. Left: effective scattering coefficient as a function of depth and wavelength. Right: absorptivity as a function of depth and wavelength. From [99].

Vostok Station and Dome Fuji in Antarctica, and scaled to the location of IceCube using an age vs. depth relation [98]. The effective scattering length in IceCube varies from about 10 to 50 m. The absorption length is typically around 100 m.

The depth dependence of scattering has also been measured with a dust logger deployed down a small number of IceCube holes prior to deploying the strings of DOMs [102]. A dust logger is a compact and recoverable instrument used to measure ice properties in the vicinity of the hole. A collimated light source is located at one end and a PMT at the other. The PMT measures light that is back-scattered into the hole. Studies are on-going that use the flashers on each DOM to directly measure ice properties and improve the ice model.

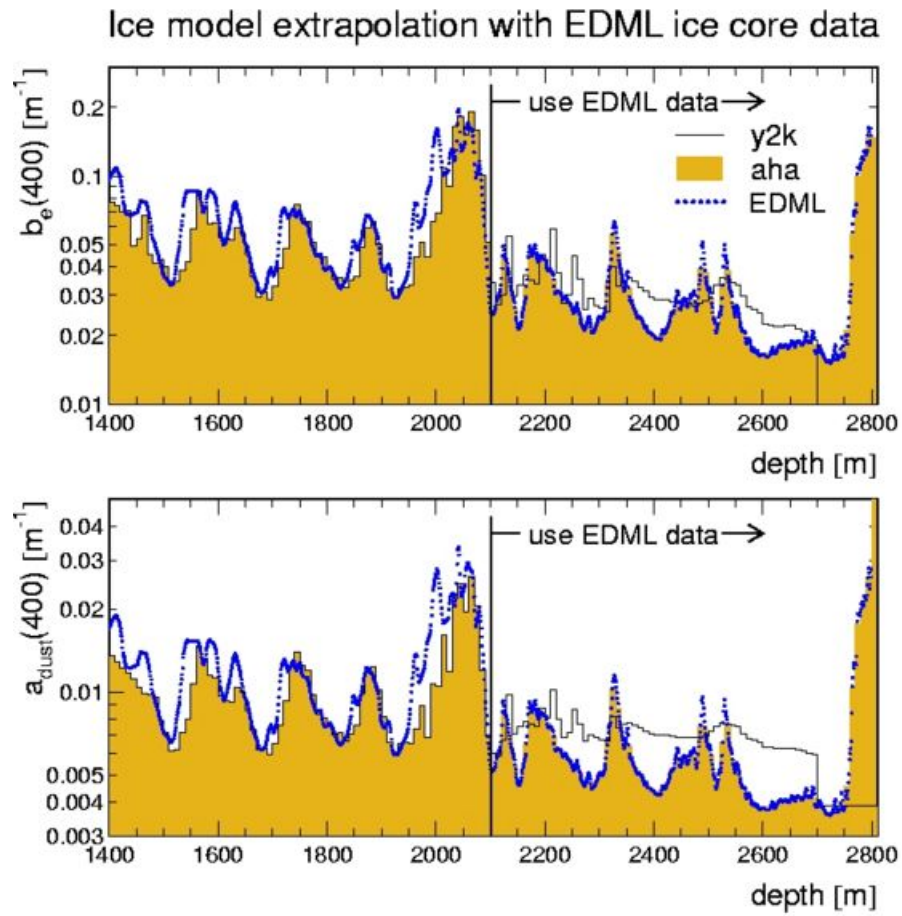


Figure 4.4: Scattering coefficients (top) and absorption (bottom) as function of depth, for light with wavelength of 400 nm. Extension of ice properties to greater depths using ice core data (right hand side).

Chapter 5

Neutrino Detection with IceCube

5.1 Neutrino-Nucleon Cross Sections

Neutrinos are detected, identified, and measured by their CC and NC interactions with nuclei in the ice. As mentioned in Chapter 2, CC interactions are mediated by the exchange of a W^\pm boson, NC interactions are mediated by the exchange of a Z^0 boson. CC and NC interactions on nucleons occur in the ratio of about 3 to 1 in the energy range of this analysis. A CC interaction between a neutrino and a valence or sea quark (q) contained within a nucleus in the ice is described by

$$\nu_l (\bar{\nu}_l) + q \rightarrow l^{-(+)} + q'. \quad (5.1)$$

If the incident neutrino is a muon neutrino, the resultant lepton is a muon. Examples of CC and NC neutrino-nucleon interactions can be seen in Fig. 5.1.

The type of scattering interaction most relevant for the energy range of this analysis is deep-inelastic scattering (DIS). The neutrino has enough energy to scatter from quarks or gluons, breaking up the nucleon. The quark gets an energy much greater than its binding energy in the nucleus it inhabits. Typically, it picks up a

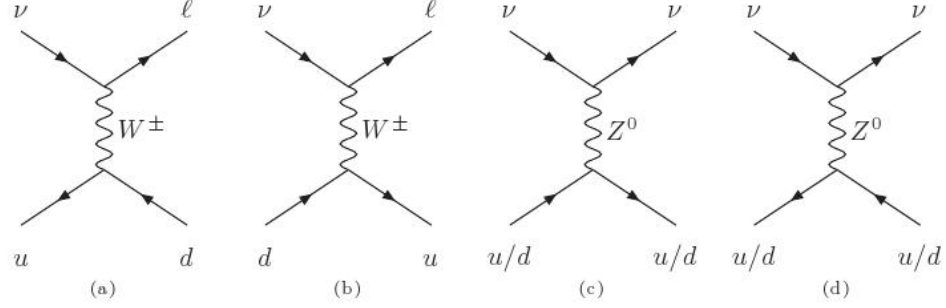


Figure 5.1: CC and NC neutrino-nucleon interactions. From IceCube Yellow Book.

$q\bar{q}$ pair from the vacuum and the resultant interaction can be

$$\begin{aligned} \nu_l (\bar{\nu}_l) + p &\rightarrow l^{-(+)} + n + \pi^0, \\ \nu_l (\bar{\nu}_l) + p &\rightarrow l^{-(+)} + p + \pi^{+(-)}, \end{aligned} \quad (5.2)$$

or similar interactions with a neutron in the initial state.

The CC DIS, neutrino-nucleon cross section is [103]

$$\frac{d^2\sigma}{dx dy} = \frac{2G_F^2 M E_\nu}{\pi} \frac{1}{(1 + Q^2/M_W^2)^2} [xq(x, Q^2) + x\bar{q}(x, Q^2)(1 - y)^2], \quad (5.3)$$

where G_F is the Fermi constant, $1.16632 \times 10^{-5} \text{ GeV}^{-2}$, and M is the nucleon mass. q and \bar{q} are the parton distribution functions (PDF) for quarks and antiquarks. These PDFs are linear combinations of the valence and sea quark distributions for each type of quark. For the NC cross section, the W-boson mass M_W is replaced by the Z-boson mass M_Z , and a different linear combination of quark distributions is used. Q^2 is the negative magnitude of the four-momentum transfer. The Bjorken variable x is the fraction of the nucleon momentum carried by the struck quark. The Bjorken variable y is the relative energy transfer from the incoming neutrino to the nucleon (via boson exchange).

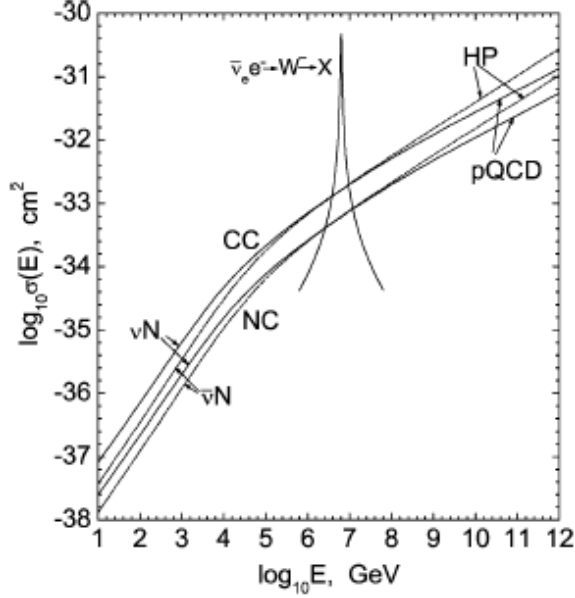


Figure 5.2: CC and NC cross sections, for neutrinos and antineutrinos. Computed with CTEQ5 PDFs [104]. The Glashow resonance at 6.3 PeV is at too high of an energy to be relevant for this analysis.

NC and CC cross sections, for neutrinos and antineutrinos, can be seen in Fig. 5.2 [104]. At low energies (less than about 450 GeV), the cross sections grow linearly with energy. That is because at low Q^2 , the $W(Z)$ -boson propagator and the PDFs are nearly independent of Q . At higher energies, the PDFs increase with Q^2 , but the boson propagator limits the value of Q^2 to roughly $Q^2 \sim M_{W(Z)}^2 \sim 10^4 \text{GeV}^{-2}$, limiting the overall cross section [105, 106]. Above a PeV, interactions with sea quarks dominate, and SM cross sections are the same for neutrinos and antineutrinos. Neutrino-electron interactions are negligible (except for the Glashow resonance at 6.3 PeV, which is not relevant for this analysis).

5.2 Cherenkov Radiation

High energy charged particles in IceCube are detected by the Cherenkov radiation that they emit. If the velocity of a charged particle in a particular dielectric medium exceeds the phase velocity of light in that medium, then it will emit Cherenkov radiation in a direction relative to the particle's track given by

$$\cos \theta_C = \frac{1}{n\beta}. \quad (5.4)$$

$\beta = v/c$, where v is the particle's velocity and c the speed of light in vacuum. n is the index of refraction which depends on frequency. For simulation in IceCube, we use values for the group and phase indices of refraction for the frequency of 400 nm. For $n_p \approx 1.32$, the Cherenkov angle is about 40.7° . Fig. 5.3 is a rendering of the Cherenkov light produced by a muon transiting through the detector.

The amount of Cherenkov light emitted by a particle along its path is given by the Frank-Tamm formula [107]

$$\frac{d^2 N}{dx d\lambda} = \frac{2\pi\alpha z^2}{\lambda^2} \left(1 - \frac{1}{\beta^2 n(\lambda)^2} \right), \quad (5.5)$$

where z is the particle's charge in units of the electron charge ($= 1$ for muons), and α is the fine structure constant. A muon traveling through ice with $\beta \approx 1$ emits around 330 Cherenkov photons per cm in the wavelength range accessible to IceCube.

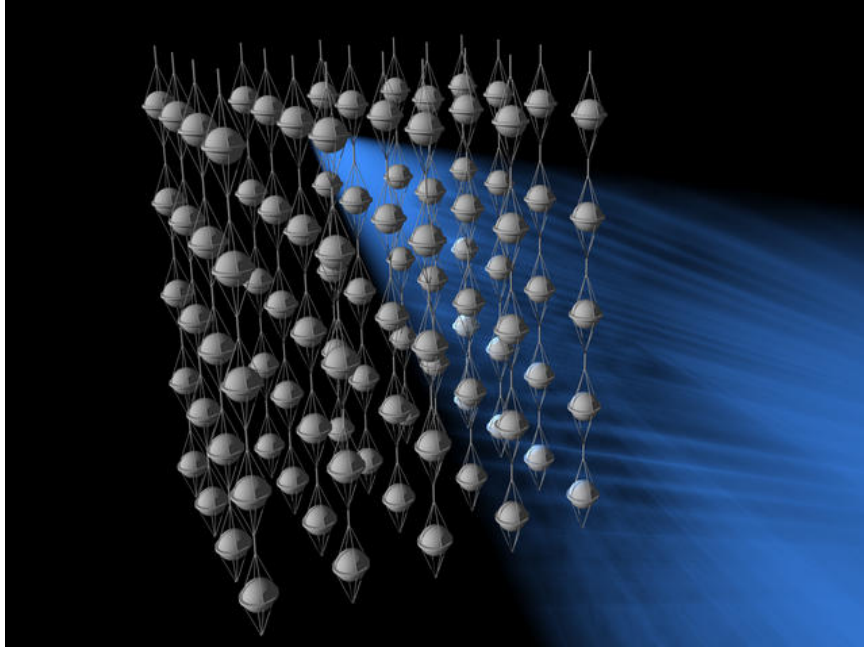


Figure 5.3: Artist's rendition of Cherenkov light in the IceCube detector.

5.3 Muon Propagation and Energy Loss

The energy loss during propagation of a charged lepton, in this case a muon, is given by [53]

$$-\left\langle \frac{dE}{dX} \right\rangle = \alpha(E) + \beta(E)E, \quad (5.6)$$

where E is the muon energy, α is the ionization energy loss per unit propagation length, and β is the radiative energy loss through bremsstrahlung, pair production, and photonuclear scattering. Technically, α and β are functions of energy, but for ice, their values are approximately $\alpha \simeq 0.2417 \text{ GeV m}^{-1}$ and $\beta \simeq 3.325 \times 10^{-4} \text{ m}^{-1}$.

The particles created in these stochastic processes can also exceed the speed of light in the ice. Hence, if charged, they also emit Cherenkov radiation and enhance the Cherenkov cone of the muon. In fact, above about 1 TeV, these stochastic

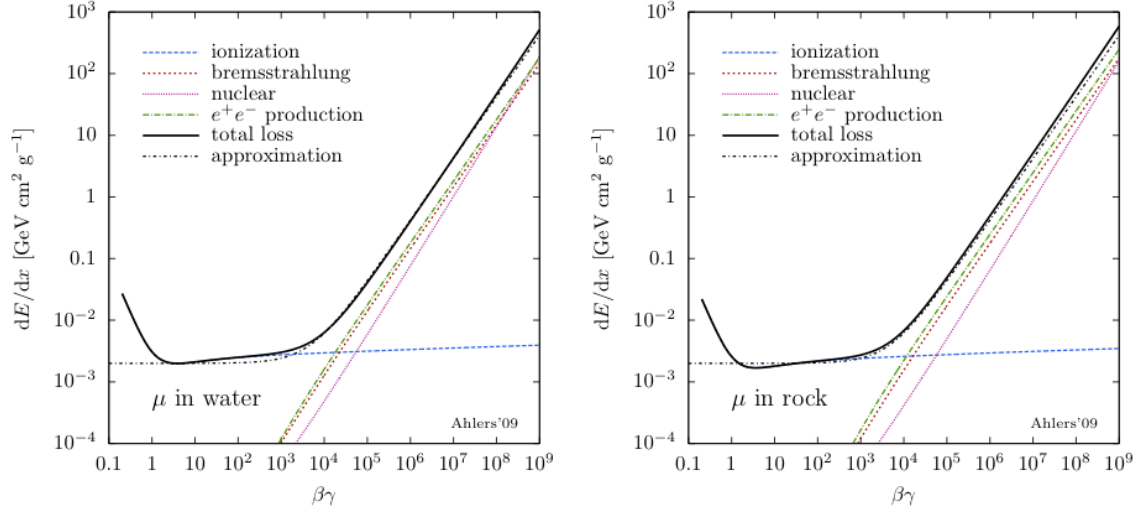


Figure 5.4: Energy loss mechanisms for muons in water (left) and rock (right). From IceCube Yellow Book.

processes dominate the light production. Fig. 5.4 shows the various mechanisms for energy loss as the muon propagates. An estimation of dE/dX is used as a proxy for energy in the analyses presented in Chapter 7.

The detection rate for high energy ν_μ is aided by the fact that the CC interaction cross section as well as the range of the resultant muon are proportional to the neutrino energy. The muon can have a track length from several tens of meters up to several kilometers, and can reach the detector even if produced outside of the detector, increasing the detectors effective volume. The track length, before the muon energy falls below a detection threshold E_μ^{th} , is given by

$$x_\mu = \frac{1}{\beta} \ln \left[\frac{\alpha + \beta E_\mu}{\alpha + \beta E_\mu^{th}} \right]. \quad (5.7)$$

Here, E_μ is the initial muon energy (= a fraction, $1 - y$, of the incident neutrino energy), and E_μ^{th} is the detection threshold, roughly 100 GeV. The mean scattering

angle between the incident neutrino and the resultant muon is a function of energy, and is on the order of a degree:

$$\langle\theta\rangle\approx\frac{0.7^\circ}{(E_\nu/\text{TeV})^{0.7}}.\tag{5.8}$$

5.4 Event Signatures

For all three flavors, NC interactions lead to hadronic showers at the point of interaction. CC interactions have some unique signatures, allowing flavor-tagging of the incident neutrino. A CC interaction between a ν_e and a target nucleus results in an electron and fragmentation of the target nucleus. Rather than propagate a significant distance like a muon, the electron initiates an electromagnetic (EM) shower and the target nucleus initiates a hadronic shower. Since this shower and the accompanying Cherenkov light does not have a nice conical shape, but rather a spherical shape elongated in the electron's direction, directional reconstruction is not as good as it is for ν_μ events. However, essentially all of the shower energy is deposited in the detector. Thus energy resolution is better for showers than for tracks. For showers, energy resolution will be roughly 10 to 20% and angular resolution may be on the order of 10° for the highest energy events.

Muons created in CC interactions in the ice surrounding or within the detector carry about 75% of the ν_μ 's energy [108]. Angular resolution is aided by the conical Cherenkov cone emitted along the muon's path and is typically between 0.5° and 1° , depending on the angle of incidence and the muon energy. Energy resolution for muons is hindered by the fact that their path length typically exceeds the size of

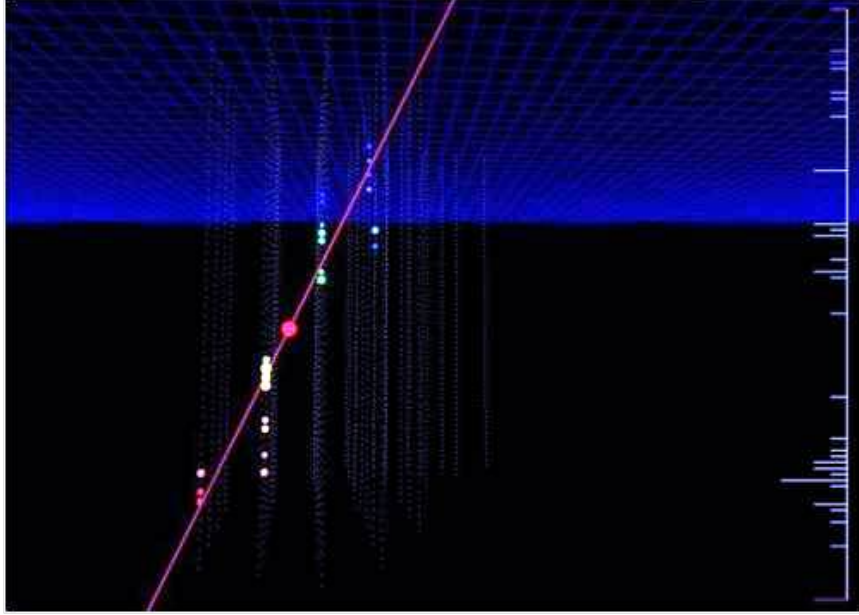


Figure 5.5: Up-going muon neutrino event in IceCube.

the detector as well as the fact that the angle and intensity of the Cherenkov cone is essentially constant due to the relativistic nature of the muons. Showers from bremsstrahlung radiation make it possible to estimate muon energy to an accuracy of about 0.3 on a logarithmic scale. Figs. 5.5 and 5.6 show the signatures of an up-going ν_μ event and a horizontal ν_μ event, from 40-string IceCube in IceCube's event viewer. The colors of the marked DOMs represent the hit times, and the size of the marks represent the amount of charge, or light, at each DOM.

Tau neutrinos are unique in that they can essentially regenerate, even after CC interactions, as they propagate through the Earth. That is because the tau lepton produced in the neutrino's CC interaction will decay before ranging out. A new ν_τ is produced in this decay, although at a reduced energy. The signature of ν_τ events in or near the detector can be unique, as well. A hadronic cascade is created

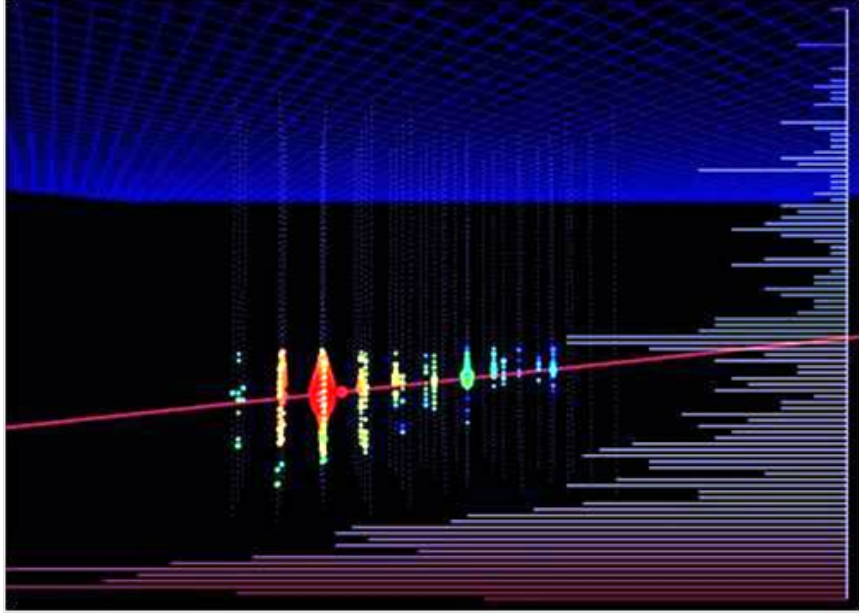


Figure 5.6: Horizontal muon neutrino event in IceCube.

at the initial interaction point, followed by a faint track due to the tau. A second cascade is created when the tau decays. The details of the appearance of a ν_τ event depend upon whether one, or both, of these cascades are contained in the detector. The separation between the two cascades depends on the energy of the tau.

5.5 Triggering

DOM MB electronics apply a threshold trigger, set to 0.25 photoelectrons (PE), to the PMT analog signals before waveforms are captured and time-stamped. Local coincidence checks between adjacent DOMs on a string reduce false triggers due to dark noise before waveforms are digitized and sent to the surface. To implement local coincidence checks, a DOM sends a pulse to its nearest or next-to-nearest

neighbors whenever its discriminator fires. A DOM will only send its data to the surface if it receives a local coincidence pulse from a nearby DOM within 1000 ns of triggering. DOMs fire at a rate of about 540 Hz due to dark noise. These local coincidence checks reduce the false trigger rate to less than a Hz.

The simple majority trigger (SMT) for in-ice events for 2008 was set at eight hit channels within a 5000 ns trigger window. Readouts included a 5000 ns pre-window and a 5000 ns post-window. Local coincidence requirements were set to next-to-nearest-neighbor. Triggered events with overlapping time windows were combined into a single event. Time window cleaning, discussed shortly, was used to extract the highest energy event, as well as reject hits that were likely noise.

5.6 Filtering

The data rate from the DAQ far exceeds the amount of data that can be transmitted via satellite. Hence, a significant reduction in the trigger-level data must be accomplished. Various software filters are running at the South Pole. These filters either reject events that are obviously uninteresting background events, or extract particular classes of events.

The Processing and Filtering (PnF) system accomplishes the software-level filtering. Events from the DAQ enter a buffer for subsequent processing by the PnF system. A cluster of processors in the counting house perform a variety of fast reconstructions on the data, and apply the output to multiple filters. Events are sent to a buffer if they pass one or more of the filters. The transfer of data from this buffer

over the communications satellite is handled by the South Pole Archival and Data Exchange (SPADE) system. During the data run with the 40-string configuration, the daily satellite bandwidth was about 35 GB/day. All triggered events are written to tape, regardless of whether they pass a filter. However, the goal is to ensure that events of interest pass the initial filtering not only so that they are readily available in the north, but to minimize the need for time-consuming data recovery from tapes.

5.7 Event Reconstruction

Simple and fast reconstructions are performed in real-time at the South Pole. These initial reconstructions are less accurate than ones performed later, at institutions in the north. However, they can be accomplished within the time and CPU constraints at the South Pole while keeping up with the trigger rate. Higher level reconstructions performed at institutions in the north include improved likelihood fits for better angular resolution and background rejection, as well as reconstruction of additional parameters, such as energy. Fits to additional track hypotheses are also performed. Some higher level reconstructions incorporate the detailed ice model.

5.7.1 Waveform Calibration

Waveform calibration is also known as charge calibration. It comprises a number of steps taken to translate digital waveforms to the number of photoelectrons (NPE), and their time-sequence, recorded by the DOMs. The NPE is the num-

ber of photons that hit the PMT times the probability that a photon generates a pulse above threshold (which includes the PMT quantum efficiency and other effects). Numerically, $NPE = Q/q_0$, where q_0 is the charge associated with a single photoelectron (SPE) detected by a DOM (a DOM-specific value) and Q is the total charge in the pulse. DOM specific calibration constants are applied. Waveforms from the three ATWD channels are combined to create one calibrated waveform. For each bin, the value from the lowest-gain, unsaturated readout is used.

Droop correction refers to an off-line correction of waveform shapes which have been distorted by transformer droop. A transformer between the PMT and the high voltage board in the DOM acts as a high-pass filter on the PMT output, causing the tails of the waveforms to undershoot. This effect is worse at lower temperatures. The droop correction inverts the effect, and eliminates the undershoot in the waveform tails. The characteristic parameters for the correction are two time constants, which are temperature dependent and vary from DOM to DOM.

5.7.2 DOM Launch Cleaning

Readouts from a predefined list of known problem DOMs are removed. For the 40-string configuration in the 2008/09 data season, this list contained about 29 DOMs with a variety of problems such as power shorts, abnormal current draw, or bad communications.

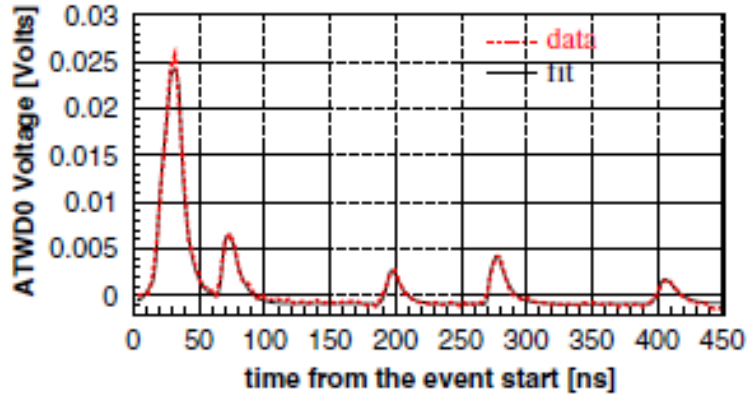


Figure 5.7: Reconstruction of photoelectron pulses from the waveform data acquired by DOMs. From [97].

5.7.3 Feature Extraction

Feature extraction is the process of extracting photon arrival times from the calibrated waveforms. A waveform is modeled as the sum of n pulses, with each pulse characterized by amplitude, arrival time, and width. An iterative algorithm is used to determine the number and characteristics of the individual pulses that best reproduces the observed waveform. Fig. 5.7 shows a typical calibrated waveform and the resultant fit.

5.7.4 Time Window Cleaning

Due to the length of the event readout window, and the possibility that more than one triggered event can be combined into one readout, the time difference between the first and last hits recorded in a single event can be several tens of μs . However, a single muon traveling at roughly the speed of light will spend at

most three μs in the detector and photons associated with a single track should be detected within about a four μs window. To get rid of these unwanted hits, a sliding six μs window is adjusted to include the period with the most hits in the event. Hits outside this window are discarded.

5.7.5 LineFit

The LineFit reconstruction is a fast, first-guess algorithm. It is based on the assumption that the Cherenkov light from a muon propagates as a plane wave. This assumption is incorrect but it leads to a fitting algorithm that is extremely fast, and often does a decent job of estimating the muon track direction. LineFit and likelihood-based reconstructions seeded with the LineFit track are used as part of the software filtering at the South Pole. Additionally, the velocity calculated by LineFit can be used to estimate how well the fit represents a muon track.

The algorithm for this fit is based on a χ^2 fit using the equation

$$\chi^2 = \sum_{i=1}^{N_{hit}} (\mathbf{r}_i - \mathbf{r} - \mathbf{v} \cdot t_i)^2, \quad (5.9)$$

where \mathbf{r} and \mathbf{v} are the reconstructed position and velocity, and the subscript i refers to the individual hits. The best-fit solution can be found analytically, and is given by

$$\mathbf{r} = \langle \mathbf{r}_i \rangle - \mathbf{r} \cdot \langle t_i \rangle, \quad (5.10)$$

and

$$\mathbf{v} = \frac{\langle \mathbf{r} \cdot t_i \rangle - \langle \mathbf{r}_i \rangle \cdot \langle t_i \rangle}{\langle t_i^2 \rangle \langle t_i \rangle^2}. \quad (5.11)$$

The $\langle \rangle$ notation implies an average over all hits.

5.7.6 Maximum Likelihood Reconstructions

Photon arrival times are used in reconstruction algorithms that attempt to account for the geometric dependence of arrival times, as well as the stochastic variability in arrival times due to scattering. The likelihood function to be minimized is the function [109]

$$L = \prod_j p(a, t_{hit,j}), \quad (5.12)$$

where a is the set of parameters characterizing the hypothesized track, i.e. vertex and direction, and possibly energy. $p(a, t_{hit})$ is the probability distribution function (PDF) for hit times. The product is over all photon hits in the event. In practice, the maximum of the likelihood function is found by minimizing the negative of the log of the likelihood, so the product becomes a sum. To simplify implementation, a transformation is made and time residual, t_{res} , is used in place of t_{hit} , where

$$t_{res} \equiv t_{hit} - t_{geo}. \quad (5.13)$$

The geometric photon arrival time, t_{geo} , is the expected hit time if scattering and absorption are ignored. This is given by [110]

$$t_{geo} = t_0 + \frac{1}{c} \left[\hat{v} \cdot \vec{r} + d \frac{n_{gr} n_{ph} - 1}{\sqrt{n_{ph}^2 - 1}} \right], \quad (5.14)$$

where n_{gr} and n_{ph} are the group and phase refractive indices for light in ice.

The geometry of the track and hit channels is shown in Fig. 5.8. The muon transits with velocity \vec{v} , which exceeds the speed of light in the ice. Cherenkov radiation is generated by the muon as well as by particles created in stochastic interactions along the muon's track. The muon is at position B when Cherenkov

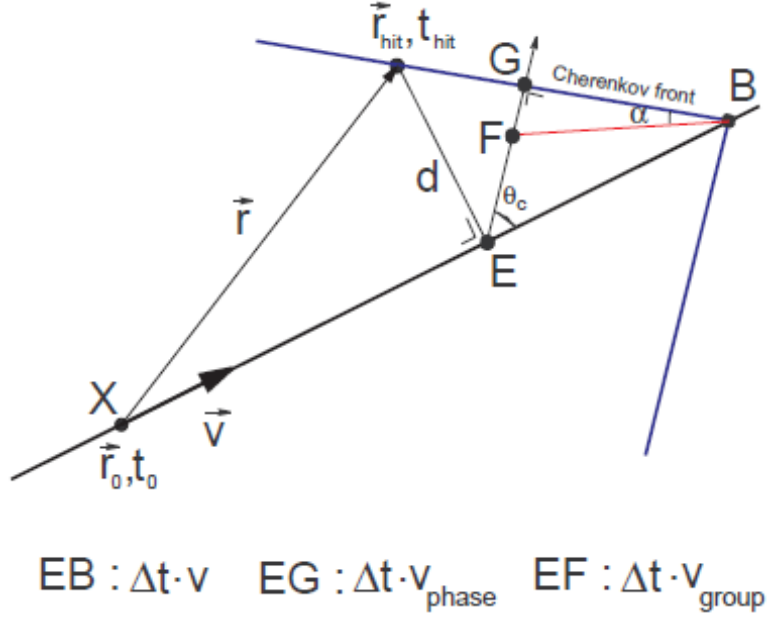


Figure 5.8: Geometry of the signal detection process. From [110]

photons emitted while it was at X reach the hit channel at (\vec{r}_{hit}, t_{hit}) . Point E is the point of closest approach between the muon track and the hit channel.

To perform the minimization process, a PDF is required. We start with the Pandel PDF [111]

$$p(\rho, \xi, t_{res}) = \frac{\rho^\xi t_{res}^{\xi-1}}{\Gamma(\xi)} e^{-\rho t_{res}}, \quad (5.15)$$

where ξ is the distance traveled by a photon from emission to detection in units of the mean scattering length, ρ is an inverse time scale, and Γ is the standard gamma function. The Pandel PDF is an analytic estimate for the distribution of photon arrival times for a monochromatic, isotropic source, in a medium dominated by scattering. However, the function is not defined for negative time residuals, which can occur due to the finite time resolution of the detector. The Pandel PDF is

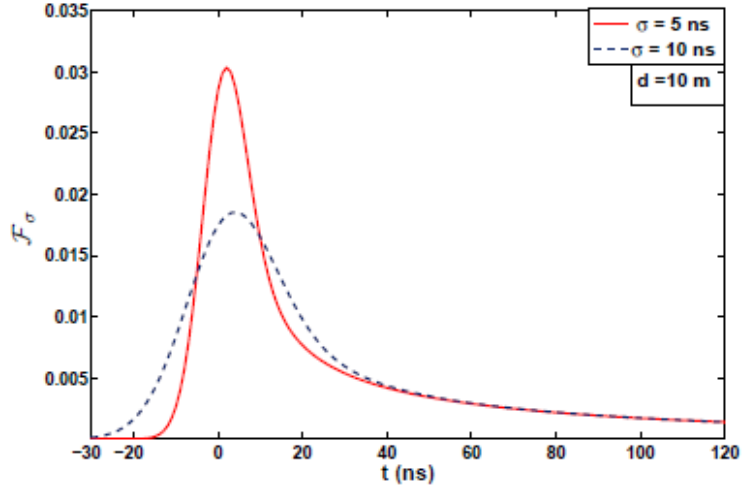


Figure 5.9: CPandel PDF for two values of the time resolution parameter (5 and 10 ns). The distance of closest approach d is 10 m. From [110].

therefore convolved with a Gaussian PDF. The resultant PDF is then [110]

$$F_{\sigma}(\rho, \xi, t_{res}) = \int_0^{\infty} \frac{dx}{\sqrt{2\pi\sigma^2}} p(\rho, \sigma, x) e^{-(t_{res}-x)^2/2\sigma^2}, \quad (5.16)$$

which is implemented numerically. Fig. 5.9 shows sample profiles for the PDF function.

Maximum likelihood reconstructions for IceCube are accomplished with a software project called Gulliver. In addition to specifying the minimization algorithm and the PDF, the user has to specify what seed track(s) to use. The minimization algorithm used is the Minuit algorithm as implemented by the TMinuit package in ROOT [112].

5.7.7 Single Photoelectron Fit

SPE, or single photoelectron fits, are likelihood fits that use only the arrival time of the first photoelectron in all hit channels, throwing out the information associated with later hits. The Pandel function is used to estimate the likelihood of the photon arrival time. Typically, LineFit is used as the seed for this fit. The fit can be automatically repeated many times, with a new pseudo-random seed used each time, to cover the direction space. This can help ensure that a local minimum was not found on the first trial and can sometimes improve the fit by ensuring a global minimum is found. Typically, 16 or 32 iterations are used.

In addition to track location and direction, likelihood fits, such as SPE, and MPE to be discussed next, return several parameters that can be used to estimate fit quality. These parameters include the log-likelihood (logl) and the reduced log-likelihood, $\text{rlogl} = \text{logl}/n_{dof}$, where n_{dof} is the number of degrees of freedom in the minimization, i.e. the number of hit channels minus the number of parameters to be fit. rlogl is then independent of the number of hit channels. A similar scaled parameter, related to rlogl , has been found to be useful at discriminating between signal and background. This parameter is called plogl and is equal to $\text{logl}/(\text{number of hit channels} - 2.5)$.

5.7.8 Multiple Photoelectron Fit

The Multiple Photoelectron fit (MPE) is very similar to the SPE fit in principle and in implementation. However, as the name implies, it uses multiple photon hit

times from each hit DOM in the likelihood minimization. Since more information is used, the accuracy of the fit can be improved as compared to the SPE fit. To ensure the MPE fit does not get trapped in a local minimum, it is usually seeded with a track thought to be reasonably near the correct direction, such as the output of the SPE fit.

Key to the likelihood minimization process for the MPE is modifying the PDF to account for multiple photon arrival times. The PDF described previously accounts for the expected distribution of arrival times for the first photon to hit a DOM. However, here we need to account for the likelihood of photon arrival times regardless of whether they are the first photon. The PDF for the n^{th} photon, in terms of the PDF for the first photon, is

$$\text{MPE}_n(t_{res}) = n \cdot \text{SPE}_n(t_{res}) \cdot \left[t_{res} \cdot \int \text{SPE}_n(t) dt \right]^n. \quad (5.17)$$

5.7.9 PhotoRec

PhotoRec is a reconstruction algorithm that accounts for spatially variable ice properties [113]. It does this by incorporating light propagation tables created by Photonics (see Chapter 6). The output of PhotoRec used in this analysis is the estimation of dE/dX . dE/dX is the average energy loss per unit propagation length, for the muon, that would produce the detected amount of light. It is related to the number of photons emitted along the track and hence to the number of photons detected. To get the proportionality right, additional factors have to be taken into account, including the distance between the track and the hit channels, and the

amount of scattering and absorption between generation and detection points. The reconstruction algorithm assumes that stochastic energy losses are uniform along the muon track.

5.7.10 Paraboloid

The Paraboloid fit [114] analyzes the value of the likelihood function around a seed, typically an SPE fit track. After transforming the coordinate space to one centered on the direction of the seed track, it attempts to fit a paraboloid to the likelihood space around that track. The important result of the Paraboloid fit is the paraboloid sigma. Calculated from the errors on the major and minor axes of the constant likelihood paraboloid,

$$\sigma = \sqrt{\frac{1}{2} (\sigma_1^2 + \sigma_2^2)} \quad (5.18)$$

provides an estimate of the pointing error of the track.

5.7.11 Bayesian

In the Bayesian reconstruction, the regular likelihood function is multiplied by a bias function which depends only on the event hypothesis and not on the actual event data. The bias is used as a way to include prior knowledge of the characteristics of the event sample, i.e. that mis-reconstructed down-going tracks dominate the event sample. In this approach, an up-going track should only be selected if its regular likelihood is so good that it is found by the minimizer even with a bias term added to the down-going hypothesis. This fit uses the same seeds as the 32

iteration SPE fit, derived from the SOBOL pseudo-random sequence. The Bayesian likelihood ratio is the useful result from this reconstruction, $\log l_{bayes} - \log l_{SPE32}$.

5.7.12 Umbrella

The umbrella reconstruction simply constrains the minimizer to the hemisphere opposite some seed track. The likelihood ratio between this reconstruction and the 32 iteration SPE reconstruction can then be calculated as $\log l_{umbr} - \log l_{SPE32}$. Better tracks will have a much higher SPE likelihood than a fit constrained to the opposite hemisphere, and so they will have negative umbrella likelihood ratios.

5.7.13 SplitTrack

The Split Track reconstructions begin by splitting the hit channels into two different groups based on hit time, and also into two different groups based on geometry. LineFit and SPE fit reconstructions are performed on each of these subsets of hits. These fits provide discrimination for poorly reconstructed tracks, as well as for tracks that reconstruct as up-going due to the superposition of hits from two separate down-going muons. Zenith angles, or the likelihood parameters for the split tracks, can be used for event discrimination.

5.7.14 Additional Cut Parameters

Photons originating from farther away from a DOM are more likely to be scattered, and the distribution of arrival time probabilities is more spread out. A larger number of direct hits, that is hits that propagate directly to the DOM with little or no scattering, has been found to be correlated with better track reconstruction. Hence, the number of direct hits (NDir) is a useful cut parameter. The number of direct hits is defined as the number of DOMs that have a hit with a residual time difference of

$$-15\text{ns} > t_{res} > 75\text{ns}. \quad (5.19)$$

The likelihood that a track is properly reconstructed is also correlated with the number of hit strings, and the more strings the better. Hence, the NString variable is useful for discriminating between signal and mis-reconstructed background.

Smoothness is a measure of how well the observed hit pattern is explained by the hypothesis of constant light emission along the reconstructed muon track. Mathematically, smoothness is defined as the value of S_j with the maximum absolute value, where S_j is defined as

$$S_j = \frac{j-1}{N-1} - \frac{l_j}{l_N}. \quad (5.20)$$

l_j is the distance along the track between the points of closest approach of the track to the first and the j^{th} hit module. N is the total number of hits. Tracks with hits clustered at the beginning or end of the track have S approaching $+1$ or -1 , respectively. High quality tracks, with S close to zero, have hits equally spaced along the track. This parameter can be calculated using all hits, or just direct hits.

The length of the event, L , is determined by projecting each hit OM onto the reconstructed track and taking the distance between the two outermost points at the ends of the track. Larger values of L indicate a more reliable reconstruction of track direction. This parameter can also be calculated using all hits or direct hits only.

Chapter 6

Event Selection

Since any remaining background contamination is difficult to model with simulation, we required an essentially pure neutrino sample for this analysis. Event selection and background rejection cuts were developed using simulation. Background rejection was done in several stages, beginning with triggering and software-based filtering at the South Pole. Then, before more CPU intensive reconstructions were performed, the background of uninteresting or unusable events was reduced by selection cuts based on zenith angle and track quality parameters, a step referred to below as data processing cuts. Finally, analysis level cuts were applied. Analysis level cuts included a set of “pre-selection” cuts that improved the training and performance of the boosted decision trees (BDT) used for the final cut level, and the BDT cut itself.

6.1 Backgrounds

We are interested in up-going atmospheric ν_μ events. The background for this analysis is down-going atmospheric muons that are mis-reconstructed as up-going. Locating IceCube at a depth greater than a km helps attenuate the flux of atmospheric muons. However, a significant number of high energy atmospheric muons still reach the detector. In fact, the ratio of down-going atmospheric muons

to muons produced in or near the detector by neutrino interactions is roughly one million to one [115]. Even after an initial event selection cut based on zenith angle, the event sample is dominated, by several orders of magnitude, by mis-reconstructed atmospheric muons. These mis-reconstructed tracks are either individual muon tracks or coincident atmospheric muons that mimic a single up-going event.

At higher energies, a diffuse flux of astrophysical neutrinos should stand out (recall Fig. 2.11 from Chapter 2). However, for the live time, detector size, and effective energy coverage of this analysis, a diffuse flux of astrophysical neutrinos is considered negligible and is not accounted for.

6.2 Simulation

Detailed simulation of atmospheric muons and neutrinos was needed for determining event selection and background rejection cuts, training and testing the BDTs, and optimizing the analysis methodologies. Simulated data sets were also used for producing prediction histograms for the likelihood analyses, the response matrix and the expected flux histogram for the unfolding analysis, and for determining sensitivity thresholds during the discrete Fourier transform (DFT) analysis. Several specialized data sets were used for systematics studies and toy MC studies.

6.2.1 Atmospheric Muons

Muons from air showers are simulated with CORSIKA [116]. The primary cosmic ray spectrum known as the Hoerandel poli-gonato model [58] was used. In

this model, the spectrum of each component is a combination of two power laws, with the turnover between the two power laws being a function of the nuclear charge Z of the primary. CORSIKA propagates cosmic ray primaries to their point of interaction with a nucleus in the atmosphere. The hadronic interaction is modeled using an interaction model such as DPMJET [117] or SIBYLL [118]. The secondary particles are then tracked as they propagate and interact or decay.

Single muon events, as well as events with two or three coincident muons, are included in the simulation. Events with individual muons in the detector are combined, and re-weighted appropriately, to account for the probability of coincident events occurring. Muon propagation and energy loss within and around the detector is simulated with Muon Monte Carlo (MMC) [119].

6.2.2 Atmospheric Neutrinos

Neutrino propagation (from point of origin in the atmosphere to interaction in or near the detector) is simulated with ANIS [120]. ANIS generates neutrinos of any flavor according to a specified flux, propagates them through the Earth, and in a final step simulates neutrino interactions within a specified volume. For computing efficiency, all simulated neutrinos are forced to interact, but their probability of interacting is accounted for in the event weight assigned by ANIS.

ANIS accounts for CC and NC neutrino-nucleon interactions, as well as neutrino regeneration following NC interactions. Also accounted for is the offset between neutrino propagation direction and the direction of the outgoing muon following a

CC interaction. Cross sections based on the CTEQ5 parton distributions were used [104]. The Preliminary Reference Earth Model [121] was used to model the density profile in the Earth.

6.2.3 Light Propagation

Light propagation is simulated using Photonics [122]. Photonics tables are created once for a given model of the absorption and scattering properties in the ice. A set of tables is created where the number and arrival times of photons are parameterized by the position of the DOM in the ice, relative position of the muon track, the energy deposition, and the direction of the muon. The output is saved in a table format, with parameters binned in location, time, photon emission angle, and incidence angle. A large number of tables, for various source directions and locations, are generated. During simulation production, or Photonics-based reconstructions, tables are queried with the location and orientation of the source, and the location of the detectors. Interpolation is applied between tables. Photon arrival times are randomly drawn from the time distribution tabulated for the given coordinates.

6.2.4 Detector Hardware

Simulation of detector hardware components is provided by various software modules that account for PMT response (i.e. the creation of a waveform from photoelectron(s)), DOM MB response to the simulated waveform, triggering, local coincidence, etc. Simulated data is then processed through all the same stages of

filtering, reconstruction algorithms, and analysis level cuts as real data.

6.2.5 Neutrino Flux Weighting

Neutrino events in simulation are weighted according to their contribution to the atmospheric neutrino flux. For this analysis, the flux predictions of Honda *et al.* [17], were used for conventional atmospheric muon neutrinos, and Enberg *et al.* [66], were used for prompt atmospheric muon neutrinos. The predictions for muon neutrinos from pions and kaons were extended to higher energies by fitting a physics-motivated analytical equation based on energy and zenith angle (see chapter 7 of Gaisser [57]) in an overlapping region with the detailed calculations of Honda *et al.* [17]. Symmetry is assumed between the flux of up-going and down-going atmospheric neutrinos [17]:

$$\varphi_\nu(-\cos\theta) = \varphi_\nu(\cos\theta). \tag{6.1}$$

For prompt atmospheric neutrinos, the flux of ν and $\bar{\nu}$ are assumed to be equal.

Solar modulation as well as affects of the Earth's magnetic field are ignored, reasonable assumptions at the > 100 GeV energy range of this analysis. Mass-induced oscillations are included in the simulation chain. Event weights for toy MC studies are adjusted for the particular oscillation or decoherence model being tested. Event weights are also adjusted when prediction histograms are built by the likelihood minimizer, according to the nuisance parameters discussed in the next chapter.

Normally, we could ignore ν_τ -induced muons for an atmospheric neutrino anal-

ysis. A small number of atmospheric ν_τ and $\bar{\nu}_\tau$ are produced by the decays of D_s mesons. This is more than an order of magnitude below the flux of prompt ν_μ and $\bar{\nu}_\mu$. Additionally, the probability for ν_τ production from ν'_μ s via mass-induced oscillations is suppressed in the energy range of this analysis. However, if some of the atmospheric ν_μ and $\bar{\nu}_\mu$ are oscillating or decohering to ν_τ and $\bar{\nu}_\tau$ according to the new physics models being tested, then this flux of ν_τ and $\bar{\nu}_\tau$ can not be neglected. These ν_τ could interact near or within the detector, producing a tau lepton, which could then decay into (among other things) a muon (branching ratio about 17%).

Detection of these muons would then dampen the signal we are looking for, i.e. a disappearance of muon neutrinos. The magnitude of this effect is small (on the order of 2 to 3% for the VLI model [76]), due to the steep power law spectrum and the fact that the muon ends up with only a fraction of the tau's energy. Nonetheless, these events are accounted for in the simulation chain for this analysis. Simulation of the propagation and interaction of tau neutrinos is used, but the events are weighted as if they were produced by atmospheric muon neutrinos that oscillated to tau neutrinos according to the particular model being evaluated.

6.3 Muon Filter

Although a variety of filters were deployed at the pole for the 2008-2009 physics run, only events passing the muon filter were used in this analysis. The muon filter is the primary filter for rejecting down-going, atmospheric muons, and retaining generic muon-like events from near or below the horizon. It plays a direct role

in many analyses, including atmospheric neutrino studies, diffuse flux studies, and point source searches. Additionally, the output of this filter is crucial to understanding the irreducible background for most other analyses.

The basic filter consists of two branches of cuts and a minimum NChannel (number of DOMs detecting photons and contributing to the event) threshold of 10. The two branches compliment each other, and use Zenith/NChannel pairs that are specified in a steering file. Branch 2 extends the reach of the muon filter further above the horizon and includes a mandatory cut on the average NHits/NChannel (number of pulses per hit channel) in an event. Two likelihood (LLH) reconstructions are performed to provide input to the filter. One is seeded with the result of a LineFit reconstruction, the other is seeded with the reciprocal of the LineFit track. This approach reduces the number of mis-reconstructed events that might otherwise pass the filter because a local minimum was found in one LLH fit, or because an up-going track was faked. The two branches differ in that both LLH reconstructions have to agree for an event to be accepted by branch 1, whereas an event is accepted by branch 2 if either LLH reconstruction passes the zenith cut.

The acceptance criteria for the muon filter, for the 40-string configuration, was that the event passes branch 1: (LLH-1 Zenith AND LLH-2 Zenith ≥ 80 AND NChannel ≥ 10) or (LLH-1 Zenith AND LLH-2 Zenith ≥ 70 AND NChannel ≥ 16); or, the event passes branch 2: NHits/NChannel ≥ 5 AND ((LLH-1 Zenith or LLH-2 Zenith ≥ 50) AND NChannel ≥ 20) OR ((LLH-1 Zenith or LLH-2 Zenith ≥ 70) AND NChannel ≥ 10).

6.4 Data Processing Cuts

Prior to performing the higher level, more CPU intensive reconstructions required by this and similar analyses, data reduction cuts were performed to remove events that were clearly not going to be useful. These cuts were a zenith angle cut of 80° , an rlogl cut of 12, and a plogl cut of 8, all based on the output of a 32-iteration SPE fit. These cuts significantly reduced the CPU loading early on in the data processing chain, with little loss of events that would have passed final analysis level cuts.

6.5 Pre-selection Cuts

Two BDTs were used in this analysis. One has better efficiency at lower energies, the other has better efficiency at middle and higher energies. Events are accepted if they pass either BDT. The BDTs are essentially trying to distinguish between poorly reconstructed background events, and signal events that include some that are well reconstructed and some that are poorly reconstructed. By applying pre-selection cuts prior to BDT training, the signal event sample was cleaned up somewhat, and the overall performance of each BDT was improved. For the low energy BDT (BDT 1), the pre-selection cut was LineFit velocity ≥ 0.2 . For the other BDT (BDT 2), the pre-selection cut was that all Split Track fits returned a zenith angle $\geq 80^\circ$. The same data processing cuts and pre-selection cuts were applied to the actual data, as were used in creating the simulated background and signal event samples used for BDT training.

6.6 Boosted Decision Trees

Final event selection to achieve the desired level of purity was done using Boosted Decision Trees (BDT). Decision trees are an excellent “out of the box” classifier [123]. They are similar to rectangular cuts. However, whereas a cut-based analysis is able to select only one hypercube out of a multidimensional parameter space, the decision tree is able to split the parameter space into a large number of hypercubes, each of which is identified as either signal-like or background-like. The theoretically best performance of a BDT, on a given problem, is generally inferior to other techniques, such as neural networks. However, in academic examples with complex correlations, or real life examples, BDTs often out-perform the other techniques. This is because either there are not enough training events available that would be needed by the other classifiers, or the optimal configuration (i.e. how many hidden layers, which variables, etc.) for a neural network is not known and is difficult to determine [123].

A decision tree is a binary, tree structured classifier. The nodes form what looks like an inverted tree. A yes/no (signal like / background like) decision is made at each node. The training algorithm chooses as the cut variable and cut value at each node, the one that gives the best discrimination at that node. Events are split into the nodes that make up the next layer of the tree, and the process repeated until an end condition is reached. Typically, when a minimum number of events in a node is reached, that node is no longer split. Variables may be used multiple times in a tree, with different cut values each time. Other variables specified by the

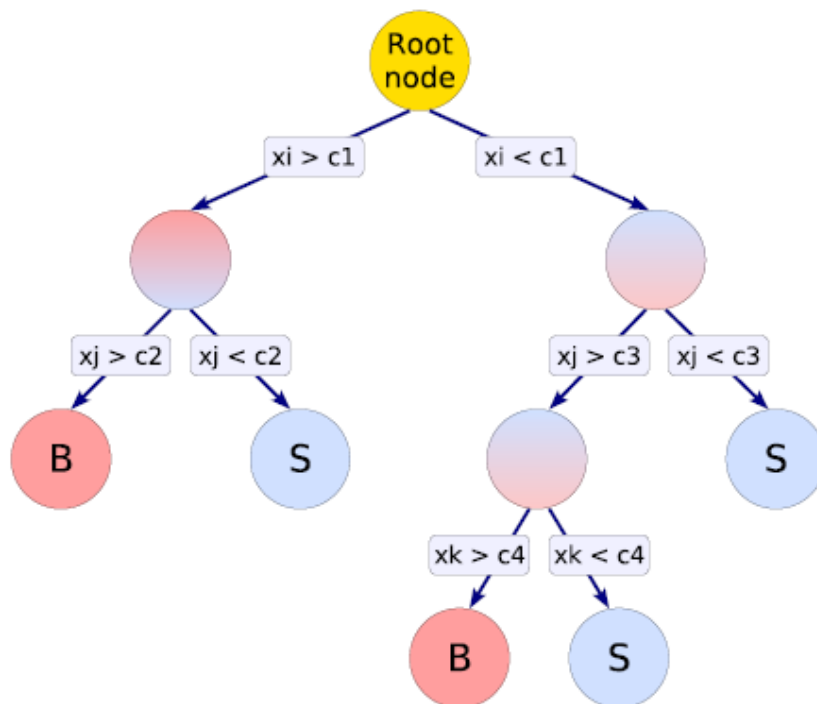


Figure 6.1: Schematic view of a decision tree, from [123]. Starting from the root node, a sequence of binary splits are applied to the data. Each split uses the variable that at this node gives the best separation between signal and background. The same variable may thus be used at several nodes, while others might not be used at all. The leaf nodes at the bottom end of the tree are classified signal or background, depending on the majority of events that end up in the respective nodes.

user may be used seldom, or not at all. The final nodes are classified as signal or background, depending on the classification of the majority of training events that end up in each node. Fig. 6.1 shows a schematic representation of a tree.

The decision tree training algorithm will ignore non-discriminating variables and is thus insensitive to the inclusion of poorly discriminating input variables. A decision tree does not find functional dependencies between the cut variables, such as a properly set-up neural network would. The user can specify functional

dependencies among the variables, however, when they are defined for a decision tree.

A shortcoming of decision trees is their instability with respect to statistical fluctuations in the training sample from which the tree structure is derived. For example, if two input variables exhibit similar separation power, a fluctuation in the training sample may cause the tree growing algorithm to decide to split on one variable, while the other variable may have been selected had that fluctuation not been present. In such a case the whole tree structure is altered below this node, possibly resulting in a substantially different classifier response. The boosting of a decision tree solves this problem. The concept of a decision tree is extended from one tree to possibly hundreds of trees which form a forest. The additional trees are derived from the same training ensemble by re-weighting events. After one tree is created, events that were mis-classified in that tree have their weights increased, and the next tree is created. This next tree will choose different variables and cut values at each node, due to the altered weights. The final classifier uses a weighted average of the individual decisions of all the trees.

The final classification score for an event is based on a weighted majority vote of the individual trees:

$$Y_{BDT}(\tilde{x}) = \sum_{i \in forest} \alpha_i \cdot h_i(\tilde{x}). \quad (6.2)$$

Y_{BDT} is the BDT score for the event, normalized to fall between 0 and 1. \tilde{x} is the array of values for each of the variables, for the given event. α_i is the fraction of events correctly classified in tree i . h_i is the decision tree result for the event in

tree i , 1 if the event lands in a signal node, 0 if it lands in a background node. The user chooses the value of the BDT score to use as a cut value, based on the desired trade-offs between signal efficiency and background contamination.

6.6.1 Training, Testing, and Choice of BDT Cut Values.

Muon neutrino simulation, with an E^{-1} spectrum, was used for signal events in the BDT training. Although the true signal spectrum is much steeper than this, testing indicated this spectrum for training produced a BDT that performed better for higher energy events, with no compromise in performance for lower energy events. If the signal events are weighted realistically, the training algorithm gives little weight to mis-classification of high energy events. Cosmic ray muon simulation from CORSIKA was used for background events. Following training, the BDTs were tested using independent signal and background event samples. It was found that a minimum of 30,000 signal and 30,000 background events were needed for training, to obtain satisfactory and consistent performance. Table 6.1 lists the reconstruction variables used in the BDTs.

As mentioned earlier, different pre-selection cuts were applied prior to the training, and application, of each BDT. Also, the NString variable was only used by BDT 1. One additional difference between the two BDTs is the source of the Split Track fits used as BDT variables. For BDT 1, which is optimized for lower energies, the LineFit reconstruction of each of the four split tracks (two split geometrically and two split in time) were used. For BDT 2, if SPE fits were successful for the split

Table 6.1: Reconstruction variables used in the BDTs. See Chapter 5 for definitions.

BDT Variables
Paraboloid Error on the MPE fit RLogl and PLogl from MPE fit NDirC and LDirC SmoothAll NDirC/NPulses $Logl_{Bayes} - Logl_{SPE32}$ NString $ \theta_Z^{MPE} - \theta_Z^{LineFit} $ $Logl_{Umbrella} - Logl_{SPE32}$ θ_z , Split-Track LineFit results θ_z , Split-Track SPE16 results

tracks, then those results were used, otherwise the LineFit results were used. SPE fit results were not available for events in which there were too few hit channels to perform a likelihood fit in one or more of the splits.

Neutrino simulation weighted to an atmospheric spectrum, as well as single, double, and triple-coincident muon events, weighted to the cosmic ray muon spectrum, were used for testing the BDTs. Since an event sample with negligible background was desired, the BDT cut values were chosen at the point where the background events were eliminated. Coincidentally, the desired cut values turned out to be the same, 0.73, for each BDT.

The effective live time of the available CORSIKA was limited and not representative of the year of live time for the data. In fact, additional testing with more background simulation indicated that some events were showing up, occasionally, that did pass the selection cuts. We did not have enough simulation for a reliable estimate of background contamination. Hence, comparisons between data

and neutrino simulation were made after unblinding to verify that the BDTs were performing as expected. The amount of background contamination is estimated to be about 1%.

Fig. 6.2 shows the efficiency of the BDTs relative to the output of the data processing cut level. The plots show, as a function of energy and cosine of the zenith angle, the fraction of events passing all cuts up to and including the data processing cuts that also pass the cuts specific to this analysis. The cuts specific to this analysis include the pre-selection cuts and the BDT cuts. Green is the efficiency of BDT 1 alone; Red is the efficiency of BDT 2 alone; Blue is their combined efficiency. Fig. 6.3 shows the output of the Boosted Decision Trees, for six months of data and for neutrino simulation weighted to the same live time.

6.7 Final Event Selection

To give a sense for the impact of the BDT cut, Fig. 6.4 shows the event rate for atmospheric muon neutrinos, in simulation, at various stages in the event selection process. Fig. 6.5 shows the same progression of event rate for data. The rate after applying a BDT cut value of 0.7 is shown for comparison only; the BDT cut was applied just once, at a value of 0.73.

The choice of the final BDT score to cut on was based on simulation, but then verified by comparing the data passing rate to the predicted rate from neutrino simulation. Fig. 6.6 shows the ratio, data to simulation, for the number of events passing the BDT cut, as a function of BDT cut value. On the left is BDT 1, on the

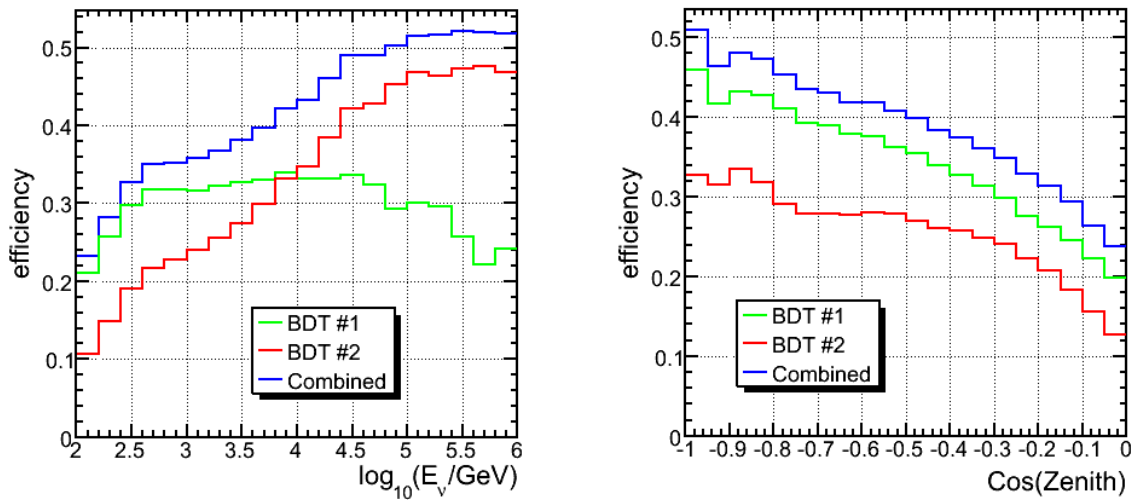


Figure 6.2: Efficiency of the BDTs, relative to the output of data processing cuts. The plots show, as a function of energy and cosine of the zenith angle, the fraction of events passing all cuts up to and including the data processing cuts, that also pass the cuts specific to this analysis. Green is the efficiency of BDT 1 alone; Red is the efficiency of BDT 2 alone; Blue is their combined efficiency.

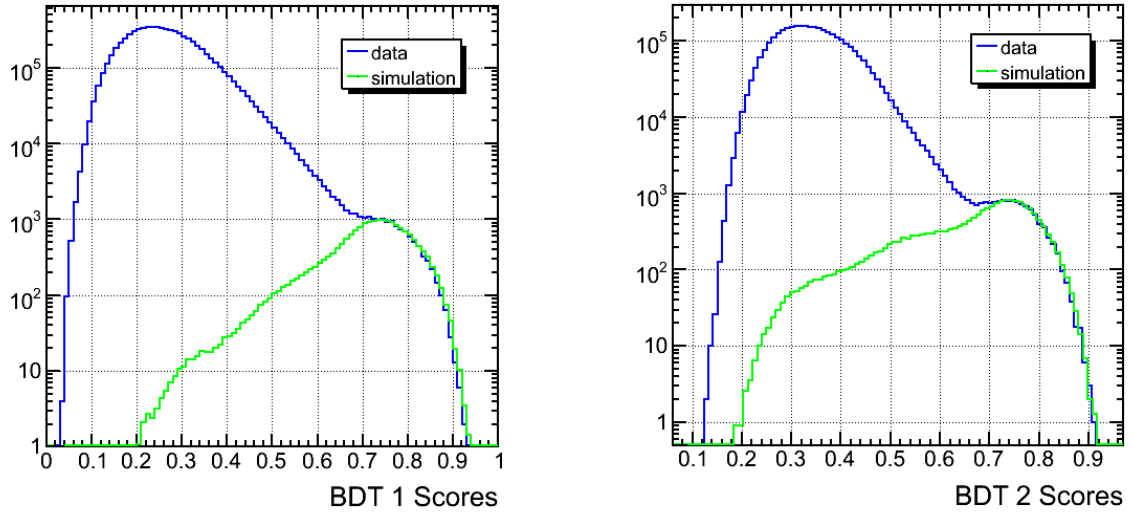


Figure 6.3: Output of the BDTs, for data (blue) and for neutrino simulation (green). Above the chosen cut values of 0.73 for each BDT, data and neutrino simulation agree, indicating that the unwanted background of cosmic ray muons has been rejected.

right is BDT 2. Note the leveling out near the chosen cut values of 0.73, indicating background rejection has likely been optimized. Behavior of this ratio fluctuates beyond the chosen cut value, probably due to statistical fluctuations and the low number of events in data, and disagreements between data and simulation in the tails of the distributions of variables used in the BDTs. Another feature to note is that the ratio data/simulation, at the chosen cut value of 0.73, is not the same for both BDTs. For BDT 1, the ratio is about 0.97, and for BDT 2 the ratio is about 1.01. There is a slightly larger fraction of events that pass both BDTs in data, than in simulation.

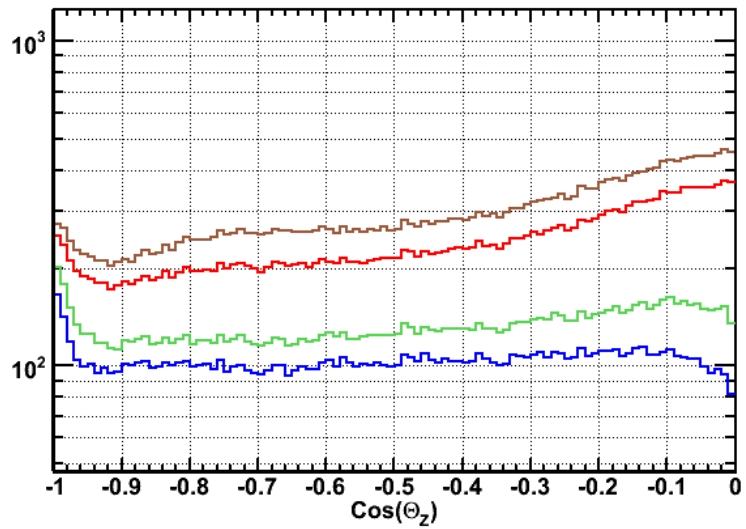


Figure 6.4: Progression of event rate for various cut levels for simulated atmospheric neutrinos, scaled to the same live time as the data shown in Fig. 6.5. Brown after data processing cuts; Red after pre-selection cuts; Green after BDT cut with a cut value of 0.7; Blue after BDT cut with a cut value of 0.73.

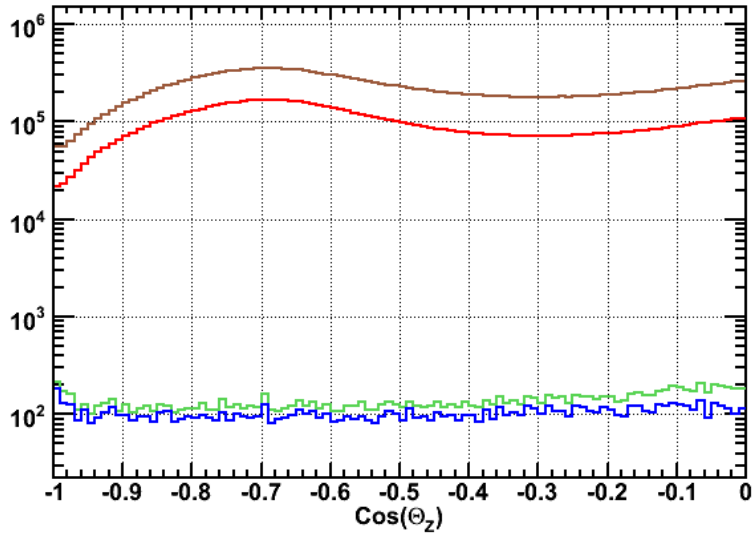


Figure 6.5: Progression of event rate for various cut levels for data. Brown after data processing cuts; Red after pre-selection cuts; Green after BDT cut with a cut value of 0.7; Blue after BDT cut with a cut value of 0.73.

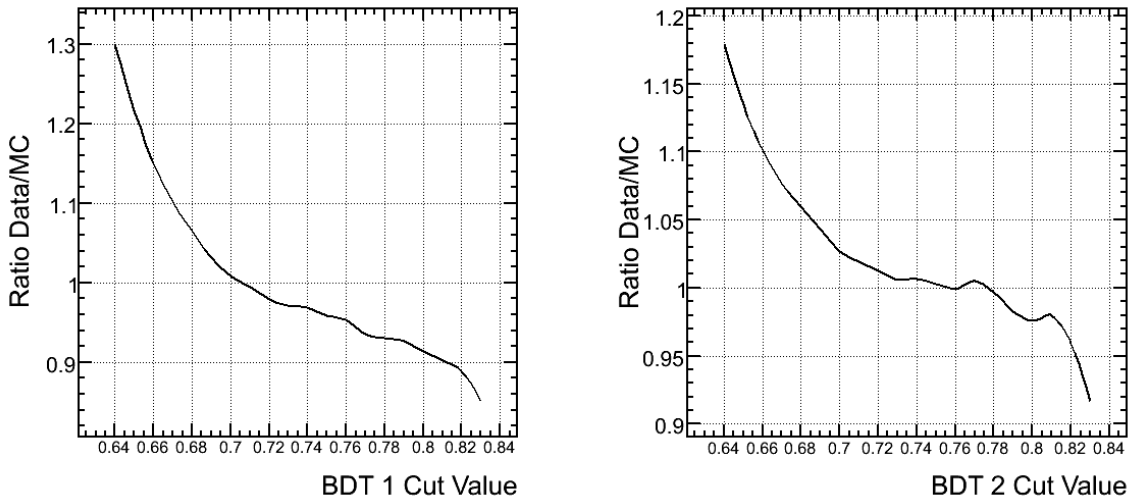


Figure 6.6: Ratio, data to simulation, as a function of BDT cut value. On the left is BDT 1, on the right is BDT 2. Derived from six months of data.

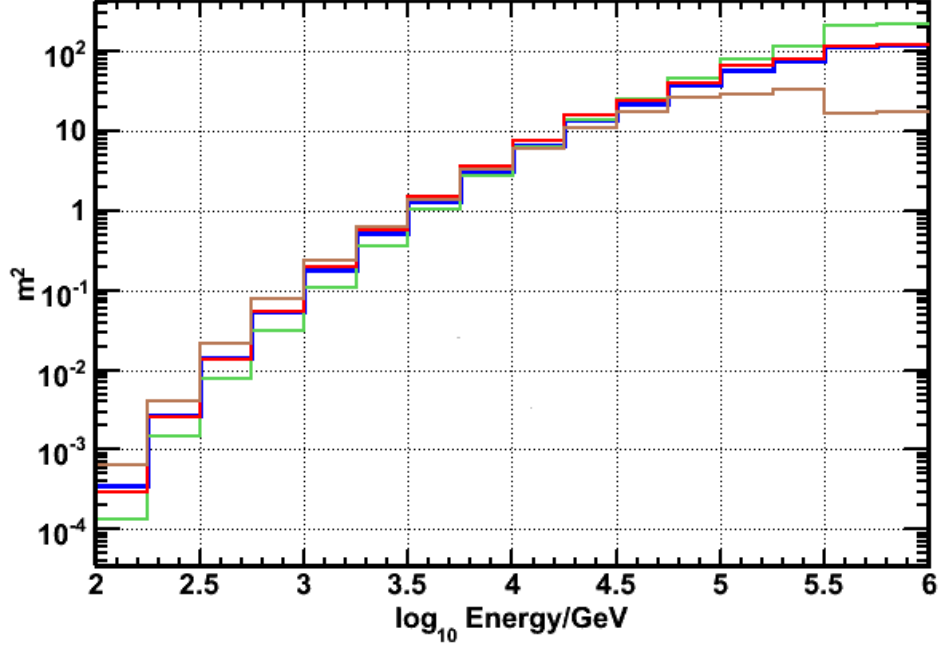


Figure 6.7: Effective area for up-going muon neutrinos as a function of neutrino energy. Blue $-1 < \cos(\theta_z) < 0$; Green $-.33 < \cos(\theta_z) < 0$; Red $-.66 < \cos(\theta_z) < -.33$; Brown $-1 < \cos(\theta_z) < -.66$.

6.7.1 Effective Area

$\Phi(E, \theta)$ is the true flux of atmospheric neutrinos. It is a function of zenith angle and neutrino energy and has units of $\text{GeV}^{-1} \text{s}^{-1} \text{sr}^{-1} \text{cm}^{-2}$. The effective area, A_{eff} , is then the function that satisfies this equation for the predicted number of detected events:

$$N_{events} = \int dt \int d\Omega \int dE \cdot \Phi(E, \theta) \cdot A_{eff}(E, \theta). \quad (6.3)$$

Fig. 6.7 shows the effective area after final selection cuts, as a function of energy and for different zenith ranges.

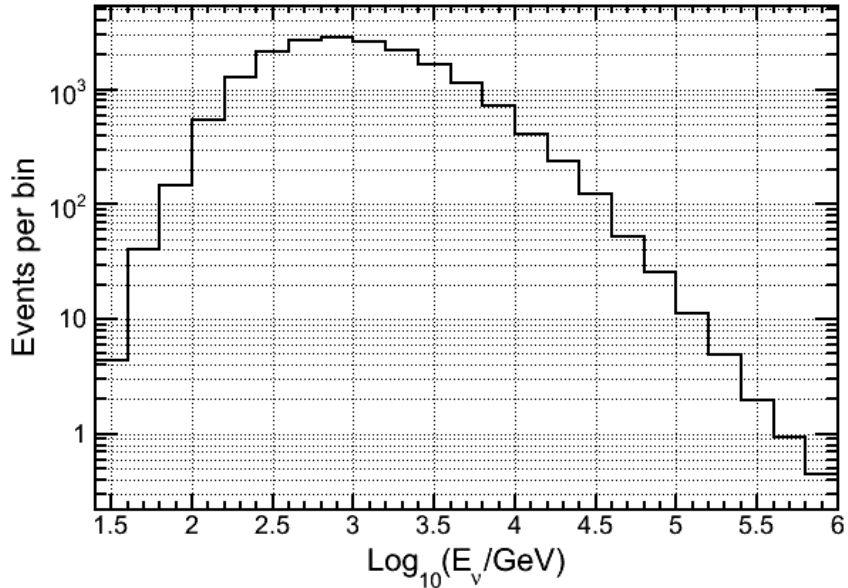


Figure 6.8: Energy reach of final neutrino sample, as predicted by simulation.

6.7.2 Final Event Sample

After eliminating data runs with some strings not operating, testing in progress, or various faults, there was a total of 359 days of live time of good data runs from 17 April 2008 to 20 May 2009. After final event selection cuts, the number of up-going neutrino events from 40-string IceCube is 20,496, with zenith angles between 90 and 180 degrees. Based on simulation, 90% of the neutrinos in this sample are in the energy range 180 GeV to 10.1 TeV. The energy reach of the final event sample, as indicated by simulation, is shown in Fig. 6.8.

Fig. 6.9 shows the number of events from the final data set in each of the dE/dX versus $\cos\theta_Z$ bins for the likelihood analysis. Fig. 6.10 shows the dE/dX and $\cos\theta_Z$ distributions for data and simulation. The apparent excess in the data near the

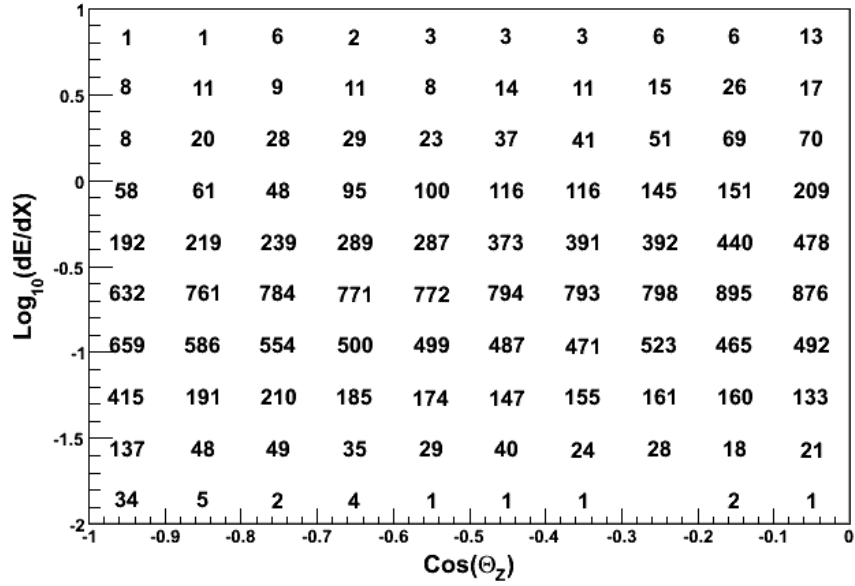


Figure 6.9: Number of events in the data, for each bin of the dE/dX versus $\cos\theta_Z$ histogram.

horizon will be discussed in Chapter 8. Fig. 6.11 shows the dE/dX and $\cos\theta_Z$ distributions after an additional zenith angle cut (at 97°) and re-binning in $\cos\theta_Z$.

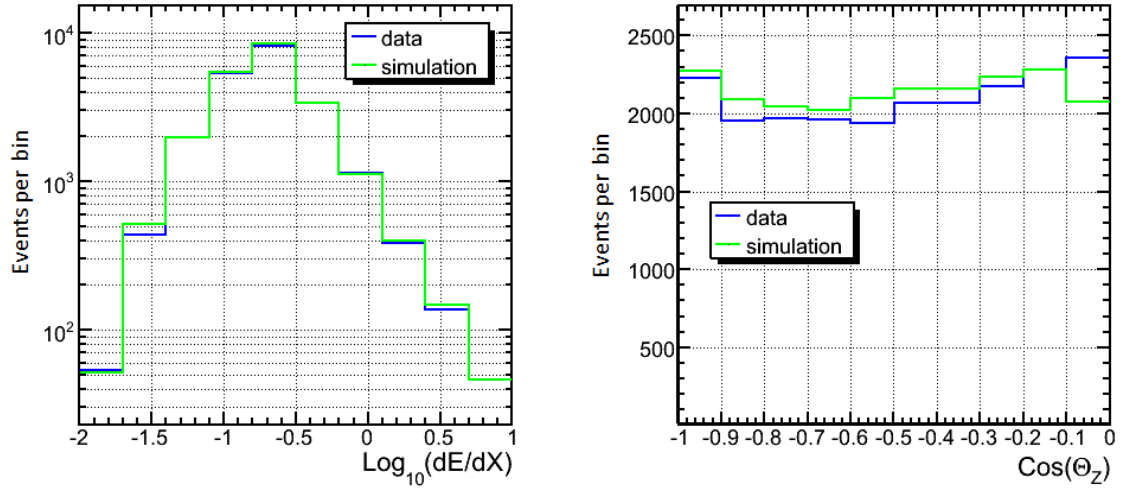


Figure 6.10: Distributions of observables for the likelihood analysis. dE/dX and $\cos \theta_Z$ for data (blue) and simulation (green).

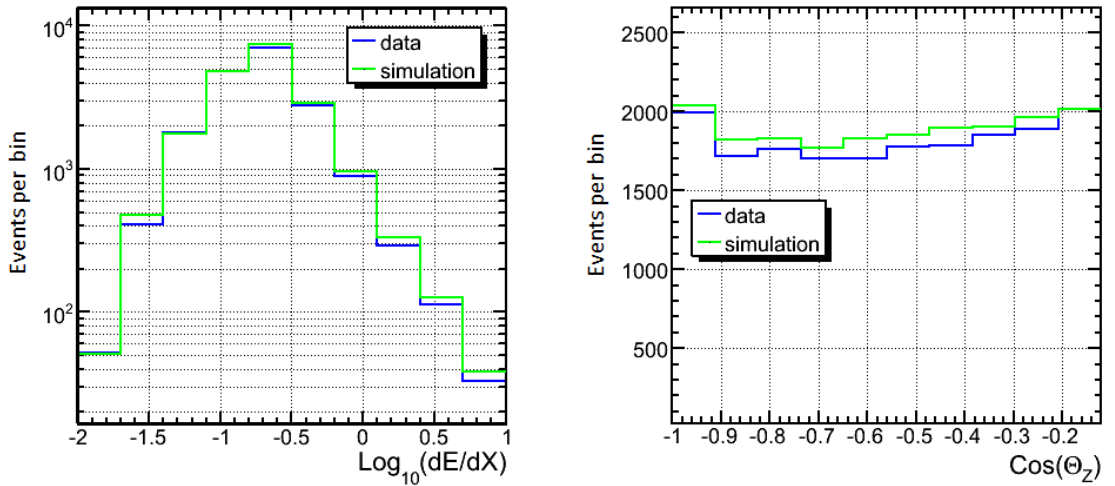


Figure 6.11: Distributions of observables for the likelihood analysis after re-binning. dE/dX and $\cos \theta_Z$ distributions for data (blue) and simulation (green), after additional zenith angle cut at 97° and re-binning in $\cos \theta_Z$.

Chapter 7

Analysis Methodology

7.1 Likelihood Ratio Test

In general, a likelihood analysis is useful because it can take advantage of the shape of a distribution, not just numbers of events or ratios of numbers of events. Additionally, the method can simultaneously constrain the parameters of interest (physics parameters for the model being tested) and parameters that are not necessarily of interest but that can impact the results (nuisance parameters). The method thus provides a straight-forward accounting of systematic uncertainties. Since we are interested in deviations in the energy and zenith angle dependence of the atmospheric neutrino flux, a two-dimensional likelihood analysis with events binned in dE/dX (a proxy for energy) and cosine of the zenith angle has been developed.

In the process of determining maximum likelihood fits or prediction histograms, simulated muon neutrino events are re-weighted according to

$$w = \varepsilon \left(\frac{E}{E_{ref}} \right)^{\Delta\gamma} \left[1 + 2\alpha \left(\cos \theta_Z + 1/2 \right) \right] \times \left\{ \left[1 + 2\alpha_c \left(\cos \theta_Z + 1/2 \right) \right] w_c + A_p \left(\frac{E}{E_{ref,p}} \right)^{\Delta\gamma_p} w_p \right\} \times P_{\nu_\mu \rightarrow \nu_\mu}(\theta_r), \quad (7.1)$$

where w_c and w_p are the weights necessary to reproduce the conventional and prompt neutrino (plus antineutrino) fluxes, based on the models of [17] and [66] respectively.

These weights include a factor called OneWeight that is computed during generation of the simulation and accounts for the survival probability through the Earth as well as the probability of interacting in or near the detector. E is the neutrino energy, θ_Z is the zenith angle, and $P_{\nu_\mu \rightarrow \nu_\tau}$ is the oscillation or decoherence survival probability. θ_r represents the physics parameters associated with the model being tested. The remaining variables are nuisance parameters, collectively denoted as θ_s . These nuisance parameters account for the more significant theoretical and experimental uncertainties in flux normalization, spectral index, and zenith angle tilt.

The form of Eqn. 7.1 is due to the fact that some uncertainties affect the conventional and the prompt atmospheric neutrino flux, whereas other sources affect just one or the other. ε accounts for theoretical and experimental uncertainties in the overall flux normalization, such as ice model uncertainties, OM sensitivity uncertainty, interaction rate uncertainties, reconstruction errors, uncertainties in the cosmic ray flux, etc. $\Delta\gamma$ accounts for the uncertainty in the primary cosmic ray spectral slope as well as the impact of OM and ice model uncertainties on the observed spectral index. α accounts for the impact of OM and ice model uncertainties on the zenith angle tilt of the observed flux. α_c accounts for theoretical uncertainty in the zenith angle tilt of the conventional atmospheric neutrino flux, primarily due to uncertainty in the pion to kaon ratio. A_p and $\Delta\gamma_p$ account for theoretical uncertainty in the magnitude and spectral index of the prompt atmospheric neutrino flux, primarily due to uncertainties in charm production cross sections and fragmentation functions. The particular forms of the spectral index correction and zenith angle tilt

factors were chosen to minimize the impact on overall normalization as the nuisance parameters are varied, to simplify the minimization process. E_{ref} and $E_{ref,p}$ are mean energies for the affected distributions.

Events are binned in $\log_{10}(dE/dX)$ versus $\cos \theta_Z$. dE/dX , with units of GeV/m, is a reconstructed variable that is proportional to the average energy loss per unit propagation length of a muon that would produce the detected amount of light, and serves as an estimator for the muon energy, which is correlated with the neutrino energy. The energy resolution is about 0.3 on a log scale, reducing sensitivity to VLI effects by a factor of two as compared to perfect energy resolution. The data is binned with $\log_{10}(dE/dX)$ and $\cos \theta_Z$ ranging from -2.0 to 1.0 and -1.0 to 0 , respectively, in 10×10 histograms. After an additional cut at 97° zenith angle is added (see Chapter 8), binning in $\cos \theta_Z$ is from -1.0 to -0.12 .

The likelihood function is the Poisson likelihood function

$$L(\{n_{ij}\}|\{\mu_{ij}(\theta_r, \theta_s)\}) = \prod_{i,j} \frac{\mu_{ij}^{n_{ij}}}{n_{ij}!} e^{-\mu_{ij}}, \quad (7.2)$$

where θ_r represents the physics parameters for the model being tested, and θ_s represents the nuisance parameters. n is the data, μ the prediction, and the product is over all bins, i, j , in the two-dimensional dE/dX versus $\cos \theta_Z$ histograms.

MINUIT2 [124] is used to perform the minimizations. The negative of the log of the likelihood function is minimized, rather than maximizing the likelihood:

$$-\ln L = \sum_{i,j} (\mu_{i,j} - n_{i,j} \ln \mu_{i,j} + \ln n_{i,j}!). \quad (7.3)$$

The test statistic is

$$R = -2 \ln \frac{L_0}{\hat{L}}. \quad (7.4)$$

L_0 is the maximum likelihood with the physics parameters fixed and the nuisance parameters allowed to vary. \hat{L} is the maximum likelihood with all parameters allowed to vary. The ratio is essentially a measure of the extent by which particular values of the physics parameters improve or degrade the fit. The factor of 2 scales the likelihood ratio so that it behaves roughly as a χ^2 distribution, with the number of degrees of freedom equal to the dimensionality of θ_r . However, it is not precisely a χ^2 distribution, so the Feldman-Cousins ordering method [125, 126, 127] is required.

The test statistic can be written as

$$R = 2 \left(\ln \hat{L}(\tilde{\theta}_r, \tilde{\theta}_s) - \ln L_0(\theta_r, \tilde{\theta}_s) \right). \quad (7.5)$$

In terms of the observables, this becomes:

$$R = 2 \sum_{i,j} \left(-\mu_{i,j}(\tilde{\theta}_r, \tilde{\theta}_s) + n_{i,j} \ln \mu_{i,j}(\tilde{\theta}_r, \tilde{\theta}_s) + \mu_{i,j}(\theta_r, \tilde{\theta}_s) - n_{i,j} \ln \mu_{i,j}(\theta_r, \tilde{\theta}_s) \right). \quad (7.6)$$

$\mu_{i,j}(\tilde{\theta}_r, \tilde{\theta}_s)$ is the best-fit prediction histogram built by the minimizer when physics and nuisance parameters are allowed to vary. $\mu_{i,j}(\theta_r, \tilde{\theta}_s)$ is the best-fit prediction histogram built by the minimizer when physics parameters are held fixed and nuisance parameters are allowed to vary. $n_{i,j}$ is either the true data, or a toy MC experiment.

Fig. 7.1 and Fig. 7.2 show the R-values for the $n = 1$ VLI model and a toy MC experiment, with systematic uncertainties ignored and included, respectively. The likelihood ratios are roughly distributed as a χ^2 function, and so the thumb rules associated with the level of acceptance for a χ^2 distribution with two degrees of freedom can be used to estimate the acceptance regions from these plots. For example, a value of 4.6 corresponds to a 90% CL, 6.0 a 95% CL, and 9.2 a 99%

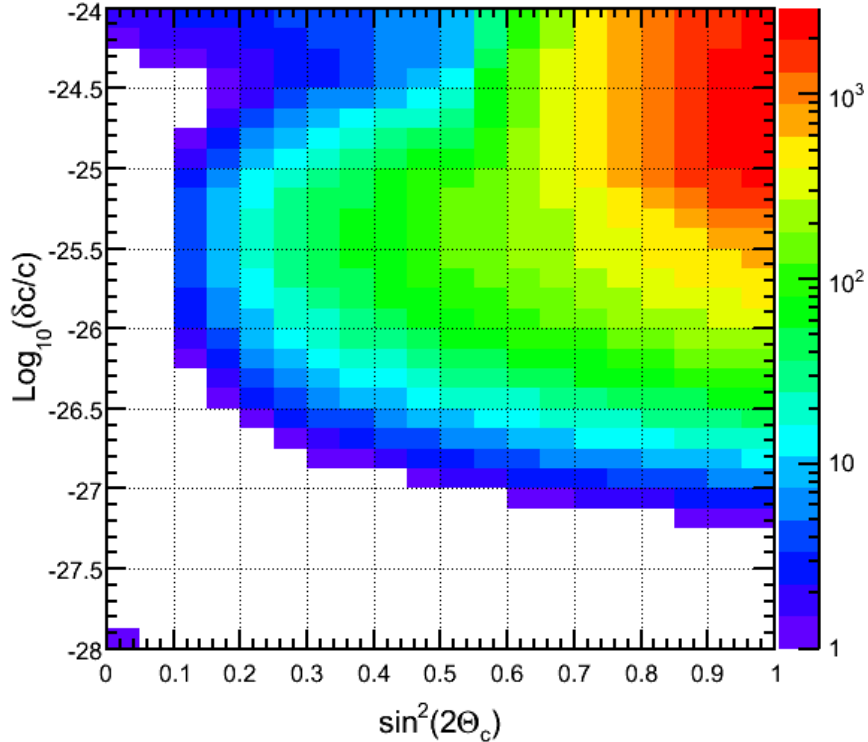


Figure 7.1: R-values, under the $n = 1$ VLI model, for a toy MC experiment and no systematic uncertainties (nuisance parameters ignored by the minimizer).

CL. This approximation is not exact, and in particular, it breaks down in regions of the phase space that are relatively insensitive to changes in one of the physics parameters. Fig. 7.3 and Fig. 7.4 show the R-values for the $n = 2$ decoherence model and a toy MC experiment, with systematic uncertainties ignored and included, respectively.

To determine the confidence intervals, a large number of toy MC experiments (up to 1000) are performed at each point in a scan of the physics parameter space. For each toy MC experiment, a histogram is drawn from the parent distribution, $\mu_{i,j}(\theta_r, \bar{\theta}_s)$, where θ_r are the physics parameters at that point and $\bar{\theta}_s$ are the nuisance

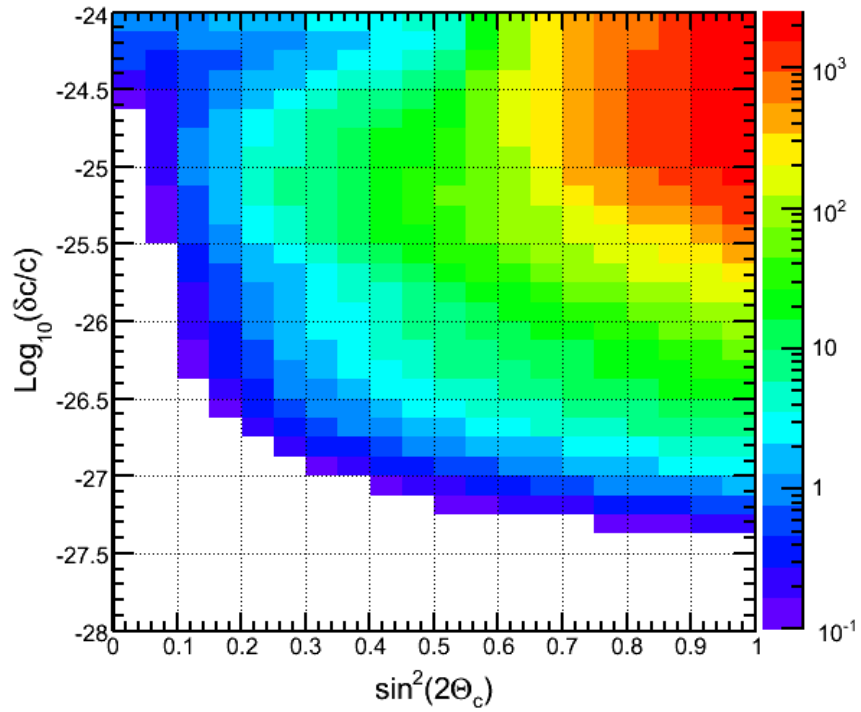


Figure 7.2: R-values, under the $n = 1$ VLI model, for a toy MC experiment including systematic uncertainties.

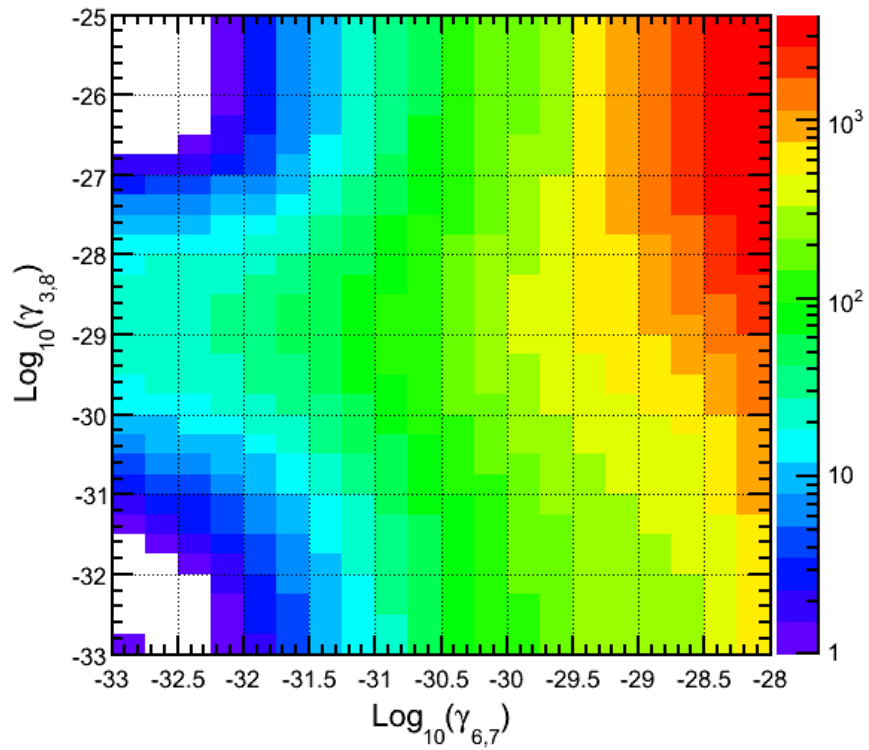


Figure 7.3: R-values, under the $n = 2$ decoherence model, for a toy MC experiment and no systematic uncertainties (nuisance parameters ignored by the minimizer).

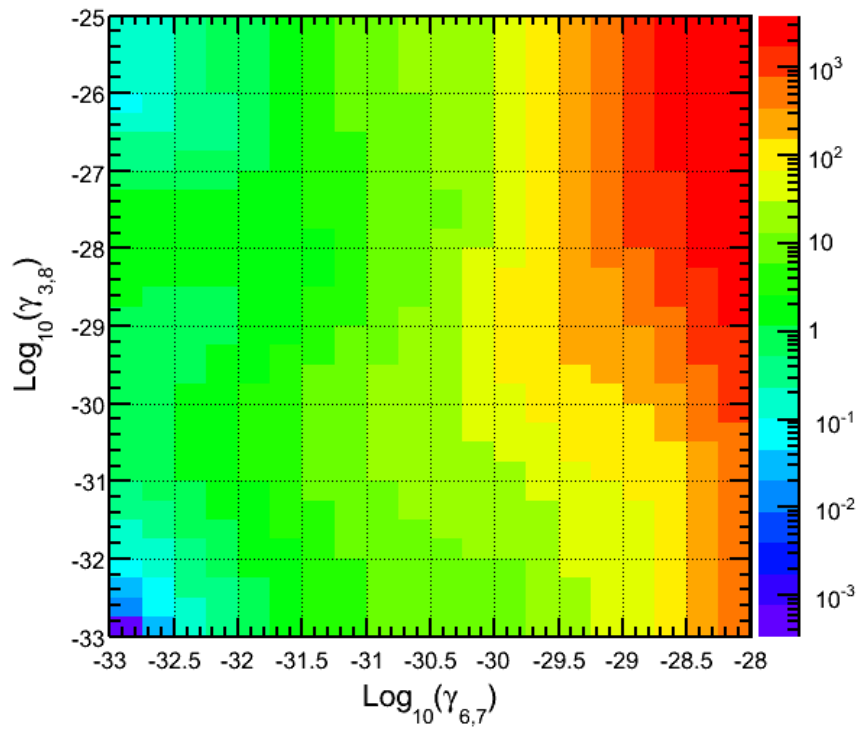


Figure 7.4: R-values, under the $n = 2$ decoherence model, for a toy MC experiment including systematic uncertainties.

parameters chosen by a forward folding fit to best represent the data. A forward folding fit involves determining the values of the nuisance parameters that reproduce the best fit to the data when simulated events are reweighted according to Eqn. 7.1. This is essentially just finding gross corrections to the normalization, spectral index, and zenith angle tilt of the flux models from [17, 66].

Bin counts for each toy MC experiment are varied according to Poisson statistics. The likelihood ratios are computed for each of these toy experiments and this set of likelihood ratios is a measure of how the test statistic responds to statistical uncertainties. A confidence interval of confidence level α is then defined by the value of $R_{crit}(\theta_r)$ such that a fraction α of the toy MC experiments at a point θ_r had a likelihood ratio R less than R_{crit} :

$$\left(\int_0^{R_{crit}} R \right) / \left(\int_0^\infty R \right) = \alpha. \quad (7.7)$$

The acceptance region is that set of points θ_r where $R_{data}(\theta_r) < R_{crit}(\theta_r)$. Fig. 7.5 and Fig. 7.6 show the acceptance regions for a toy experiment, under the $n = 1$ VLI and $n = 2$ decoherence models, after applying the ordering method of Feldman and Cousins.

7.2 Discrete Fourier Transform Analysis

The DFT method was adapted from Ref. [88]. In that case, the MINOS Collaboration was looking for periodic variations in neutrino oscillations in the NuMI beam line, using the MINOS near detector. Although they were evaluating the same coefficients from the SME, the survival probability equation in their analysis was

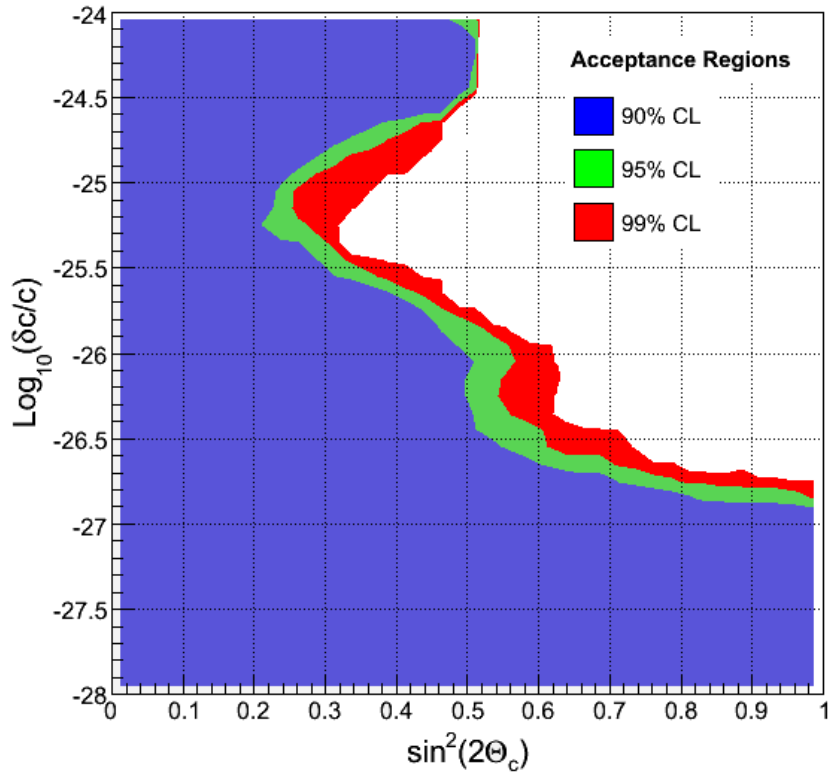


Figure 7.5: Acceptance regions for a toy experiment under the $n = 1$ VLI model. The regions are determined by comparing the likelihood ratios to the critical ratios determined by the Feldman-Cousins method.

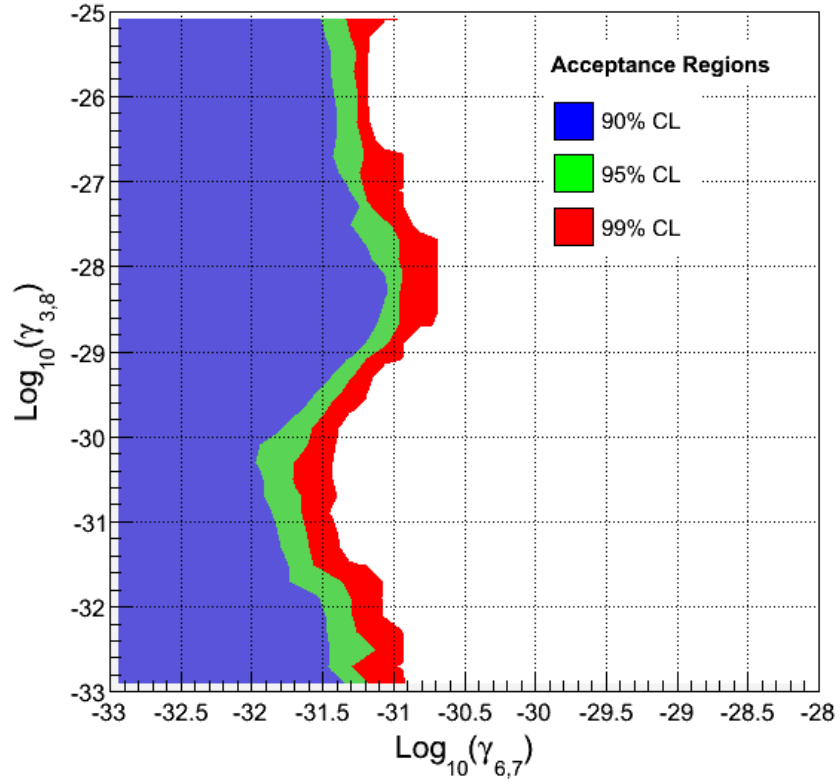


Figure 7.6: Acceptance regions for a toy experiment under the $n = 2$ decoherence model. The regions are determined by comparing the likelihood ratios to the critical ratios determined by the Feldman-Cousins method.

different from the one used here. The approximations used in the two experiments are different, due to the different energy range and length scales. The DFT analysis is much faster and simpler to use than a likelihood analysis. And, since events are binned in RA, it is not sensitive to zenith-dependent systematic uncertainties. It also allows for a model-independent check for a periodic signal.

This analysis is done in two stages. In the first stage, the data is checked for consistency with the hypothesis of no sidereal signal. In the second stage, constraints are placed on the SME coefficients in the vector model. The muon neutrino survival probability varies with RA with a modulation frequency of $4\omega_{\oplus}$, where $\omega_{\oplus} = 2\pi/23\text{h}56\text{ min}$ is the Earth's sidereal frequency. So we want to check the $n = 4$ mode of a DFT of the data, with the data binned in RA. 32 bins are used, from 0 to 360° , to allow measuring the $n = 4$ component. Only events in the declination band 7 to 30° (zenith band 97 to 120°) were used.

First, a large number of toy experiments were performed in which the RAs of all events in the data were randomly redistributed. The power spectral densities (PSDs) in the $n = 1$ to $n = 4$ components of a DFT were computed for each of these noise-only toy experiments. The PSDs of the true data histogram were then computed and compared to the range of PSDs from the toy experiments. This indicated whether the data is consistent with the hypothesis of no sidereal signal.

To set upper limits on the SME coefficients in the vector model, a large number of toy MC experiments were performed. In each trial, events for the toy histograms were drawn from a distribution of simulated events that mimics the energy and zenith distribution of atmospheric neutrinos. RA's were randomly assigned in each

toy experiment. The physics parameters of the vector model were then incrementally increased, and the simulated events re-weighted according to their survival probability under the vector model, until a PSD greater than the 99.87 percentile (equivalent to a 3-sigma threshold) of the PSDs from the noise-only toy experiments was obtained. The values found in each of these trials were averaged to find the sensitivity of this analysis given the data and the absence of a signal. While determining the sensitivity for one coefficient in each of these trials, the other coefficients were held at zero.

As mentioned earlier, if ν_μ are oscillating to ν_τ , then some fraction of these ν_τ would lead to muon tracks in the detector and events in the final sample. This effect was accounted for through toy MC studies using ν_τ simulation. It was found that, for oscillations near the sensitivity threshold, this feedback loop leads to recovering about 6% of the events lost due to oscillations induced by the a coefficients, and about 9% of the events lost due to oscillations induced by the c coefficients. The difference between the two cases is due to the fact that the mean energy of affected events is higher in the case of the c coefficients.

7.3 Unfolding of the Atmospheric Neutrino Spectrum

Unfolding the atmospheric neutrino spectrum involves determining what the ν_μ plus $\bar{\nu}_\mu$ flux is at the point of origin in the atmosphere, based on the observed detector response. For the likelihood and DFT analyses, an unfolding is not necessary. Rather, the effects of the models are propagated through detector specific

simulation, and the results compared to the measured data. However, unfolding the spectrum at the point of origin is desirable because it simplifies comparison to results from other experiments, as well as to various theoretical predictions. Unfolding removes the need for someone trying to use the flux measurement in IceCube to account for IceCube systematics, detector efficiency, and effective area.

In general, the measurement b is a function of the true neutrino flux x , and a response matrix A that accounts for the modification, attenuation, limited detector acceptance, bin-to-bin migration of events, etc., that happens due to propagation through the earth, and interaction in and measurement by the detector:

$$Ax = b. \tag{7.8}$$

Ideally, the matrix A could be inverted and the true distribution directly calculated as $x = A^{-1}b$. However, this is in general not possible. Since an analytical solution for the smearing matrix is not known, it must be determined from simulation. However, only a limited live time of simulated data is available. Additionally, there are statistical fluctuations in the measured data. These fluctuations would lead to unphysical fluctuations in the solution.

The desired distribution x is expressed in quantities that are not directly measured. Rather the number of events in each bin of a dE/dX histogram is used as the observable. There is a finite resolution for this measured variable, with large bin-to-bin migration. Simulation is used to find the response matrix, A , which maps the distribution of events based on the observable to the distribution of true neutrino energies.

The SVD unfolding algorithm [128] was used for the unfolding. This algorithm has been implemented in the RooUnfold package [129] for use in the ROOT framework. The inputs to the unfolding algorithm are: the response matrix from simulation, the predicted histogram for the observed distribution, and a histogram for the true flux. x_{MC} is a 12 bin histogram of the predicted atmospheric neutrino flux, binned in $\log_{10}(E_\nu)$ from 2 to 5.6, where E_ν is the neutrino energy in GeV. b_{MC} is a 12 bin histogram of the expected dE/dX distribution for events passing final cuts, binned in $\log_{10}(dE/dX)$ from -2.1 to 1.5 . A is a 12 x 12 histogram filled with values of $(\log_{10}(dE/dX), (\log_{10}(E_\nu)))$, for all events in b_{MC} .

The unfolding algorithm overcomes the problem of statistical fluctuations in the data through regularization. The shape of the true flux is assumed to be similar to the shape of the simulated flux. Higher frequency terms, in a Fourier-like expansion of the solution, are dominated by statistical fluctuations that get enhanced without regularization. The curvature in the solution, i.e. how sharply it can fluctuate from bin-to-bin, is regulated, preventing statistical fluctuations in the data from being interpreted as structure in the true distribution. The amount of regularization must be specified, and a smooth cutoff is applied to the higher frequency terms. A lower cutoff biases the solution towards simulation, a higher cutoff biases the solution towards the data.

The optimal choice of the regularization parameter depends on the number of bins and the sample size. The proper value to use must be determined on a case-by-case basis. Two methods for determining the optimal choice of the regularization parameter are discussed in Ref. [128]. The first method is to examine a plot of the

variable $\log |d_i|$ versus i , where d is a vector computed by the unfolding algorithm. The components of d are the coefficients of the rescaled measurement histogram, in front of a particular set of basis functions. The d_i fall exponentially, with values for low i being significant. The critical value is the i after which the d_i are not significant. The other method is to use toy MC studies, based on simulation that is systematically and statistically different from the training simulation, to determine what value leads to the best performance. These tests indicated that the input variable $kterm$ should be 3 in this case. $kterm$ is the input to the SVD unfolding algorithm that directs what regularization parameters to use. The scaling factors for the smooth cutoff are computed within the unfolding algorithm, based on the specified value of $kterm$.

Chapter 8

Systematic Uncertainties

8.1 Uncertainties in Atmospheric Neutrino Flux Predictions

Affecting both the conventional and prompt components of the atmospheric neutrino flux is the uncertainty in the normalization of the cosmic ray flux, as well as uncertainty in the spectral index of the cosmic ray flux. From Honda *et al.* [17], the uncertainty in the normalization of the atmospheric neutrino flux at 1 TeV (the mean energy of events in this analysis) is $\pm 25\%$. The bulk of the nucleons in cosmic rays are in protons (79%) and helium nuclei (15%), so we can get a reasonable estimate of the uncertainty of the overall cosmic ray spectral index by considering the uncertainty in these two components. From Gaisser *et al.* [130], the uncertainty in the spectral index for protons is estimated to be ± 0.01 , and for helium ± 0.07 . For the energy range of this analysis, helium nuclei make up about 30% of the flux of nucleons as a function of kinetic energy per nucleon. Scaling the individual spectral index uncertainties by the fraction of the total flux for that component gives an estimate of ± 0.03 for the uncertainty in the overall spectral index. Hence, affecting the conventional and the prompt atmospheric neutrino fluxes, we have the following theoretical uncertainties:

$$\begin{aligned} A & 0.75 \text{ to } 1.25, \\ \Delta\gamma_A & \pm 0.03. \end{aligned} \tag{8.1}$$

The major source of uncertainty affecting only the conventional atmospheric neutrino flux is the π/K ratio at production, which can affect the zenith angle distribution of neutrinos due to the kinematics of collisions and decay. From Honda, *et al.* [17], the magnitude of the impact of this uncertainty on the zenith angle tilt is estimated to be

$$\alpha_c \pm 0.03. \tag{8.2}$$

The major sources of uncertainty for the prompt flux are the primary spectrum at the top of the atmosphere and the charm production cross sections and quark fragmentation functions [66]. From Enberg, *et al.* [66], the uncertainties associated with the normalization and spectral index of the prompt atmospheric neutrino flux, for the energy range of this analysis, are estimated to be:

$$\begin{aligned} A_p & 0.56 \text{ to } 1.25, \\ \Delta\gamma_p & \pm 0.03. \end{aligned} \tag{8.3}$$

8.2 Uncertainties in DOM Sensitivity and Ice Properties

The major sources of uncertainty in the detector response are the DOM sensitivity and the ice properties. To estimate the impact of these uncertainties, two specialized neutrino simulation datasets were created. In one dataset, the number of photons striking each DOM (proportional to the number detected) was boosted by 10%. In the other dataset, the number of photons was reduced by 10%. From this, it was found that the $\pm 10\%$ change to the photon flux lead to a $\pm 15\%$ change in event rate, a ± 0.09 change in the apparent spectral index, and a ∓ 0.01 change in the apparent zenith angle tilt. These “apparent” changes were found from forward

folding fits that reweighted standard atmospheric neutrino simulation to reproduce the best fit to the observed distribution of events, after final cut level, from these specialized datasets. The impact of the $\pm 10\%$ change in photon flux in the specialized simulation was directly scaled to the $\pm 8\%$ uncertainty in DOM sensitivity.

To estimate the change in the number of photons striking an average DOM due to changes in ice properties, a diffuse flux approximation was used. First, we assume a mean attenuation length $\lambda_p = 30$ m with 10% uncertainty. Then, we estimate the change in the photon flux at a certain distance as

$$\begin{aligned}
 N &\sim e^{-\frac{d}{\lambda_p}}, \\
 N' &\sim e^{-\frac{d}{(1\pm.1)\lambda_p}}, \\
 \frac{N'-N}{N} &\sim e^{\frac{\pm.1d}{(1\pm.1)\lambda_p}} - 1,
 \end{aligned}
 \tag{8.4}$$

where N is the number of photons at distance d for the nominal attenuation length and N' is the number of photons at distance d for the perturbed attenuation length (nominal $\pm 10\%$). The third equation is the fractional change in number of photons at distance d . The average distance d per event was estimated from simulation. The net result of this approximation is that the photon flux reaching the DOMs is estimated to change by $\pm 12\%$, on average, due to ice property uncertainties. The thumbrules derived from the specialized simulation, above, were scaled by this factor to account for the impact of ice property uncertainties. Limitations in this approximation method include the fact that changes in ice properties would change the light propagation distances and the distribution of photon arrival times at the hit DOMs, effects which are not accounted for here.

Adding the uncertainties in detector response due to DOM sensitivity and ice

properties in quadrature leads to the following estimate of the associated nuisance parameters

$$\begin{aligned}
 B &= 1.0 \pm 0.22, \\
 \Delta\gamma_B &= \pm 0.13, \\
 \alpha_B &= \pm 0.02.
 \end{aligned}
 \tag{8.5}$$

Note that the range on α was not very well constrained by the forward folding fits, it was essentially at the limit of sensitivity of the forward folding to resolve it. Also, the change in normalization is correlated with the change in spectral slope.

8.3 Other Sources of Uncertainty

From Achterberg *et al.* [131], a 3% uncertainty in the charged current, deep-inelastic neutrino-nucleon scattering cross section is estimated to lead to a 3% uncertainty in neutrino event rates. Similarly, uncertainties in muon energy loss are estimated to lead to a 1% uncertainty in neutrino event rates. Background contamination in the final event sample is estimated to be less than 1%. Reconstruction and cut biases are estimated to introduce a 2% error in event rate. Adding these in quadrature gives the normalization uncertainty

$$C = 1.0 \pm 0.04.
 \tag{8.6}$$

8.4 Summary of Nuisance Parameters

The nuisance parameters are summarized in Table 8.1, where ε is the overall normalization factor,

$$\varepsilon = A \times B \times C, \quad (8.7)$$

and

$$\Delta\gamma = \Delta\gamma_A + \Delta\gamma_B \quad (8.8)$$

is the overall spectral index correction factor. The range of uncertainty for ε is estimated as

$$\frac{\sigma_\varepsilon^2}{\varepsilon^2} = \frac{\sigma_A^2}{A^2} + \frac{\sigma_B^2}{B^2} + \frac{\sigma_C^2}{C^2}. \quad (8.9)$$

Since $A \sim B \sim C \sim 1$, we can approximate the uncertainty on ε as

$$\sigma_\varepsilon^2 \approx \sigma_A^2 + \sigma_B^2 + \sigma_C^2. \quad (8.10)$$

Similarly,

$$\sigma_{\Delta\gamma}^2 \approx \sigma_{\Delta\gamma_A}^2 + \sigma_{\Delta\gamma_B}^2. \quad (8.11)$$

8.5 Additional Uncertainty Evidenced by Data/Simulation Mismatch

Fig. 8.1 shows the zenith distribution of events in data and in simulation. There is an apparent excess of events in data, or a deficit in simulation, between $90 - 97^\circ$. Fig. 8.2 shows the statistical significance of the differences between bin counts in data and in simulation, for bins in the dE/dX versus $\cos\theta_Z$ histograms. This figure is based on the intended zenith binning from 90 to 180° . After cutting

Table 8.1: Summary of Nuisance Parameters.

Parameter	Range	Definition
A	1 ± 0.25	Normalization uncertainty (theoretical)
B	1 ± 0.22	Normalization uncertainty (DOM/Ice)
C	1 ± 0.04	Normalization uncertainty (miscellaneous)
$\Delta\gamma_A$	± 0.03	Spectral index uncertainty (theoretical)
$\Delta\gamma_B$	± 0.13	Spectral index uncertainty (DOM/Ice)
A_p	$0.56 - 1.25$	Prompt flux normalization uncertainty (theoretical)
$\Delta\gamma_p$	± 0.03	Prompt flux spectral index uncertainty (theoretical)
α	± 0.02	Zenith angle tilt uncertainty (DOM/Ice)
α_c	± 0.03	Conventional flux zenith angle tilt uncertainty (theoretical)

out events between 90 and 97° , and re-binning to once again have 10 bins in $\cos\theta_Z$, the statistical significance of the remaining mismatch is as indicated in Fig. 8.3.

Several checks and investigations were performed to try to identify the origin of the mismatch near the horizon. First, it can not be mimicked within the theoretical uncertainties in the atmospheric neutrino flux model or predictions for a diffuse flux of astrophysical neutrinos. Also, distributions of track quality parameters do not reveal any problems. In simulation of atmospheric muons, the background shows up first at lower BDT values and near the top of the detector. The excess in the data does not exhibit this behavior. The fractional excess remains as the BDT cut is increased beyond 0.73. Fig. 8.4 shows the distributions of the z-component of the center of gravity (COG) variable for events in the zenith range $90 - 97^\circ$. COG is the location of the center of gravity of the measured charge from the DOMs contributing to the event. For these near-horizontal events, COG_Z is approximately the depth of the event. The horizontal excess in data does not decrease with depth.

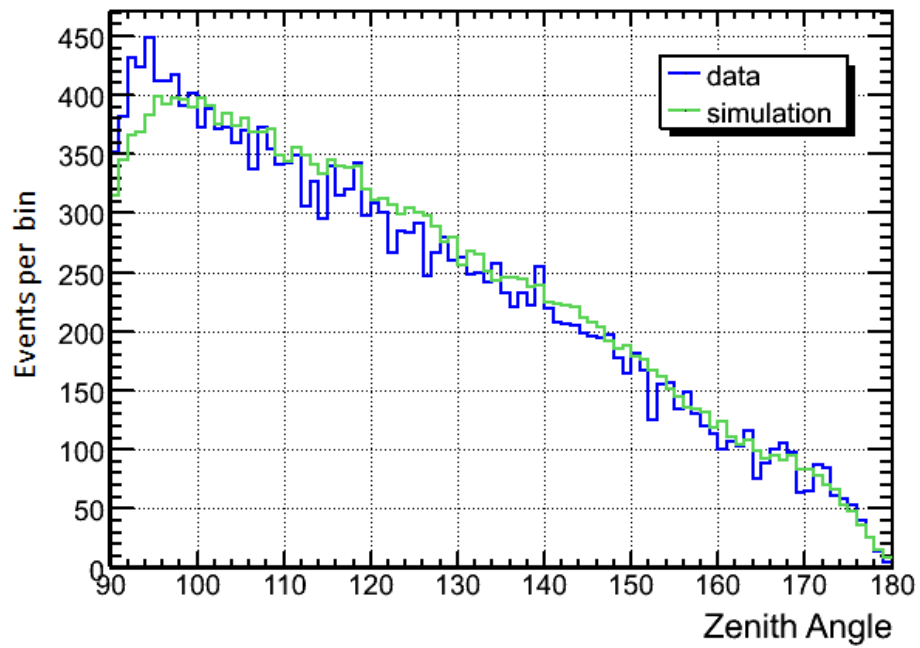


Figure 8.1: Zenith distribution of events in data and simulation. Data is blue, simulation is green. There is an apparent excess of events in data, or deficit in simulation, between 90 and 97°.

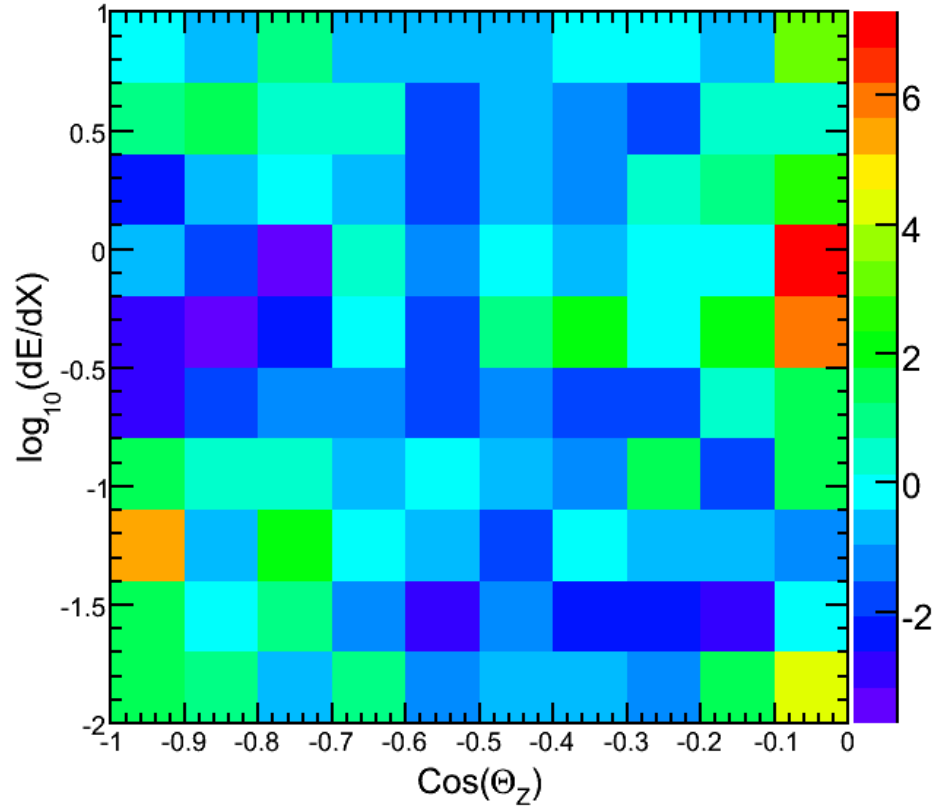


Figure 8.2: Bin-wise data/simulation comparison. This plot shows the statistical significance of the disagreement between data and simulation in each of the 100 bins of the dE/dX versus $\cos\theta_Z$ histograms. Statistical significance is computed as $(n_{ij}^{data} - \mu_{ij}^{sim}) / \sqrt{\mu_{ij}^{sim}}$. Positive numbers are an excess in data.

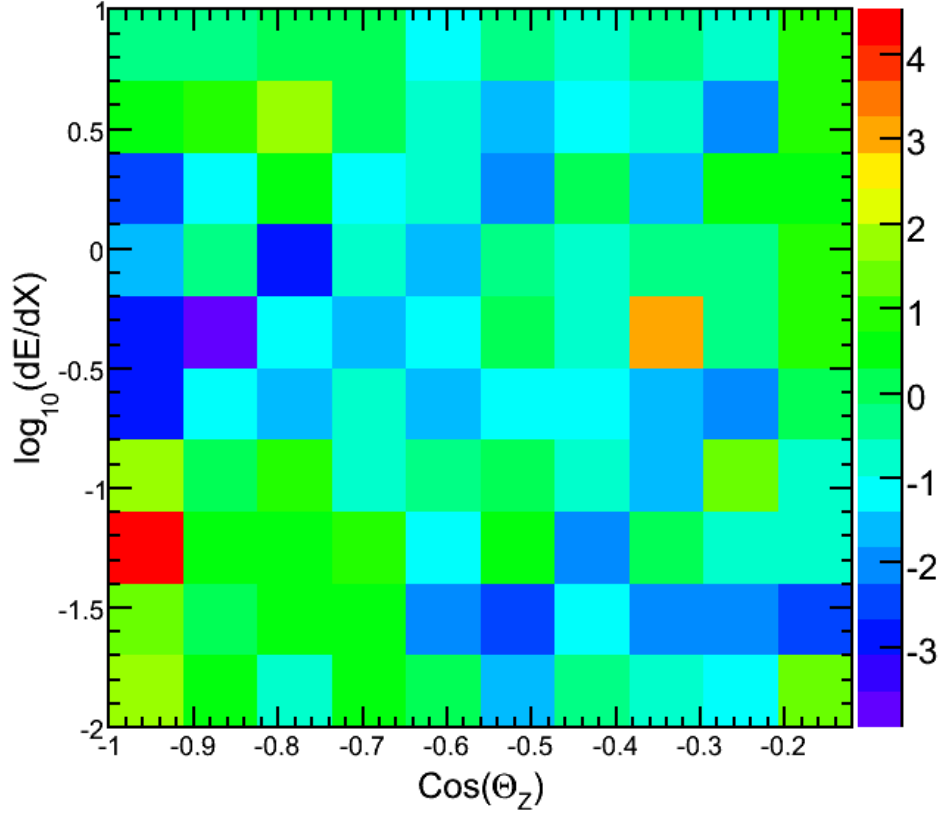


Figure 8.3: Bin-wise data/simulation comparison after additional zenith cut at 97° , and re-binning in $\cos\theta_z$. This plot shows the statistical significance of the disagreement between data and simulation in each of the 100 bins of the dE/dX versus $\cos\theta_z$ histograms. Statistical significance computed as $(n_{ij}^{data} - \mu_{ij}^{sim}) / \sqrt{\mu_{ij}^{sim}}$. Positive numbers are an excess in data.

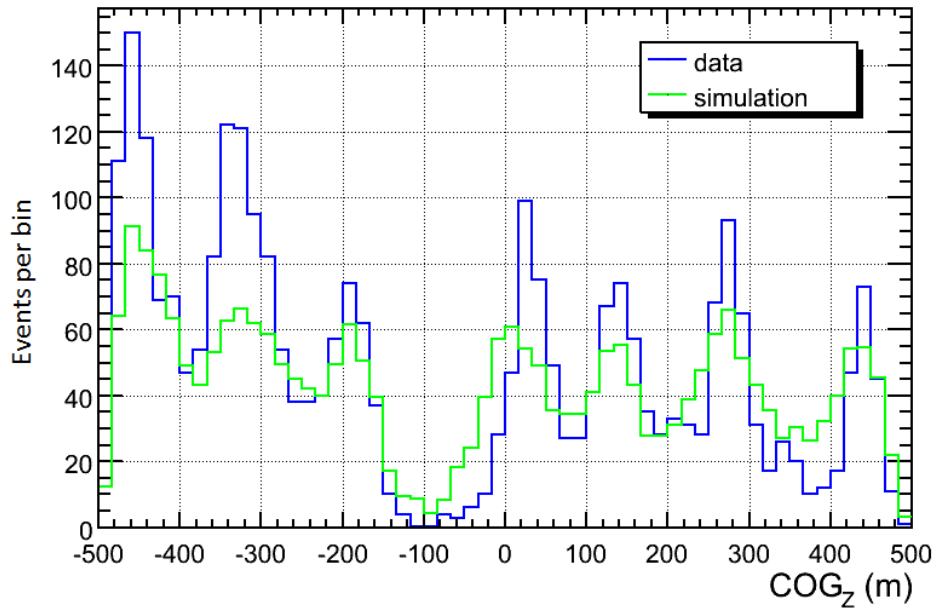


Figure 8.4: Distributions of the z component of the COG variable for events in the zenith range $90 - 97^\circ$. COG is the location of the center of gravity of the measured charge from the PMTs contributing to the event. For these near horizontal events, COG_z is approximately the depth of the event. Data is blue, simulation is green. Note the excess in data at each of the clean ice layers.

The horizontal excess is not a problem specifically related to training the BDTs and their performance near the horizon. An independent analysis that used straight cuts and no BDT for background rejection saw a similar excess. A subset of events were also examined in a software-based event viewer. All of these tests indicated that the excess is consistent with horizontal, neutrino-induced muon tracks. The problem could be related to errors in the neutrino flux calculation near the horizon, or the impact of atmospheric variability on the energy and zenith distribution of atmospheric neutrinos. However, since the origin of this problem could not be verified, the region from 90 to 97° was excluded from each of the analyses.

To further investigate the horizontal event rate and COG_Z disagreements, neutrino simulation was generated using a modified ice model. The modified ice model was a somewhat arbitrary modification to the standard ice model. The depth-dependent variations in scattering and absorption in the clean layers were intensified by doubling the variations of the coefficients for absorption and scattering from their mean values. Where absorption and scattering are below the mean, the amount by which they are below the mean was doubled. Different mean values were used for ice above and below the large dust peak (above and below 2100 m). The result of this test was a 7% increase in the overall event rate, but with little zenith-dependence to the increase. In particular, there was no enhanced preference for horizontal events.

Binning of photon flux parameters in the Photonics tables, and subsequent interpolation during simulation production could be smearing out the affect of the layered ice properties. This could be related to the disagreements in the COG_Z distributions of horizontal events and the difficulty in trying to reproduce, in simu-

lation, the event rate seen in the clean regions. Photonics based simulation is being compared to other methods for simulating light propagation in the ice. This work is on-going by various members of the Collaboration.

Fig. 8.5 is the same as Fig. 8.3, but with data renormalized so that the overall number of events in data agrees with simulation and the fit parameters of the forward folding applied to re-weighting events in simulation. The χ^2 per bin is 1.8 in this case, compared to about 2 prior to the fit, indicating that it is still not an overall good fit. However, more troubling than the range in bin-by-bin fluctuations is the systematic clustering of bins with excess events in data, and events with a deficit in data. The highlighted regions in Fig. 8.6 show these troublesome areas. The signal we are looking for in the VLI and decoherence models is a distortion of the flux due to a deficit of up-going high energy events. The excess of up-going low energy events and the excess of mid-energy horizontal events, as indicated in the highlighted regions of Fig. 8.6, confuses the likelihood analysis.

8.6 Seasonal Variability in the Data

Seasonal and regional variations in atmospheric conditions are expected to lead to variations in the atmospheric neutrino flux. Colder temperatures correspond to a greater air density and a shallower atmosphere. Greater atmospheric density leads to more collisions of pions and kaons prior to their decay. Hence, the production of high energy neutrinos is reduced. The converse occurs for warmer temperatures. The kinematics of collision and decay, and slant angle through the atmosphere,

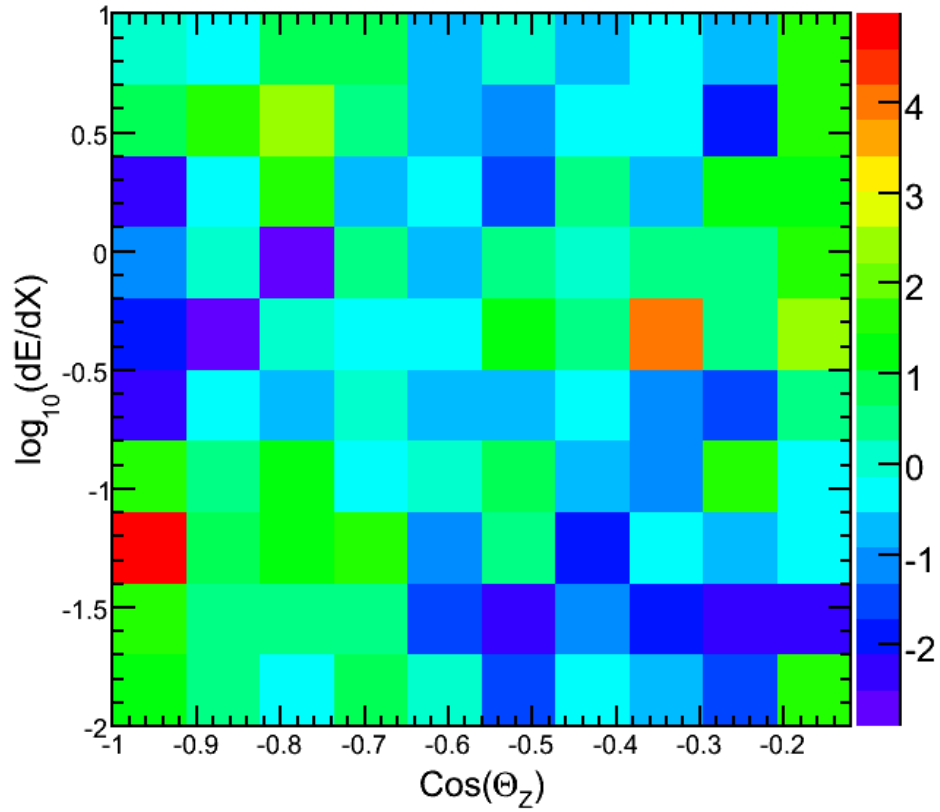


Figure 8.5: Bin-wise data/simulation comparison after additional zenith cut, with data renormalized to same overall event count as simulation and the fit parameters of the forward-folding used for re-weighting events in simulation. The plot shows the statistical significance of the disagreement between data and simulation in each of the 100 bins.

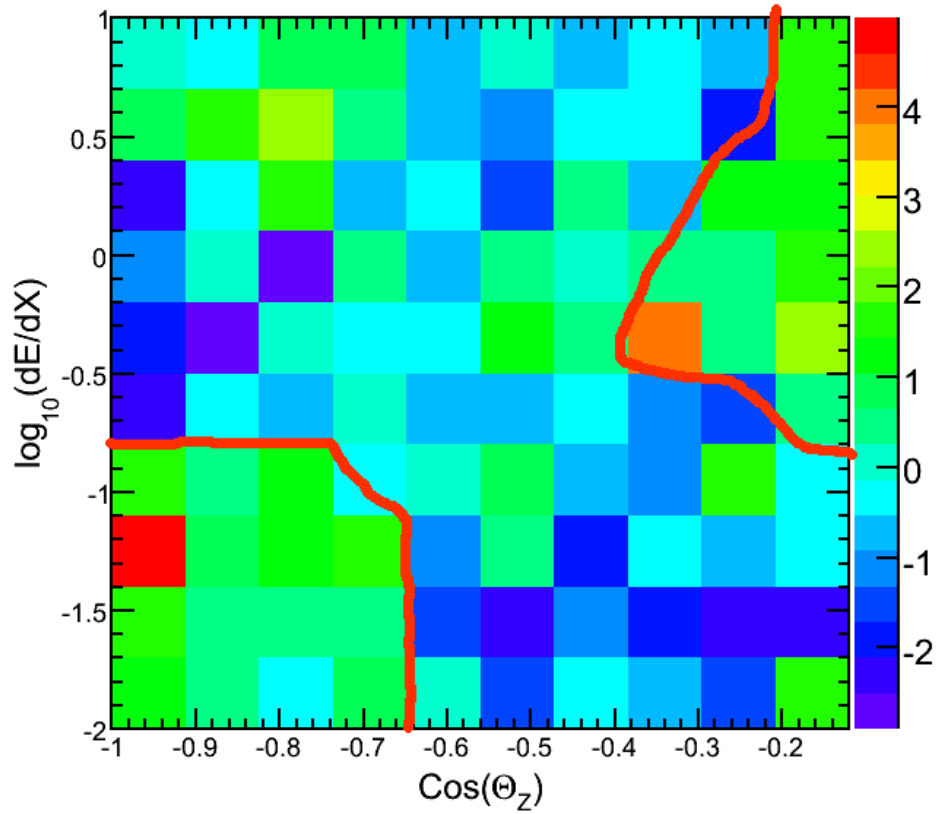


Figure 8.6: Bin-wise data/simulation comparison after additional zenith cut, with data renormalized to same overall event count as simulation, and the fit parameters of the forward-folding used for re-weighting events in simulation. This plot shows the statistical significance of the disagreement between data and simulation in each of the 100 bins, just like Fig. 8.5. Here, the systematic and problematic clustering of excess events in the data is highlighted.

complicate the impact of atmospheric variations on the energy and zenith angle dependence of neutrino production.

The normalization error on the Honda conventional atmospheric neutrino flux model due to uncertainties in the atmospheric density profile is estimated at 3% [17, 132]. This is one component already included in the normalization uncertainty nuisance parameter discussed earlier. However, the flux calculation uses an atmospheric model (the US-standard '76) that is a climatological average, and does not account for regional or seasonal variations in the temperature profile. The estimate of the error in the flux calculation is based on the error in the climatological average atmospheric density profile. So the error estimate does not account for changes in normalization, or in the energy and zenith distribution of atmospheric neutrinos, due to local and temporal atmospheric variability.

A continuous twelve month period of data was used to evaluate seasonal variations. This period is 1 May 2008, to 30 April 2009. Fig. 8.7 shows the monthly event rate over this period. The number of events in the final sample for each month is normalized by the detector live time for that month.

The twelve months were also divided into four seasons as described in Table 8.2. Fig. 8.8 shows the dE/dX and $\cos\theta_Z$ distributions for each of the four seasons. Each season has been normalized to the same average live time. The $\sim 4\sigma$ excess in the $\cos\theta_Z$ -0.4 to -0.5 bin for the February to April time period has not been explained. Figs. 8.9 and 8.10 show the azimuth and RA distributions, respectively, for this $\cos\theta_Z$ region.

Seasonal comparisons in the following plots include the full 90 to 180° range.

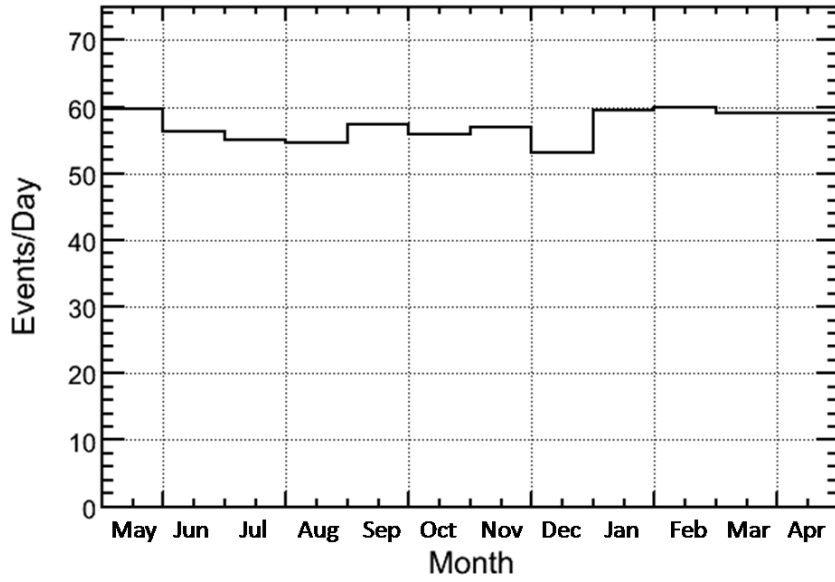


Figure 8.7: Monthly variability in event rate. Event rates are normalized to events per day of live time.

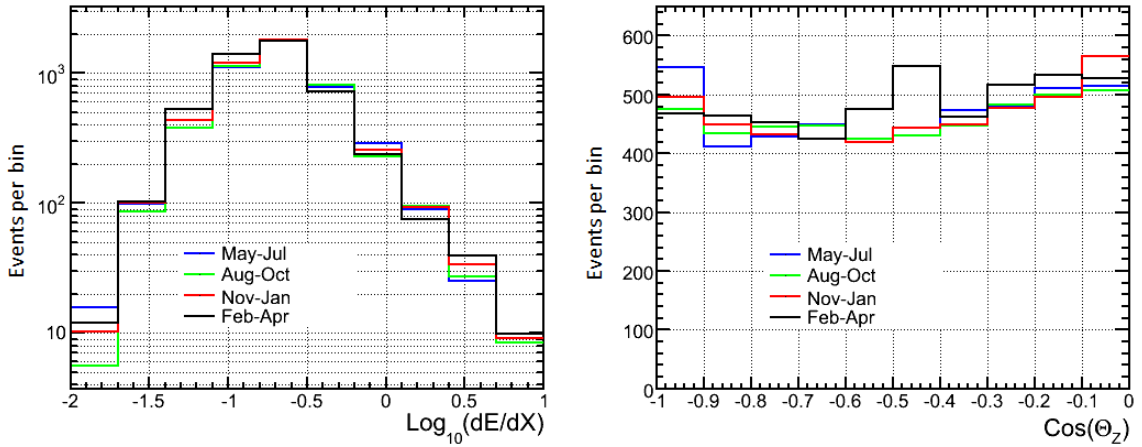


Figure 8.8: dE/dX and $\cos \theta_Z$ distributions for each of the four seasons. Each season has been normalized to the same average live time. The $\sim 4\sigma$ excess in the fifth $\cos \theta_Z$ bin from the right, for the February to April time period, has not been explained.

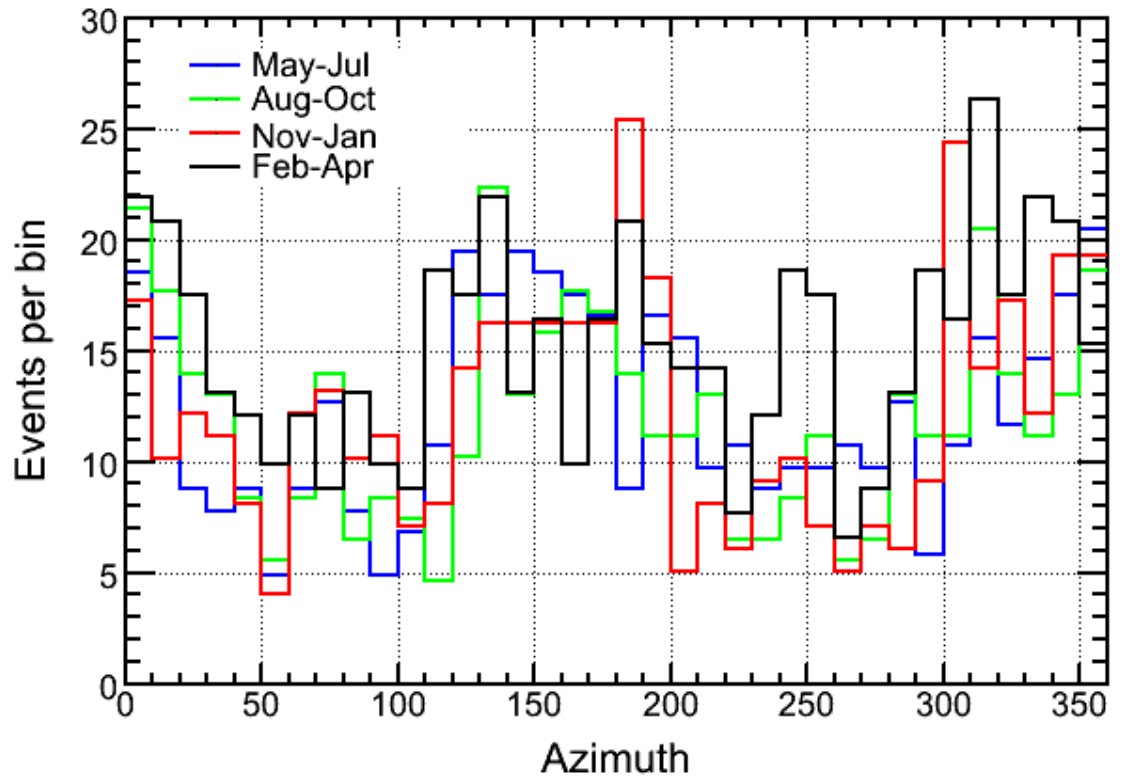


Figure 8.9: Azimuth distributions for each of four seasons, for the $\cos \theta_Z$ band -0.4 to -0.5 . Each season has been normalized to the same live time.

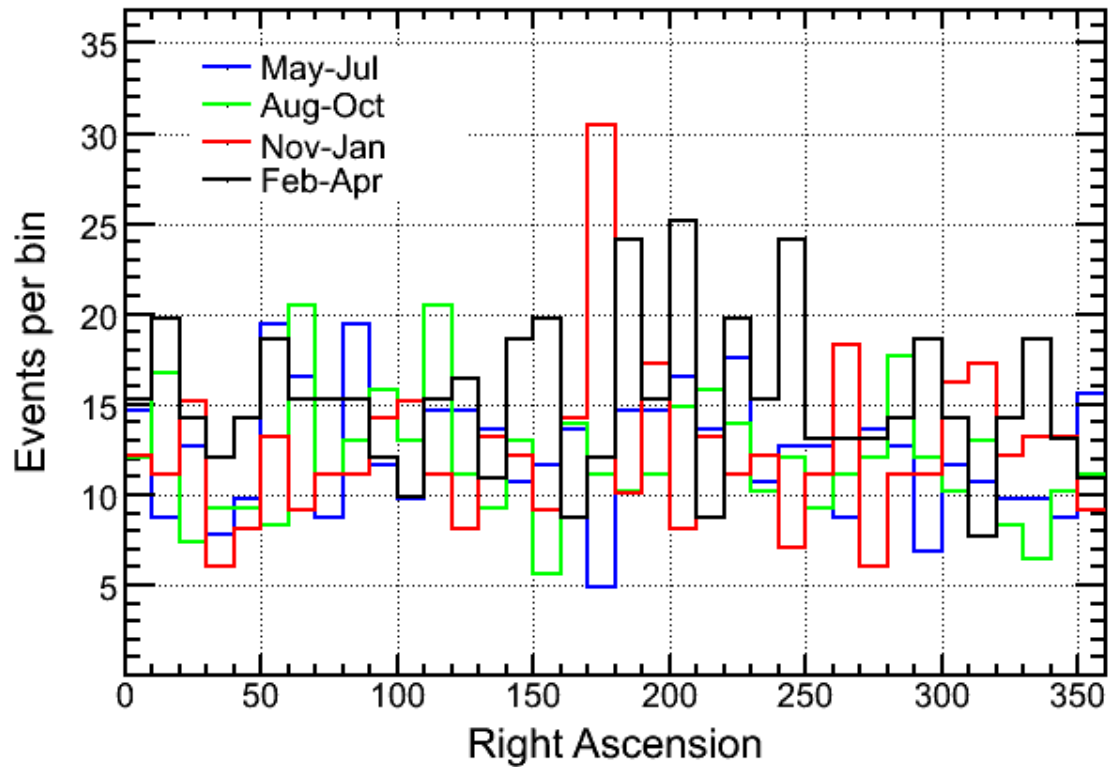


Figure 8.10: RA distributions for each of four seasons, for the $\cos\theta_Z$ band -0.4 to -0.5 . Each season has been normalized to the same live time.

Table 8.2: Seasonal Comparison of Data.

Season	Months	Events	Live Time (hrs)
1	May - July	4796	2024.2
2	Aug - Oct	4942	2122.3
3	Nov - Jan	4579	1944.4
4	Feb - Apr	4445	1800.1

Fig. 8.11 shows the bin-wise comparison of data in each season to the entire year of data. Each season and the entire year histogram have been normalized to the average seasonal live time. Fig. 8.12 shows the statistical significance of the variability indicated in Fig. 8.11. Fig. 8.13 shows the bin-wise comparison of data in each season to simulation. Each season and simulation have again been normalized to the average seasonal live time. Fig. 8.14 shows the statistical significance of the variability indicated in Fig. 8.13.

As seen from the previous plots, seasonal variability appears to exhibit features similar to that seen in the data/simulation comparisons. Seasonal and regional temperature variations in the upper atmosphere could account for some part of the data/simulation disagreement. However, statistical fluctuations are also contributing to these variations. It is not yet clear how much is due to random fluctuations and how much can be attributed to atmospheric or detector effects. More data from additional years of detector operation should clarify this picture. Additionally, members of the Collaboration are using the 40-string data sample and in situ atmospheric temperature measurements to quantify the relationship between neutrino production rates and variations in atmospheric temperature profiles. This atmo-

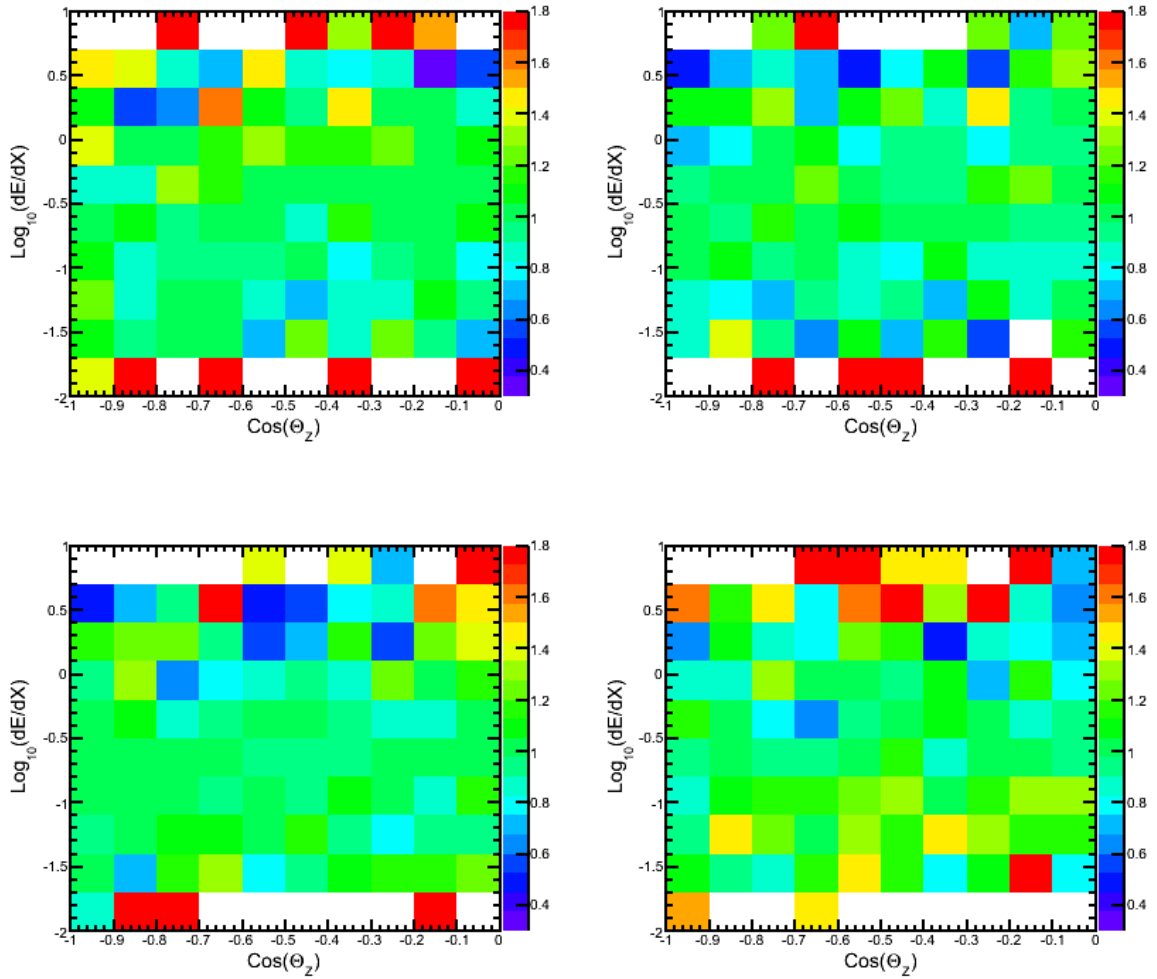


Figure 8.11: Bin-wise comparison of data in each season to entire year of data. Each season and the entire year histogram have been normalized to the average seasonal live time. Each bin shows the ratio of the number events in that bin for the particular season to the average. Top left is season 1; top right is season 2; bottom left is season 3; bottom right is season 4. The color scale is clipped at 0.3 to 1.8 for ease of comparison between each plot, creating some small errors in the red or purple bins if this range is exceeded.

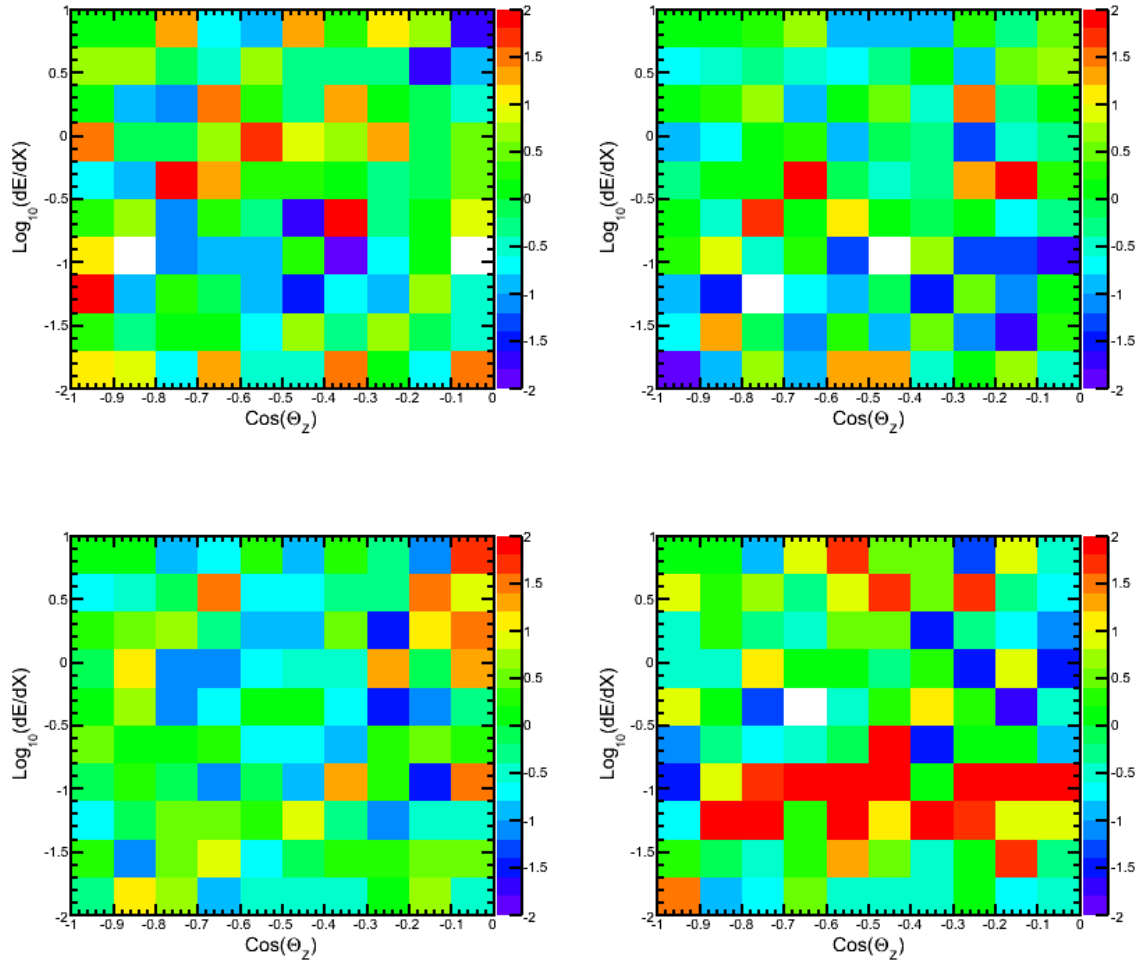


Figure 8.12: Statistical significance for bin-wise, seasonal comparison of data. Each bin shows the difference between the number events in that bin for the particular season and the average, divided by the square-root of the average. Top left is season 1; top right is season 2; bottom left is season 3; bottom right is season 4. The color scale is clipped at -2 to 2 for ease of comparison between each plot, creating some small errors in the red or purple bins if this range is exceeded.

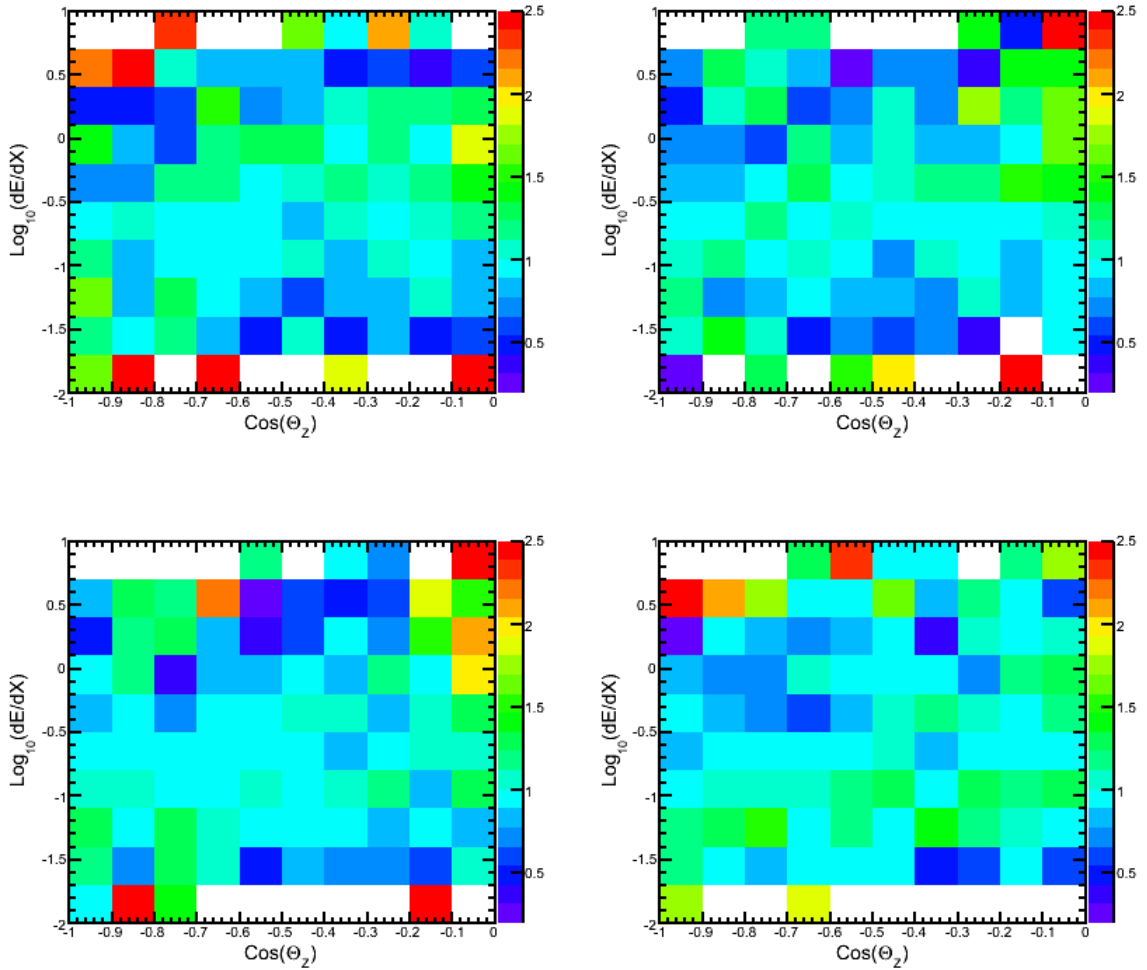


Figure 8.13: Bin-wise comparison of data in each season to simulation. Each season and simulation have been normalized to the average seasonal live time. The color scale is clipped at 0.2 to 2.5 for ease of comparison between each plot, creating some small errors in the red or purple bins if this range is exceeded.

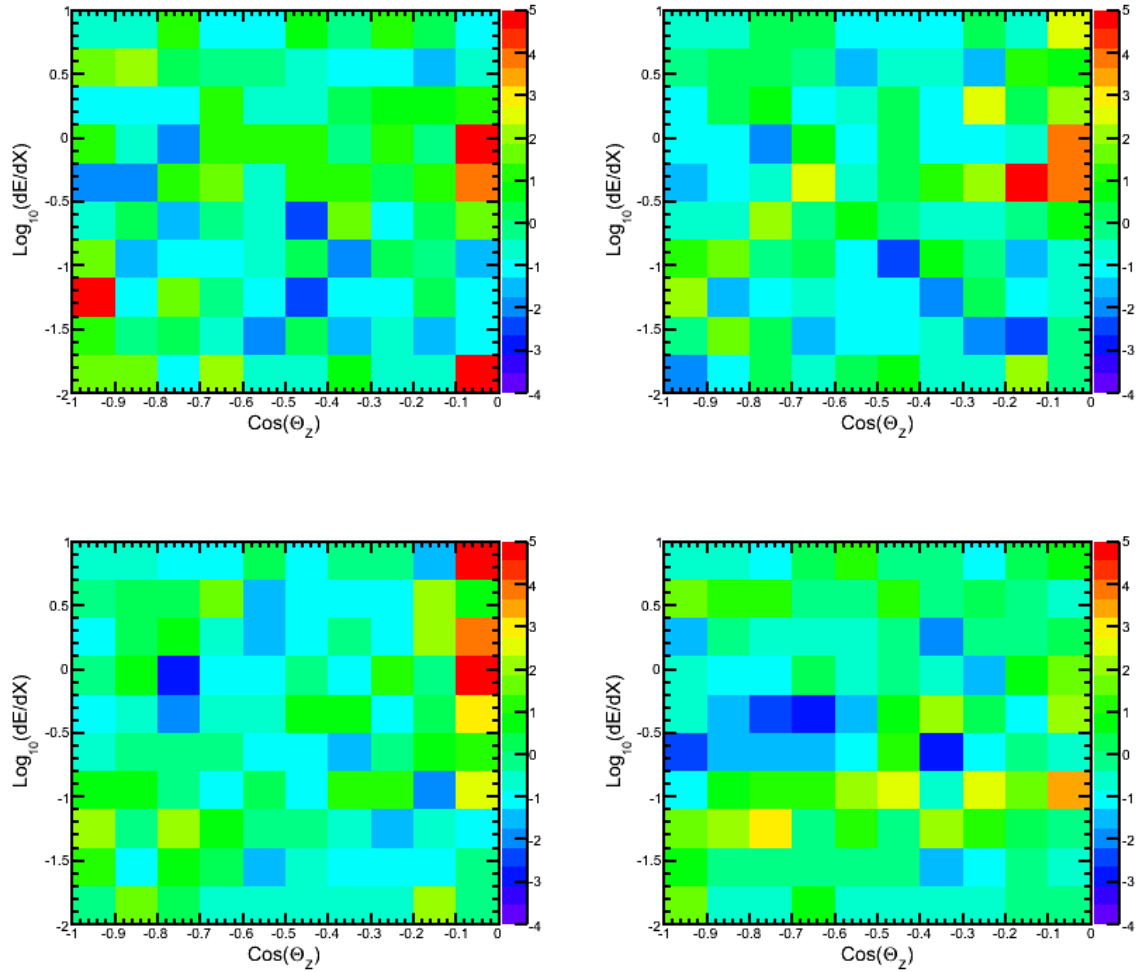


Figure 8.14: Statistical significance for bin-wise, seasonal comparison of data to simulation. The color scale is clipped at -4 to 5 for ease of comparison between each plot, creating some small errors in the red or purple bins if this range is exceeded.

spheric neutrino data sample will be used to compute zenith-dependent correlation coefficients that relate corrections to the neutrino flux to deviations in the effective temperature of the atmosphere.

CORSIKA was also used to evaluate the impact of seasonal variations on the atmospheric neutrino flux. The flux of down-going muon neutrinos produced by cosmic ray air showers for five different atmospheres were examined. The atmospheres were standard South Pole atmospheres for the months of January, March, July, October, and December, parameterized and available within CORSIKA. This down-going neutrino flux does not directly correspond to the up-going flux that this analysis is based on. The simulation in this CORSIKA-based study did not include propagation through the Earth, interaction in or near the detector, and event selection cuts. However, by looking at variations in the neutrino rate at production, and in the energy and zenith-dependence of the rate, we can still assess the importance of atmospheric variability.

Fig. 8.15 shows the energy and zenith distributions for the CORSIKA-generated muon neutrino flux for each of five atmospheres. Figs. 8.16, 8.17, and 8.18 compare the shapes of the energy and zenith distributions from each month to the average of the five months. In these plots that show the bin-wise ratio of number of events and the statistical significance of the differences, the total number of events in each of the five data sets has been normalized to the same value, so that the plots are just evaluating differences in the shapes of the distributions. Similar to the seasonal data comparisons, this study indicates that atmospheric variability can play an important role in the two-dimensional likelihood analysis.

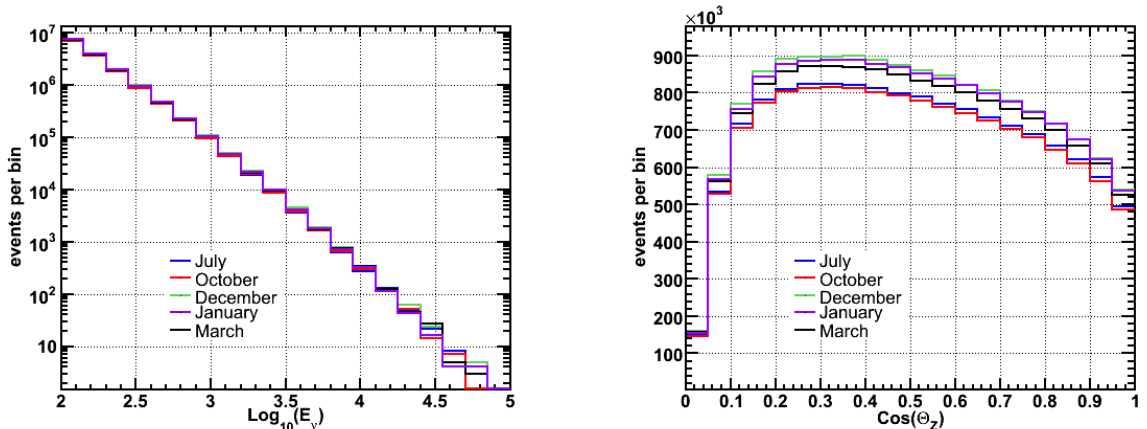


Figure 8.15: E_ν and $\cos\theta_Z$ distributions for each of five South Pole atmospheres, from CORSIKA. Note that this is a flux of down-going neutrinos.

8.7 Other Possible New Physics Effects: Neutrino Cross Sections

Possible uncertainties in neutrino cross sections beyond the 3% discussed earlier were investigated. Testing showed that it is possible to arbitrarily tune the cross sections and improve the fit to the horizontal excess. However, plausible errors in the parton distribution functions, or new physics effects, turn on too late to make a realistic difference at the energy levels of this data sample. Uncertainties in PDFs would affect CC and NC cross sections, but are not expected to be significant until well above a PeV. Various theoretical and phenomenological models of new physics predict significant enhancements to NC cross sections [133, 134, 135], however these are also not expected to be consequential until above about a PeV. These models include large extra dimensions and Kaluza-Klein gravitons, TeV string resonances, production of microscopic black holes, and electroweak instanton fields.

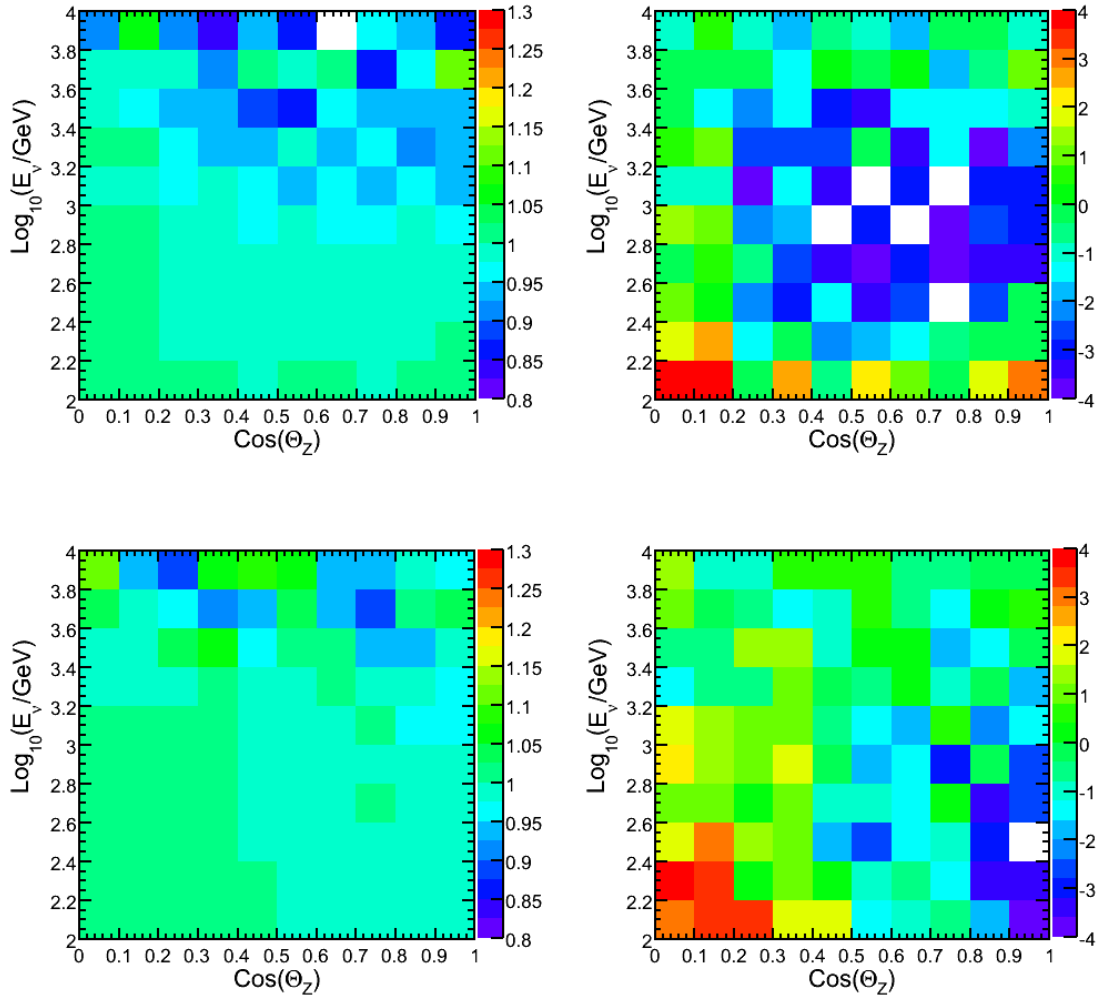


Figure 8.16: Bin-wise comparison of the neutrino event rates from the July (top) and October (bottom) CORSIKA samples, to the average. Bin-wise ratios are on the left. Statistical significance of the difference between the event rate for the given month and the average is on the right. The total number of events from July and October have been normalized to the average value, so that the plots show differences in the shapes of the distributions. For ease of comparison between figures, the color scale has been clipped at 0.8 to 1.3 for the ratio plots, and -4 to 4 for the significance plots.

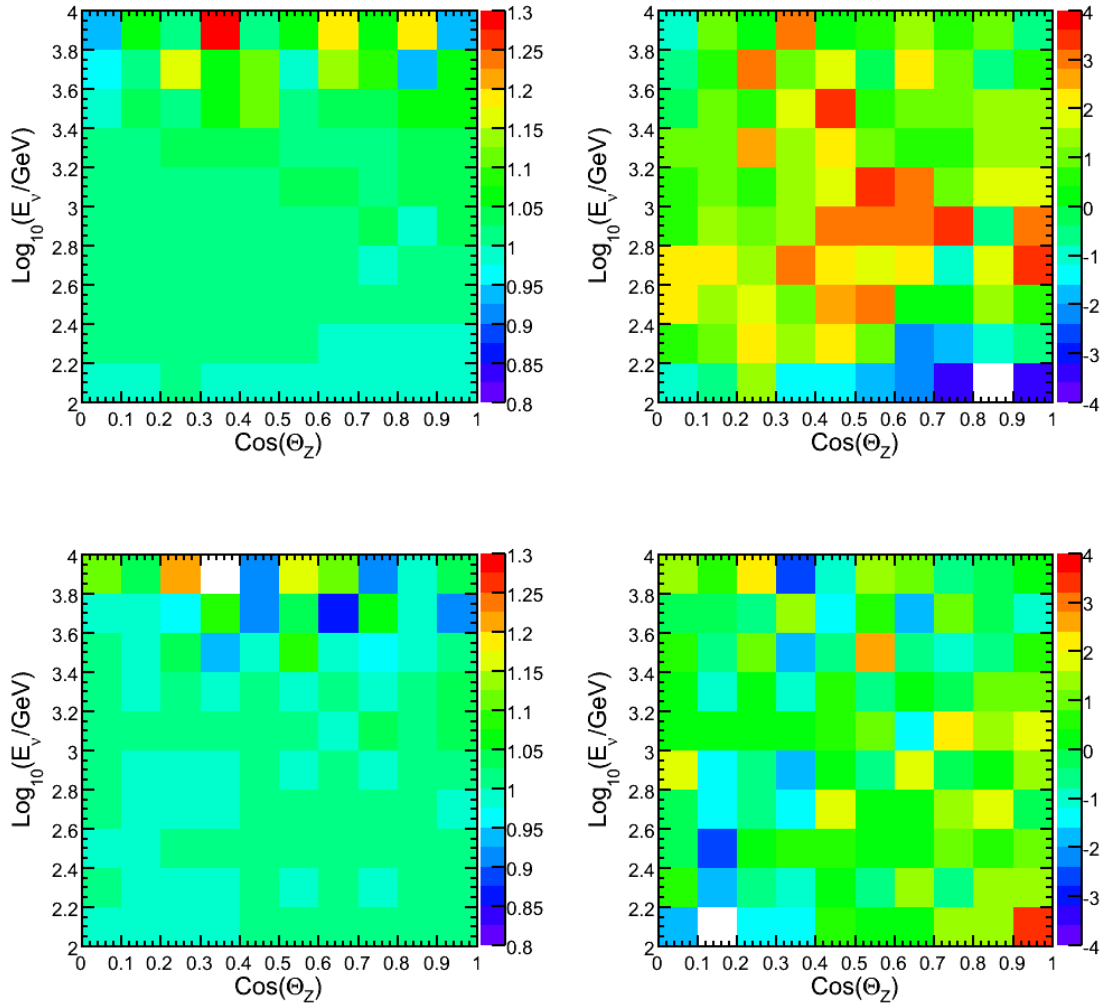


Figure 8.17: Bin-wise comparison of the neutrino event rates from the March (top) and December (bottom) CORSIKA samples, to the average. Bin-wise ratios are on the left. Statistical significance of the difference between the event rate for the given month and the average is on the right. The total number of events from July and October have been normalized to the average value, so that the plots show differences in the shapes of the distributions. For ease of comparison between figures, the color scale has been clipped at 0.8 to 1.3 for the ratio plots, and -4 to 4 for the significance plots.

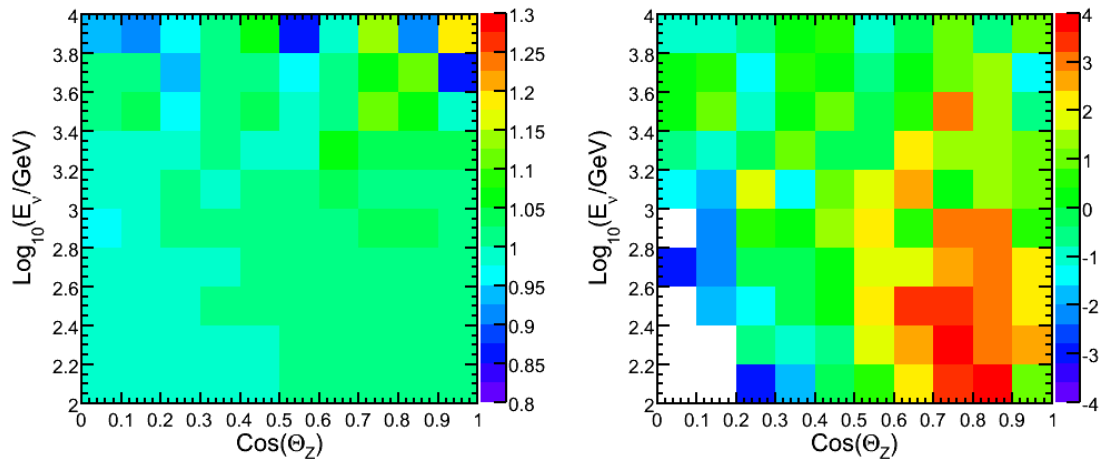


Figure 8.18: Bin-wise comparison of the neutrino event rates from the January CORSIKA sample, to the average. Bin-wise ratios are on the left. Statistical significance of the difference between the event rate for the given month and the average is on the right. The total number of events from July and October have been normalized to the average value, so that the plots show differences in the shapes of the distributions. For ease of comparison between figures, the color scale has been clipped at 0.8 to 1.3 for the ratio plots, and -4 to 4 for the significance plots.

Chapter 9

Results

9.1 Atmospheric Neutrino Flux Unfolding

Fig. 9.1 shows the distributions, comparing data to simulation, for the observable dE/dX used for the unfolding. The additional cut at zenith angle of 97° has been applied. The results of the atmospheric neutrino spectrum unfolding can be seen in Fig. 9.2. The blue lines indicate the unfolded spectrum and estimated uncertainty. The red line is the simulated spectrum that provided the basis for the response matrix. Note that this is the zenith-averaged flux for the region $97 - 180^\circ$.

The major uncertainties in the unfolded result come from six sources. These are the homogeneous uncertainties in DOM sensitivity and ice properties, the zenith-dependent data/simulation mismatch, statistical uncertainties, the impact of the regularization process, errors in the response matrix due to event weighting in simulation, and miscellaneous normalization errors. The bin-by-bin values for each of these error sources are added in quadrature to obtain the final error estimate for each bin of the unfolded result.

The impact of statistical fluctuations in the data, i.e. Poisson variability of bin counts, was determined using toy MC experiments. The toy spectrum was made systematically different from simulation by re-weighting events according to the output of the forward folding fit, to mimic the data. The results of the forward

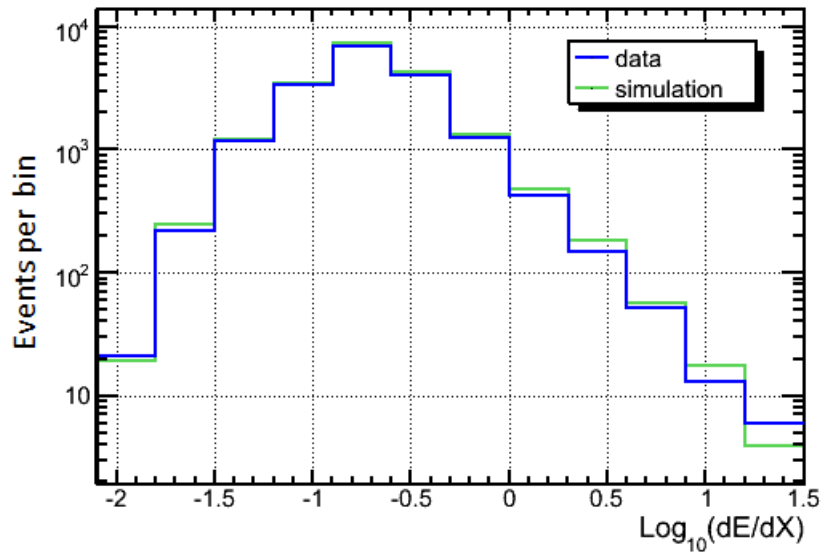


Figure 9.1: Distributions of the dE/dX observable, for data (blue) and simulation (green), for the event sample used in the unfolding.

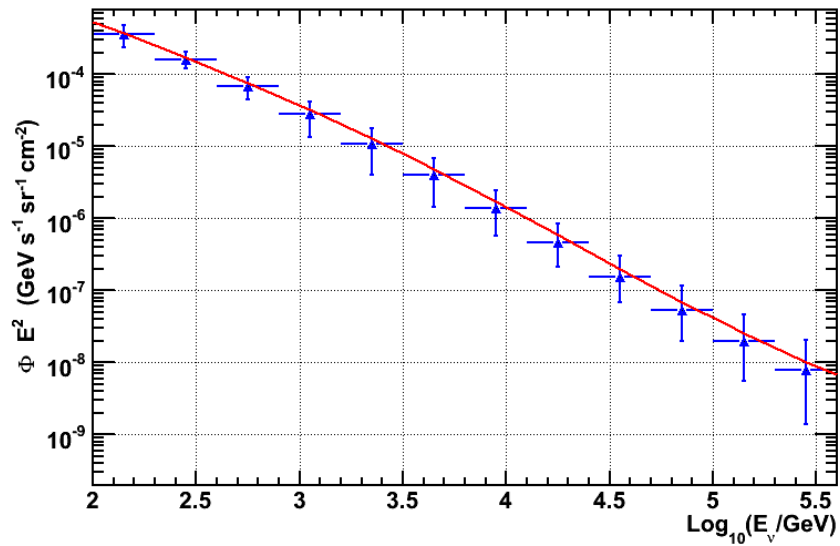


Figure 9.2: Results of the atmospheric neutrino spectrum unfolding. The blue lines indicate the unfolded spectrum and estimated errors. The red line is the simulated spectrum that provided the basis for the response matrix. This is the zenith-averaged flux for the region $97 - 180^\circ$.

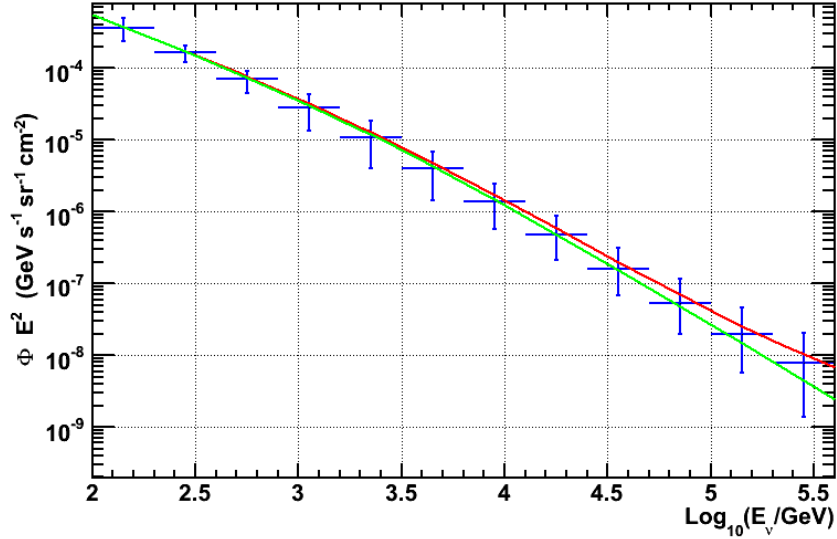


Figure 9.3: Comparison of the result of the forward folding fit (green) to the baseline simulation (red) and the unfolded result (blue). Not shown is the uncertainty in the forward folding result.

folding fit were $\varepsilon = 0.95$, $\Delta\gamma = -0.03$, $\alpha = 0.02$, and $A_p = 0$. Fig. 9.3 compares the result of the forward folding fit (green) to the baseline simulation (red) and the unfolded result (blue). 1000 trials were performed with the bin counts in each toy dE/dX distribution varied in a Poisson fashion. The errors in each bin of the unfolded results were computed and the 90th percentile for the errors in each bin were assigned as the errors due to statistical uncertainties. The result of this analysis is shown in Fig. 9.4, where the errors in each bin are given as percent of the true flux.

Recall from Chapter 8, and the discussion of systematic uncertainties due to DOM sensitivity and ice property measurement errors, that detector uncertainties lead to quantitative uncertainties in the apparent neutrino flux. For a given detector

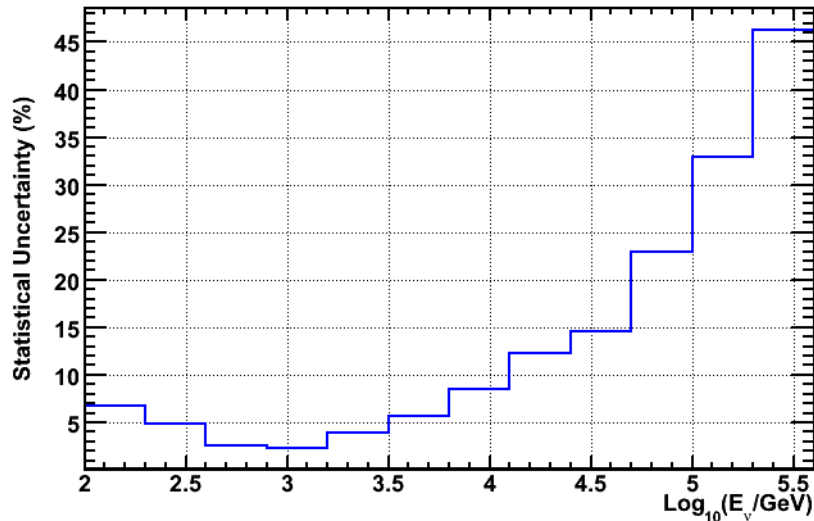


Figure 9.4: Statistical uncertainties in the unfolded result. From toy MC studies.

response, i.e. a measurement of the dE/dX distribution, the true normalization, spectral index, and zenith angle tilt of the neutrino flux can not be constrained better than allowed by the nuisance parameters derived for DOM sensitivity and ice property uncertainties. Fig. 9.5 shows the resulting range of uncertainty in the atmospheric neutrino spectrum.

In Chapter 8, we also showed that there were some apparent, systematic differences between the data and simulation, with energy and zenith-dependence that are not explained by the theoretical or experimental nuisance parameters. Fig. 8.6 showed a different behavior on the left side (more upgoing events) of that plot, compared to the right side (more horizontal events). A zenith angle cut of 124° splits that plot in half and also splits the data sample in half. So an unfolding performed with events in the zenith range $97 - 124^\circ$ was performed, as well as an unfolding

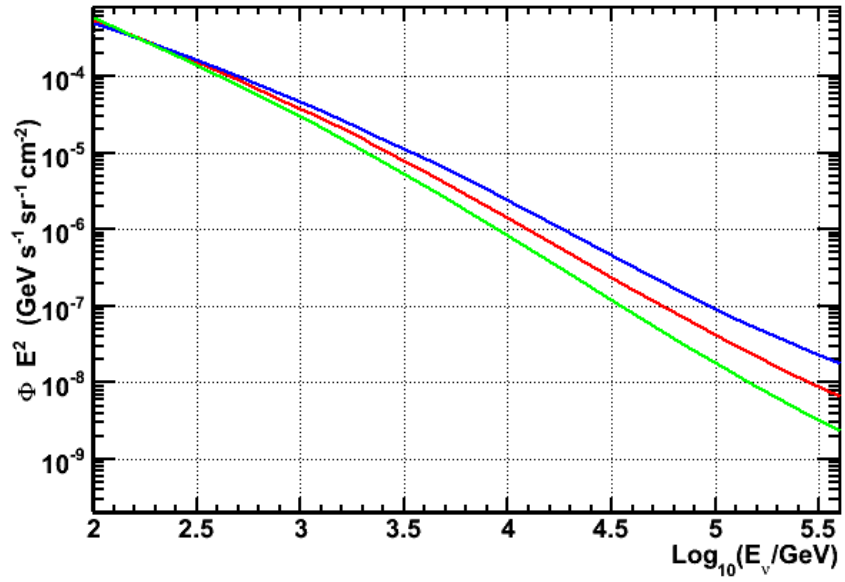


Figure 9.5: Possible variability in the true flux allowed by DOM and ice property uncertainties. Red is the predicted atmospheric neutrino flux ([17, 66]) used to train the unfolding algorithm. Blue and green are the maximum and minimum, respectively, of the range of variability consistent with DOM sensitivity and ice model uncertainties.

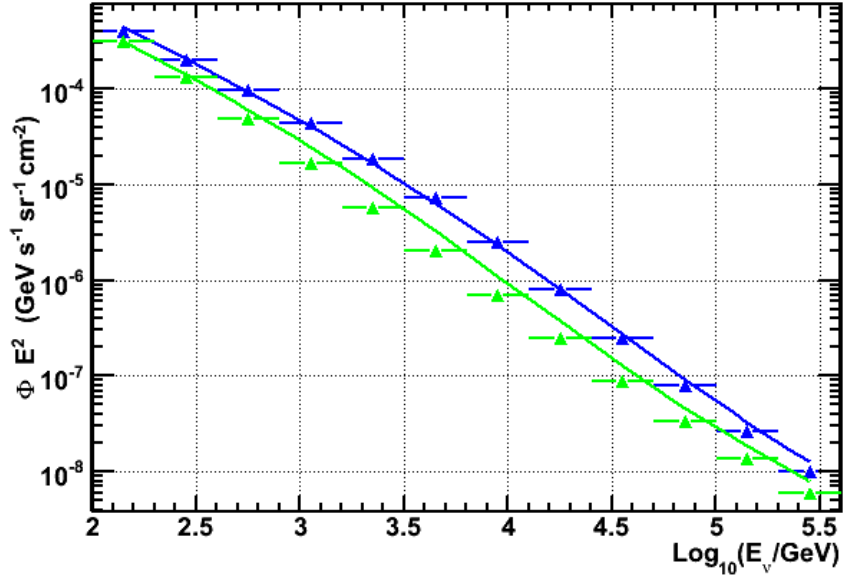


Figure 9.6: Comparison of unfolded spectra for different zenith regions. Separate unfoldings were performed for the zenith range $97 - 124^\circ$ (blue) and the zenith range $124 - 180^\circ$ (green). The unfolded results for each region and the predicted spectrum corresponding to each region are shown.

using the zenith range $124 - 180^\circ$. The results of these tests are shown in Fig. 9.6, as well as the predicted spectrum corresponding to each region. Each unfolded result differs from its associated prediction, but in different ways. For the upgoing region (green in Fig. 9.6), the unfolded result is significantly less than predicted for middle and higher energies. For the horizontal region (blue in Fig. 9.6), the unfolded result is slightly higher than predicted for middle energies and slightly less than predicted at higher energies. This contrasting behavior is consistent with the data/simulation comparison in Fig. 8.6. The relative differences between result and prediction for the two zenith regions is taken as an estimate of the impact of the anisotropic uncertainties.

The choice of regularization parameter fixes the amount of smoothing that is

applied to the unfolded solution, hence, the amount of bias between the shape of the simulated distribution and fluctuations in the data. As discussed in Chapter 7, testing indicated that the optimal choice for this was given by a value of $kterm = 3$ as input to the SVD unfolding algorithm. Some systematic error due to the regularization process is already accounted for in the toy MC study used to estimate statistical uncertainties. That is because the toy MC experiments were systematically as well as statistically different from the reference simulation. However, the nature of the regularization process is that it can hide features in the true spectrum that are not present in the simulated spectrum. Such features would also not be revealed by the forward folding fit. To estimate the extent by which this could be occurring, the unfolding was repeated for various values of $kterm$. Fig. 9.7 shows the unfolded result for different values of $kterm$. The disagreements between the result with $kterm = 3$, and the results for $kterm = 2$ or 4, are taken as the uncertainty.

The response matrix maps the measured muon dE/dX distribution to the distribution of neutrino energies. It is created from simulation and is therefore subject to numerical and statistical errors in the weights assigned in simulation. If no errors were present, due to rounding of weighting factors or a finite event sample, for example, then dividing the final simulated distribution by the numerically computed effective area (Fig. 6.7) should reproduce the original spectrum. However, Fig. 9.8 shows the differences between the zenith-averaged flux from [17, 66] and the result after converting the simulated final event distribution back to the original flux using effective area. This disagreement provides an estimate of the impact of event weighting errors.

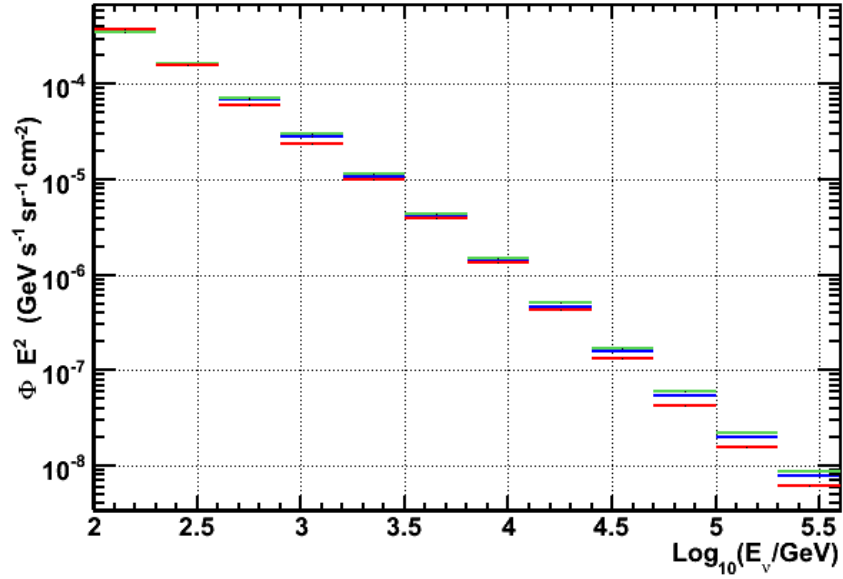


Figure 9.7: Unfolded result for various values of $kterm$. Blue is $kterm = 3$ (nominal result), green is $kterm = 2$ (less biased toward data), red is $kterm = 4$ (more bias toward data).

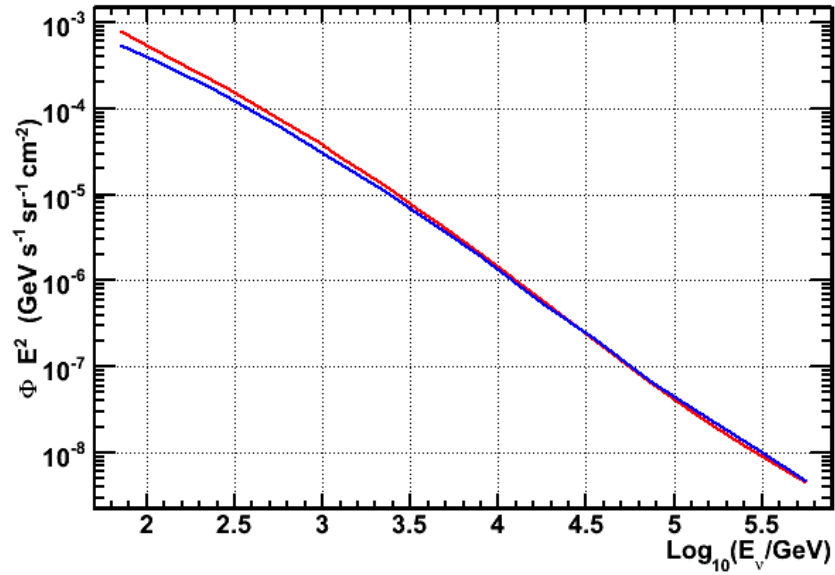


Figure 9.8: Introduction of errors through event weighting in simulation. Red is the zenith-averaged flux from [17] and blue is the result after converting the simulated final event distribution back to the original distribution using effective area.

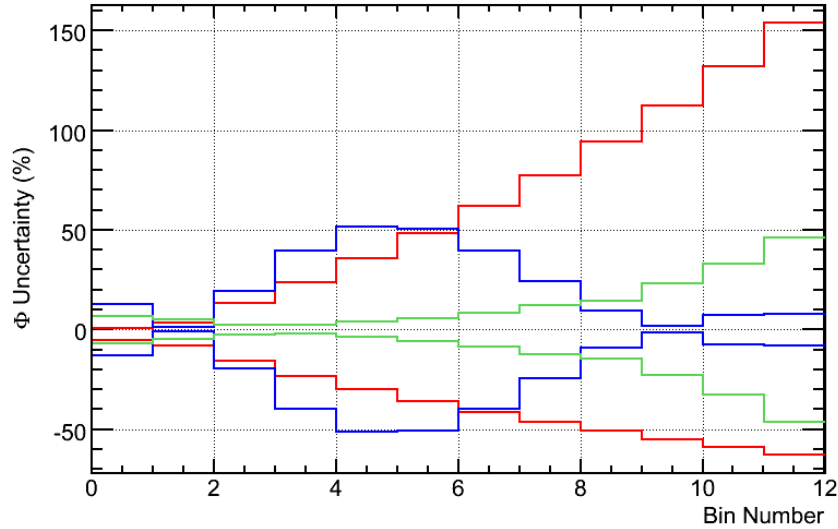


Figure 9.9: Uncertainties in the unfolded result. Blue is the systematic uncertainty implied by anisotropic errors in data/MC comparisons, green is the statistical uncertainty from toy MC studies, and red is the systematic uncertainty due to DOM sensitivity and ice property uncertainties.

A summary of uncertainties in the unfolded result can be seen in Figs. 9.9 and 9.10. In Fig.9.9, blue is the systematic uncertainty implied by anisotropic errors in data/MC comparisons, green is the statistical uncertainty from toy MC studies, and red is the systematic uncertainty due to DOM sensitivity and ice property uncertainties. In Fig.9.10, blue is the systematic uncertainty due to event weighting in simulation, green is the uncertainty due to the choice of regularization parameter, and red is the uniform uncertainty due to miscellaneous errors assumed to be independent of energy. The miscellaneous normalization uncertainties include neutrino cross sections, background contamination, etc., as discussed in Chapter 8.

Comparisons to various flux models are shown in Fig. 9.11, Fig. 9.12, and Fig. 9.13. Fig. 9.11 compares the Honda and Bartol conventional flux models to the

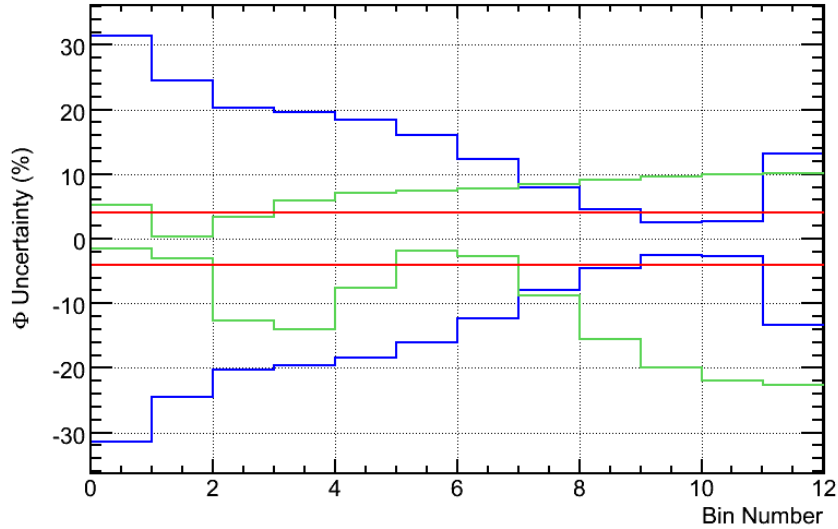


Figure 9.10: Uncertainties in the unfolded result. Blue is the systematic uncertainty due to event weighting, green is the uncertainty due to the choice of regularization parameter, and red is the uniform uncertainty due to miscellaneous errors assumed to be independent of energy.

unfolded results. Fig. 9.12 shows the range of uncertainty in the Sarcevic model as discussed in [66]. Fig. 9.13 looks at various prompt flux models [66, 68, 67].

In order to constrain these various models, the DOM/Ice uncertainties and the anisotropic uncertainties will have to be reduced. Statistical uncertainties will naturally decrease as several years of live time are accumulated for the full IceCube detector. Studies with cosmic ray muons, and with the flashers on each DOM, are being used to improve DOM calibrations and the ice model. Work is also on-going to identify and correct potential problems in simulation that could be contributing to data/simulation mismatch.

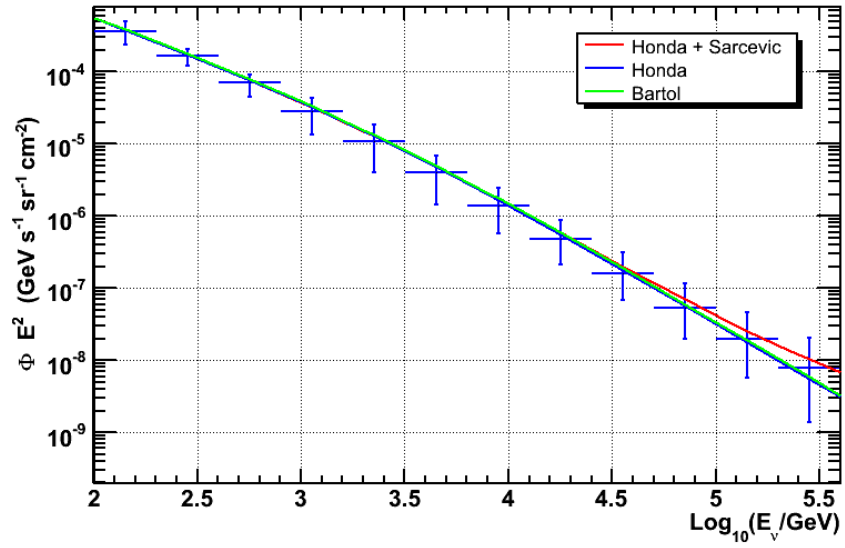


Figure 9.11: Comparison of Honda [17] and Bartol [16] models to unfolded result.

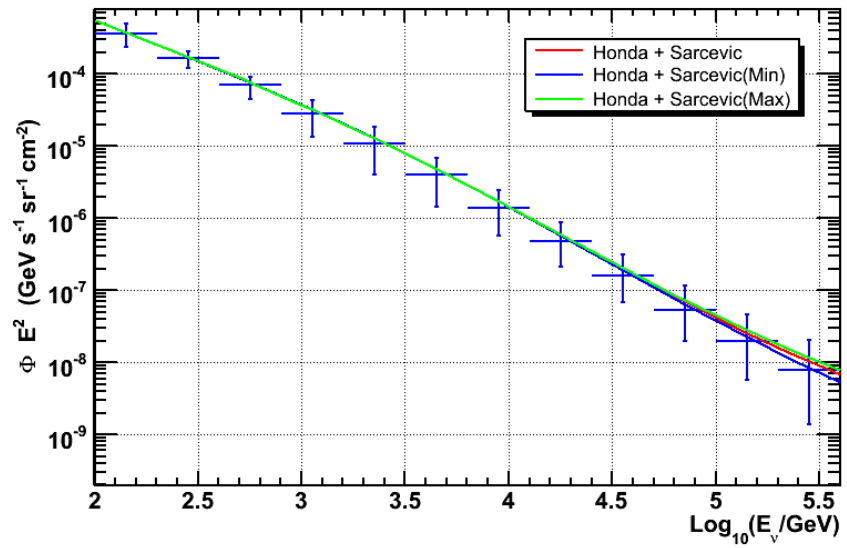


Figure 9.12: Comparison of the minimum and maximum of the Sarcevic [66] prompt flux to unfolded result.

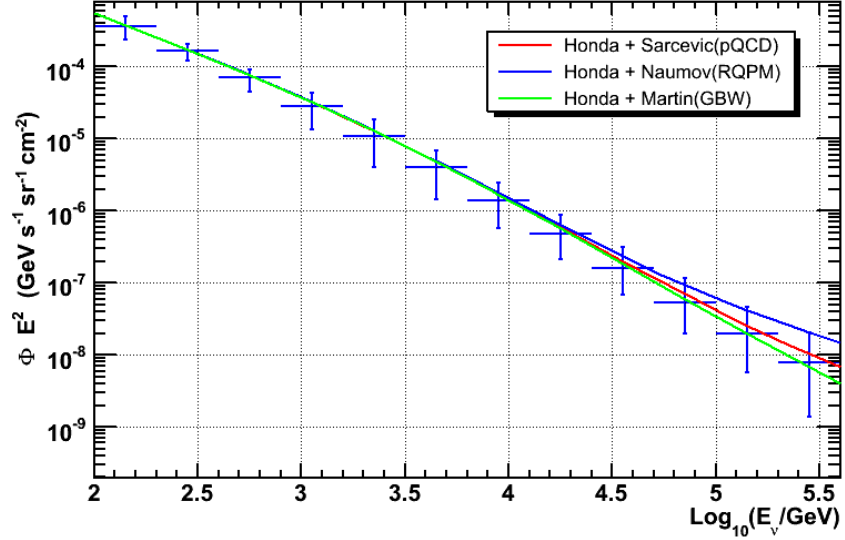


Figure 9.13: Comparison of various prompt flux models to unfolded result. The flux models shown are the Honda flux, plus one of Sarcevic [66], Naumov(RQPM) [68], or Martin(GBW) [67].

9.2 DFT Analysis: Violation of Rotational Invariance

Fig. 9.14 shows the distribution in RA, for events in the final data sample used for the vector model analysis. Fig. 9.15 shows the energy reach of this sample, as predicted by simulation. This data sample contains 7882 events, with declination between -7 and -30° (zenith angle 97 to 120°). Using the data as the input, 10,000 toy experiments were performed to determine whether the data was consistent with the hypotheses of no sidereal signal. For each of the 10,000 tests, the RA of all data events were randomized and the PSDs in modes $n = 1$ through $n = 4$ were computed. The true PSDs for data were then computed and compared to these noise-only distributions. The data was consistent with no signal in any of the modes. In particular, the PSDs for data were less than 34% of the trials for $n = 1$,

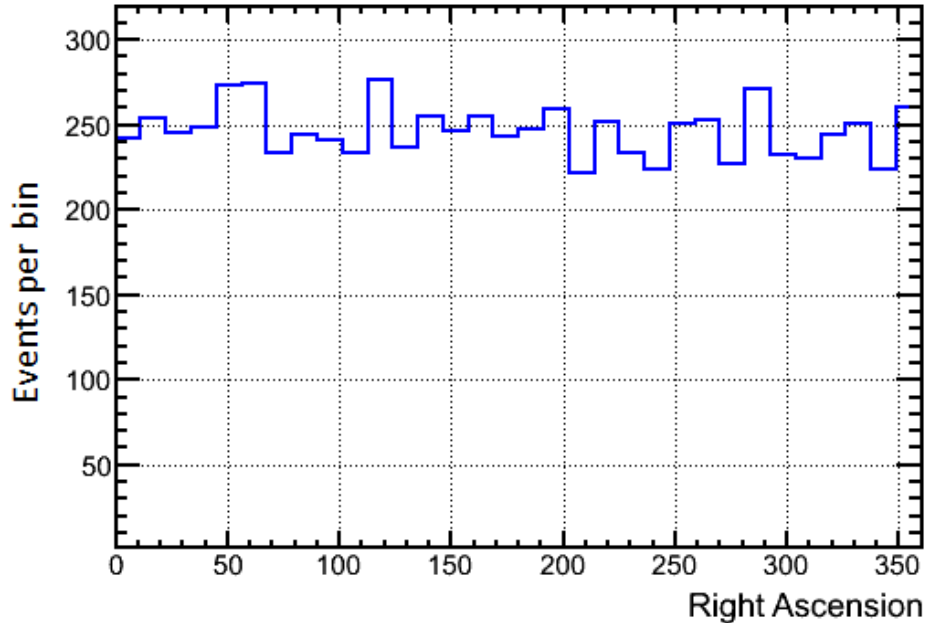


Figure 9.14: RA distribution for events used in the vector model analysis.

92% for $n = 2$, 31% for $n = 3$, and 98% for $n = 4$. The power in even (discrete cosine transforms) and odd (discrete sine transforms) were also checked, with similar results.

Next, 400 trials using simulation were performed to determine the sensitivity to the SME coefficients of the vector model, given the number and distribution of events in the data. The average of each of these trials provided the following limits on the a_L and c_L coefficients, at the 3 sigma level:

$$\begin{aligned}
 a_L^{X(Y)} &< 1.8 \times 10^{-23} \text{GeV}, \\
 c_L^{TX(TY)} &< 3.7 \times 10^{-27}.
 \end{aligned}
 \tag{9.1}$$

We have been able to improve the constraints on these coefficients, by about three and four orders of magnitude, due to the long baseline of atmospheric neutrinos

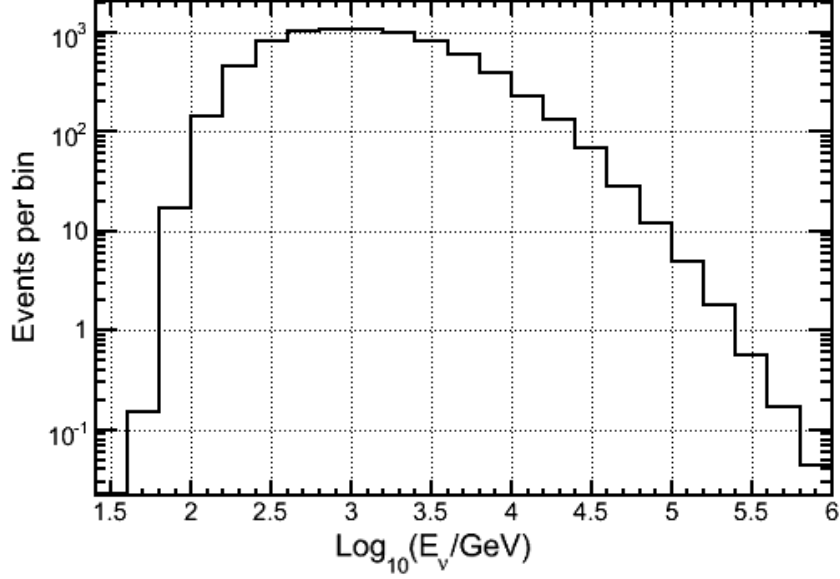


Figure 9.15: Energy reach of the neutrino sample in the vector model analysis, from simulation.

and the high energy reach of IceCube. The limits stated above were determined by varying one coefficient at a time, while keeping the other three fixed at 0. If a_L^X and a_L^Y are equal, and both are contributing to the oscillations, the upper limit is $a_L^X = a_L^Y < 1.3 \times 10^{-23} \text{GeV}$. Similarly, if c_L^{TX} and c_L^{TY} are equal, the upper limit is $c_L^{TX} = c_L^{TY} < 2.7 \times 10^{-27}$.

These upper limits depend on the zenith and energy distribution of atmospheric neutrinos, and are thus affected by uncertainties in these quantities. The impact of the theoretical and experimental uncertainties in the zenith distribution are negligible. Uncertainties in the energy distribution do not affect sensitivity to oscillations driven by the $a_L^{X(Y)}$ coefficients. Uncertainties in the spectral index for atmospheric neutrinos, discussed in Refs. [17, 66], lead to a $\pm 4\%$ change to the

sensitivity for the $c_L^{TX(TY)}$ coefficients, primarily due to uncertainty in the energy distribution of the cosmic ray flux. DOM sensitivity and ice property uncertainties affect the energy dependence of the effective area, and hence the distribution of neutrino energies represented in the data. The specialized simulations with $\pm 10\%$ enhanced photon populations were used to estimate this uncertainty in the energy distribution, in a manner similar to the evaluation of DOM sensitivity and ice property uncertainties for the unfolding analysis. DOM sensitivity and ice property uncertainties lead to a $\pm 11\%$ change in sensitivity to the $c_L^{TX(TY)}$ coefficients. These uncertainties were added in the quadrature, and a net 12% increase (0.4×10^{-27}) has been included in the limits for $c_L^{TX(TY)}$ stated in Eqn. 9.1.

9.3 Likelihood Analyses

9.3.1 Atmospheric Neutrino Spectrum

Fig. 9.16 shows the likelihood ratios for data, for the case where the nuisance parameters for the prompt atmospheric neutrino flux have been promoted to physics parameters. The results of the Feldman-Cousins analysis applied to the likelihood ratios for the prompt flux parameters is shown in Fig. 9.17. The upper limit on the normalization factor is $A_p \sim 2$ at the 90% CL, with little sensitivity to the prompt flux spectral index correction factor. However, this result still suffers from the anomalous systematic uncertainties (previously discussed), which are not accounted for in the remaining nuisance parameters.

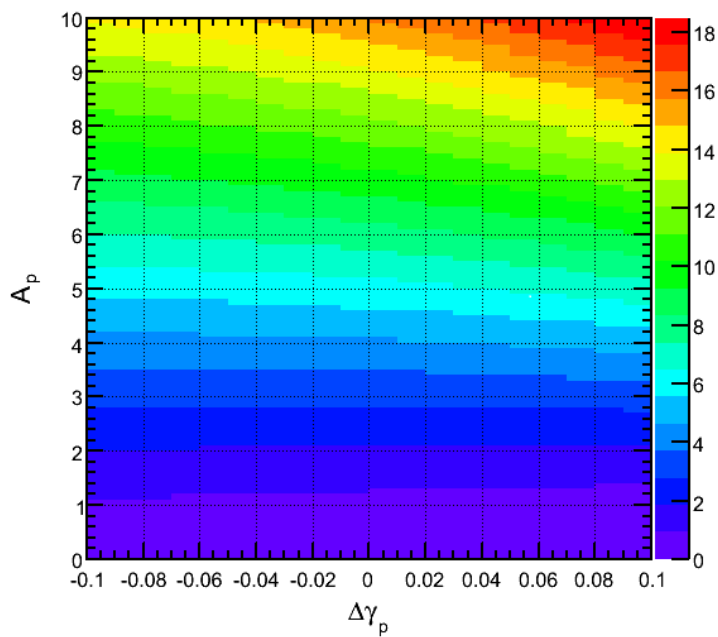


Figure 9.16: Likelihood ratios for data, for the case where the nuisance parameters, A_p and $\Delta\gamma_p$, for the prompt atmospheric neutrino flux have been promoted to physics parameters.

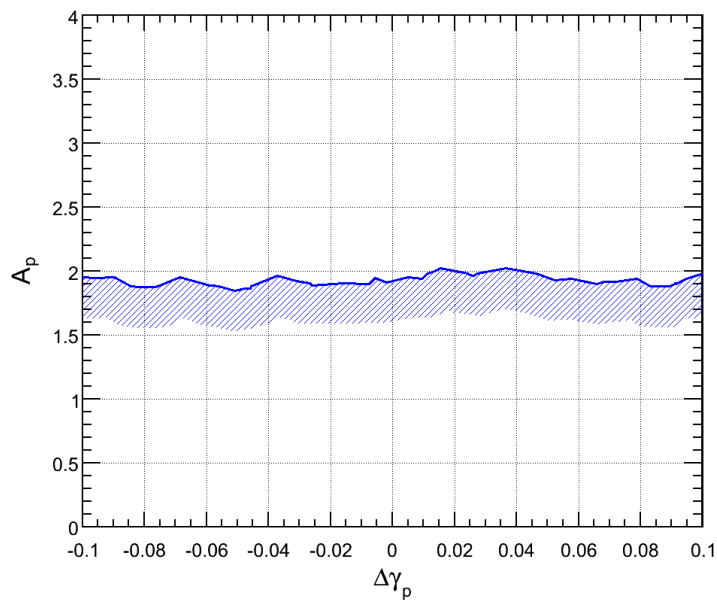


Figure 9.17: The upper limit on the prompt flux normalization factor is $A_p \sim 2$ at the 90% CL, with little sensitivity to the spectral index correction factor for the prompt flux. However, this result still suffers from the anomalous systematic uncertainties (previously discussed), which are not accounted for in the remaining nuisance parameters.

9.3.2 VLI Models

Fig. 9.18 shows the likelihood ratios for data under the $n = 1$ VLI model. Fig. 9.19 shows the same likelihood ratios if the minimum of the prompt flux amplitude is assumed to be 0, rather than 0.56 as stated in Chapter 8. Just from the values of the likelihood ratios, it is apparent that the data rules out the null hypothesis. That is, given the nuisance parameters that have been defined, the data rejects the region of parameter space with no oscillations (bottom and left on the plots). This is because the VLI model improves the fit to the data. Unfortunately, the new physics corrections are improving the fit because the fit based on the standard model and current simulation is a poor fit due to unresolved systematics issues. We can not be certain at this time whether this is a signal of new physics or unaccounted detector systematics. Fig. 9.20 shows the likelihood ratios for the $n = 1$ VLI model as determined using data from the AMANDA-II detector in the dissertation of John Kelley [136]. The best-fit region for the AMANDA analysis covered a very similar part of the parameter space, indicating that it may have been affected by similar systematic uncertainties. However, in that case the null hypothesis was not excluded. The event sample used in the AMANDA analysis contained about 5500 events, from 1387 days of live time over a seven year period from 2000 to 2006. Hence, atmospheric variability may have been averaged out to a greater extent.

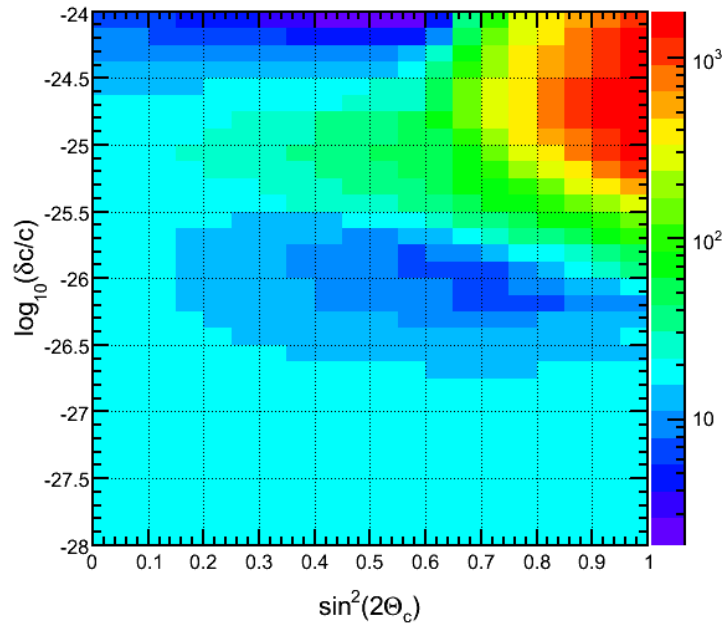


Figure 9.18: Likelihood ratios for data under the $n = 1$ VLI model.

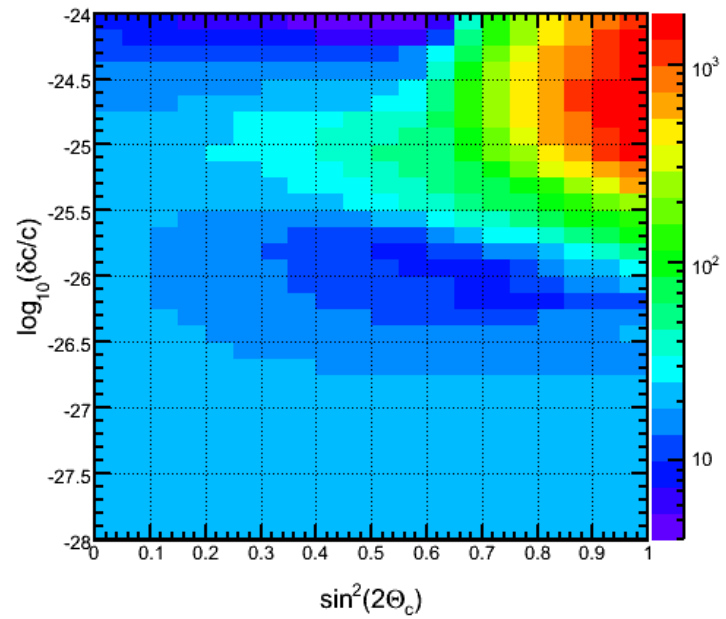


Figure 9.19: Likelihood ratios for data, under the $n = 1$ VLI model. Minimum of the prompt flux amplitude assumed to be 0.

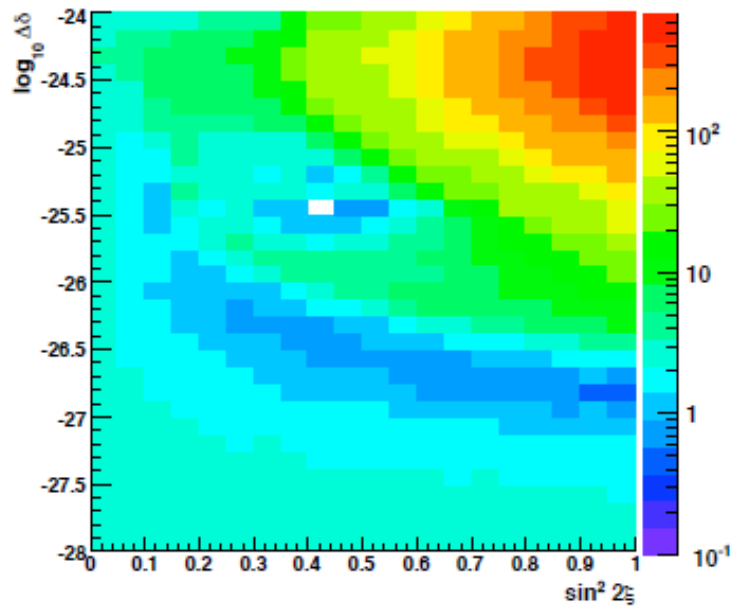


Figure 9.20: Likelihood ratios for the 2000-2006 AMANDA-II data under the $n = 1$ VLI model. The white cell indicates the best fit value. From the dissertation of John Kelley [136].

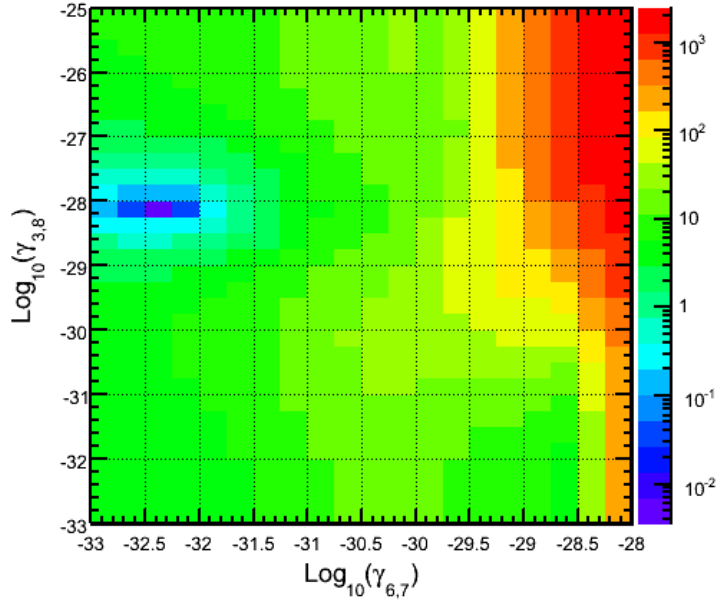


Figure 9.21: Likelihood ratios for data under the $n = 2$ decoherence model.

9.3.3 Decoherence Models

Fig. 9.21 shows the likelihood ratios for data under the $n = 2$ decoherence model. Fig. 9.22 shows the same likelihood ratios if the minimum of the prompt flux amplitude is assumed to be 0. Once again, the sensitivity of the likelihood ratios to the theoretical minimum in the prompt flux can be seen. The results indicated in these plots are also dominated by systematic uncertainties that are not accounted for in the nuisance parameters and we are unable to conclude whether the overall behavior is due to some new physics or unresolved systematics.

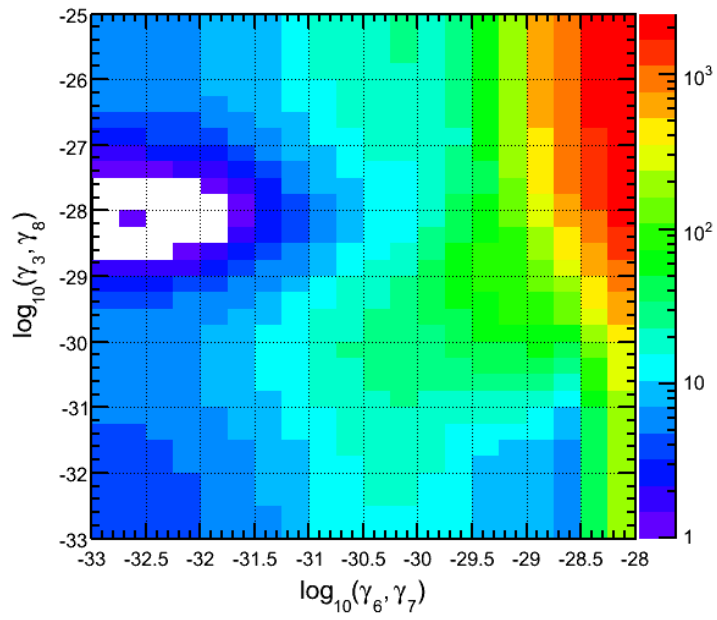


Figure 9.22: Likelihood ratios for data, under the $n = 2$ decoherence model. Minimum of the prompt flux amplitude assumed to be 0.

Chapter 10

Conclusions and Outlook

10.1 Summary of Results

An unfolding of the atmospheric muon neutrino flux, from 100 GeV to 400 TeV, was successfully performed. Estimates of statistical and systematic errors on the result were determined. This unfolding result is interesting due to the high-energy reach, however uncertainties will need to be reduced before various flux models can be constrained. Uncertainties in DOM sensitivity and ice property measurements can be reduced using atmospheric muons and the DOM flashers. Also, once simulation of light propagation in the ice has been improved, it should be possible to use a more sophisticated method for estimating the impact of ice model uncertainties, obtaining a more accurate and perhaps smaller estimate of the induced errors. It may also be possible to account for anisotropic variations in the neutrino flux, due to regional and temporal variations in the atmospheric temperature profile, by rescaling simulation using energy and zenith-dependent correlation factors and in situ meteorological data.

A DFT analysis of the RA dependence of the atmospheric neutrino flux was performed. The results were consistent with no sidereal modulation. In the context of the SME and the vector model, constraints on certain Lorentz and CPT-violating coefficients were improved by about three and four orders of magnitude.

A likelihood analysis was developed to search for small perturbations in the energy and zenith dependence of the atmospheric neutrino flux, such as predicted by various phenomenological models of new physics. Systematic uncertainties, and their impact on this type of analysis, were evaluated. Important systematic disagreements between data and simulation have to be resolved before the likelihood analysis can be used to constrain these models. These disagreements include an excess of near-horizontal events in the data, and systematic zenith and energy dependent disagreements that may be due, at least in part, to local and temporal atmospheric variability. It may be necessary to consider energy-dependent or zenith-dependent nuisance parameters.

In addition to accounting for atmospheric variability, other changes or improvements to simulation are needed. In particular, the inability to reproduce the COG dependence of horizontal events indicates that the layered ice properties may be getting smeared out in simulation. Better simulation for light propagation in the detector is likely needed, and a possible alternative to Photonics is being developed and tested by various members of the Collaboration. Additionally, more accurate modelling of the production of the horizontal flux may be necessary, as well as closer examination of the assumption that the up-going atmospheric neutrino flux in IceCube is a mirror of the down-going atmospheric neutrino flux.

10.2 Future Prospects and Refinements to the Methodology

Improvements to the event selection are certainly possible. However, BDT event selection should play a leading role in IceCube analyses, particularly atmospheric neutrino and diffuse flux analyses. While quite a bit of work went in to optimizing the cuts and the BDT configuration for this analysis, the optimal configuration has likely not been found yet. Also, with the addition of more strings, and new reconstruction algorithms that are being created, refinements and improvements to this BDT configuration are likely possible.

Once the systematic issues discussed above are resolved, the likelihood analysis should be revisited. Several years of data from the full 86-string detector will improve the averaging of seasonal variations, as well as reduce the statistical uncertainties for the likelihood analysis and the unfolding analysis. It should be possible to extend the unfolding to about 10^5 TeV, and reduce the uncertainties to a level where different flux models can be constrained.

Bibliography

- [1] V.A. Kostelecky, *arXiv:hep-ph/0403088*.
- [2] V.A. Kostelecky and S. Samuel, *Phys. Rev. D* **39**, 683 (1989).
- [3] J.R. Ellis, N.E. Mavromatos, and D.V. Nanopoulos, *arXiv:gr-qc/9909085*.
- [4] R. Gambini and J. Pullin, *Phys. Rev. D* **59**, 124021 (1999).
- [5] M.R. Douglas and N.A. Nekrasov, *Rev. Mod. Phys.* **73**, 977 (2001).
- [6] S.W. Hawking, *Commun. Math. Phys.*, **87**, 395 (1982).
- [7] N. E. Mavromatos, *arXiv:hep-ph/0402005*.
- [8] N. E. Mavromatos, *arXiv:gr-qc/0407005*.
- [9] L. Randall and R. Sundrum, *Phys. Rev. Lett.* **83**, 17 (1999).
- [10] F. Reines and C.L. Cowan, *Phys. Rev.* **92**, 830 (1953); C.L. Cowan *et al.*, *Science* **124**, 103 (1956).
- [11] F. Reines *et al.*, *Phys. Rev. Lett.* **15**, 429 (1965).
- [12] C.V. Achar *et al.*, *Phys. Lett.* **18**, 196 (1965).
- [13] Y. Fukuda *et al.*, *Phys. Rev. Lett.* **81**, 1562 (1998).
- [14] M.C. Sanchez *et al.*, *Phys. Rev. D* **68**, 113004 (2003).
- [15] M. Ambrosio *et al.*, *Phys. Lett. B* **517**, 59 (2001).
- [16] G.D. Barr *et al.*, *Phys. Rev. D.*, **70**, 023006 (2004).
- [17] M. Honda *et al.*, *Phys. Rev. D.*, **75**, 043006 (2007).
- [18] S. Coleman and S.L. Glashow, *Phys. Lett. B* **405**, 249 (1997).
- [19] S.L. Glashow *et al.*, *Phys. Rev. D* **56**, 2433 (1997).

- [20] S.L. Glashow, *arxiv:hep-ph/0407087*.
- [21] D. Colladay and V.A. Kostelecky, *Phys. Rev. D* **55**, 6760 (1997).
- [22] S. Coleman and S.L. Glashow, *Phys. Rev. D* **59**, 116008 (1999).
- [23] V.D. Barger *et al.*, *Phys. Rev. Lett.* **85**, 5055 (2000).
- [24] M. Gasperini, *Phys. Rev. D* **38**, 2635 (1988).
- [25] M. Gasperini, *Phys. Rev. D* **39**, 3606 (1989).
- [26] A. Halprin and C.N. Leung, *Phys. Rev. Lett.* **67**, 1833 (1991).
- [27] G.Z. Adunas, E. Rodriguez-Milla, and D.V. Ahluwalia, *Phys. Lett. B.* **485**, 215 (2000).
- [28] A. Karle, *arXiv:0812.3981*.
- [29] F. Halzen and D. Hooper, *Rep. Prog. Phys.* **65**, 1025 (2002).
- [30] IceCube official website, <http://www.icecube.wisc.edu>.
- [31] M.C. Gonzalez-Garcia, F. Halzen and M. Maltoni, *Phys. Rev. D.*, **71**, 093010 (2005).
- [32] D. Colladay and V.A. Kostelecky, *Phys. Rev. D* **58**, 116002 (1998).
- [33] W.C. Haxton and B.R. Holstein, *Am. J. Phys.* **68**, 15 (2000).
- [34] W.C. Haxton and B.R. Holstein, *Am. J. Phys.* **72**, 18 (2004).
- [35] W. Grimus, *arXiv:hep-ph/0307149*.
- [36] B. Kayser, *arXiv:0804.1121*.
- [37] E. Kh. Akhmedov, *arXiv:0905.1903*.
- [38] A. de Gouvea, *arXiv:hep-ph/0503086* and *hep-ph/0411274*.
- [39] A. de Gouvea, *arXiv:0902.4656*.

- [40] R.N. Mohapatra, S. Nasri, and Hai-Bo Yu, *Phys. Rev. D* **72**, 033007 (2005).
- [41] J.N. Bahcall, H. Murayama, and C. Pena-Garay, *Phys. Rev. D* **70**, 033012 (2004).
- [42] K. Abe *et al.*, *arXiv:hep-ex/0607059*.
- [43] G.L. Fogli *et al.*, *arXiv:0805.2517*.
- [44] C. Giunti and C.W. Kim, *Fundamentals of Neutrino Physics and Astrophysics* (Oxford University Press, New York, 2007).
- [45] P. Lipari, *Astropart. Phys.* **14**, 153 (2000).
- [46] J. Favier, R. Kossakowski, and J.P. Vialle, *Phys. Rev. D* **68**, 093006 (2003).
- [47] R.N. Mohapatra, *New J. of Phys.* **6**, 82 (2004).
- [48] G. Barenboim and N.E. Mavromatos, *Phys. Rev. D* **70**, 093015 (2004).
- [49] V.A. Kostelecky and M. Mewes, *Phys. Rev. D.*, **69**, 016005 (2004).
- [50] V.A. Kostelecky and M. Mewes, *Phys. Rev. D.*, **70**, 076002 (2004).
- [51] V.A. Kostelecky and M. Mewes, *Phys. Rev. D.*, **70**, 031902 (2004).
- [52] V.A. Kostelecky and M. Mewes, *arXiv:0801.0287*.
- [53] C. Amsler *et al.* (Particle Data Group), *Physics Letters* **B667**, 1 (2008).
- [54] R. Abbasi, P. Desiati, and J.C. Diaz Velez, *Proc. of the 31st ICRC*, Łódź (2009).
- [55] A. Hillas, *arXiv:astro-ph/0607109*.
- [56] F. Halzen, A. Kappes, and A. O Murchadha, *arXiv:0803.0314*.
- [57] T.K. Gaisser, *Cosmic Rays and Particle Physics* (Cambridge University, U.K., 1991).
- [58] J.R. Hoerandel, *Astropart. Phys.* **21**, 241 (2004).
- [59] B. Louis *et al.*, *Los Alamos Sci.* **25**, 16 (1997).

- [60] T.K. Gaisser and M. Honda, *Annu. Rev. Nucl. part. Sci.* **52**, 153 (2002).
- [61] S. Tilav *et al.*, *Proc. of the 31st ICRC*, Łódź (2009).
- [62] M. Ackermann and E. Bernardini *Proc. of the 29th ICRC*, Pune, (2005).
- [63] C.G.S. Costa, *Astropart. Phys.* **16**, 193 (2001).
- [64] J. Ahrens *et al.*, *IceCube Project Preliminary Design Document* Available at <http://icecube.wisc.edu>.
- [65] T.K. Gaisser, *arXiv:hep-ph:0209195*.
- [66] R. Enberg, M.H. Reno and I. Sarcevic, *Phys. Rev. D.*, **78**, 043005 (2008).
- [67] A.D. Martin, M.G. Ryskin and A.M. Stasto, *Acta Phys. Polon. B*, **34**, 3273 (2003).
- [68] G. Fiorentini, A. Naumov and F.L. Villante, *Phys. Lett. B*, **510**, 173 (2001).
- [69] J. Ahrens, *et al.*, *Astropart. Phys.* **20**, 507 (2004).
- [70] G. Amelino-Camelia, *arxiv:gr-qc/0309054*.
- [71] J. Alfaro, H. Morales-Tecotl, and F. Urrutia, *Phys. Rev. Lett.* **84**, 2318 (2000).
- [72] R. Brustein, D. Eichler, and S. Foffa, *Phys. Rev. D* **65**, 105006 (2002).
- [73] A. Halprin and H.B. Kim, *Phys. Lett. B* **469**, 78 (1999).
- [74] G. Battistoni *et al.*, *Phys. Lett. B* **615**, 14 (2005).
- [75] G.L. Fogli, *et al.*, *Phys. Rev. D* **60**, 053006 (1999).
- [76] M.C. Gonzalez-Garcia and M. Maltoni, *Phys. Rev. D.*, **70**, 033010 (2004).
- [77] R. Abbasi *et al.*, *Phys Rev D* **79**, 102005 (2009).
- [78] S.W. Hawking, *Nucl. Phys. B*, **144**, 349 (1978).
- [79] S.W. Hawking, *Phys. Rev. D*, **53**, 3099 (1996).

- [80] G. Lindblad, *Commun. Math. Phys.* **48**, 119 (1976).
- [81] L. Anchordoqui and F. Halzen, *Annals Phys.*, **321**, 2660 (2006).
- [82] A.M. Gago *et al.*, *arXiv:hep-ph/0208166*.
- [83] G. Barenboim *et al.*, *Nucl. Phys. B.* **758** 90 (2006).
- [84] J. Ellis, N. E. Mavromatos, and D. V. Nanopoulos, *Mod. Phys. Lett. A* **12**, 1759 (1997).
- [85] J. Ellis *et al.*, *Mod. Phys. Lett. A* **12**, 243 (1997).
- [86] E. Lisi, A. Marrone, and D. Montanino, *Phys. Rev. Lett.* **85**, 1166 (2000).
- [87] L.B. Auerbach *et al.*, *Phys. Rev. D* **72**, 076004 (2005).
- [88] P. Adamson *et al.*, *Phys. Rev. Lett.*, **101**, 151601 (2008).
- [89] G. Karagiorgi *et al.*, *arXiv:0906.1997*.
- [90] M. Mewes, *arXiv:hep-ph/0409344*.
- [91] M.D. Messier, in V.A. Kostelecky, ed., *CPT and Lorentz Symmetry III*, World Scientific, Singapore (2005).
- [92] L.A. Anchordoqui, *et al.*, *arXiv:hep-ph/0506168*.
- [93] J. Christian, *arXiv:gr-qc/0409077*.
- [94] F. Halzen, *arXiv:astro-ph/0602132*.
- [95] A. Achterburg *et al.*, *arXiv:astro-ph/0509330*.
- [96] R. Abbasi *et al.*, *arXiv:0805.2517*.
- [97] A. Achterberg, *et al.*, *Astropart. Phys.* **26**, 155 (2006).
- [98] P.B. Price, K. Woschnagg, and D. Chirkin, *Geophys. Res. Lett.* **27**, (14) 2129 (2000).
- [99] M. Ackermann *et al.*, *J. of Geophys. Res.* **111**, D13203 (2006).

- [100] P.B. Price and L. Bergstrom, *Appl. Opt.* **36**, (18) 4181 (1997).
- [101] P. Askebjør *et al.*, *Appl. Opt.* **36**, (18) 4168 (1997)
- [102] N.E. Bramall *et al.*, *Geophys. Res. Lett.* **32**, L21815 (2005).
- [103] R. Gandhi *et al.*, *Phys. Rev. D* **58**, 093009 (1998).
- [104] H.L. Lai *et al.*, *Eur. Phys. J. C*, **12**, 375 (2000).
- [105] M.H. Reno, *arXiv:hep-ph/0410109*.
- [106] M.H. Reno, *arXiv:hep-ph/0412412*.
- [107] S. Eidelman *et al.*, *Phys. Lett. B* **592**, 252 (2004).
- [108] J.F. Beacom, P. Crotty, and E.W. Kolb, *Phys. Rev. D* **66**, 021302 (2002).
- [109] J. Ahrens *et al.*, *Nucl. Instr. and Meth. A* **524**, 169 (2004).
- [110] N. van Eijndhoven, O. Fadiran, and G. Japaridze, *arXiv:0704.1706*.
- [111] D. Pandel, *Diploma Thesis*, Humboldt-Universität zu Berlin, Berlin, 1996.
- [112] CERN, ROOT, 1994, <http://root.cern.ch>.
- [113] S. Grullon, D. Boersma, and G. Hill, *Photonics-based Log-Likelihood Reconstruction in IceCube*, IceCube Internal Report 200807001.
- [114] T. Neunhoffer, *Astropart. Phys.* **25**, 220, (2006).
- [115] P.A. Toale, *arXiv:astro-ph/0607003*.
- [116] D. Heck *et al.*, *CORSIKA: A Monte Carlo Code to Simulate Extensive Air Showers* (Wissenschaftliche Berichte FZKA 6019; Karlsruhe: Forschungszentrum Karlsruhe) (1998).
- [117] J. Ranft, *arXiv:hep-ph/9911232*.
- [118] E. Ahn *et al.*, *arXiv:hep-ph/0906.4113*.
- [119] D. Chirkin and W. Rhode, *arXiv:hep-ph/0407075*.

- [120] M Kowalski and A. Gazizov, *arXiv:astro-ph/0312202*.
- [121] A. Dziewonski in *The Encyclopedia of Solid Earth Geophysics*, edited by D.E. James (Van Nostrand Reinhold, New York, 1989), p. 331.
- [122] J. Lundberg *et al.*, *arXiv:astro-ph/0702108*.
- [123] A. Hoecker *et al.*, *arXiv:physics/0703039*.
- [124] R. Brun and F. Rademakers, *Phys. Res. A*, **389**, 81 (1997).
- [125] G.J. Feldman and R.D. Cousins, *Phys. Rev. D.*, **57**, 3873 (1998).
- [126] G.J. Feldman, "Multiple measurements and parameters in the unified approach," Workshop on Confidence Limits, Fermilab (2000).
- [127] K. Cranmer, in *Statistical Problems in Particle Physics, Astrophysics and Cosmology: Proceedings of PHYSTAT05*, L. Lyons and M. Ünel, eds., (Univ. of Oxford, U.K., 2005); *arXiv:physics/0511028*.
- [128] A. Hoecker and V. Kartvelishvili, *Nucl. Inst. Meth. A* **372**, 469 (1996).
- [129] RooUnfold: ROOT Unfolding Framework, [http:// hep-unx.rl.ac.uk/ adye/software/unfold/RooUnfold.html](http://hep-unx.rl.ac.uk/adye/software/unfold/RooUnfold.html).
- [130] T.K. Gaisser, *et al.*, *Proc. of 27th ICRC* (Hamburg) **1**, 1643 (2001).
- [131] A. Achterberg, *et al.*, *Phys. Rev. D* **75**, 102001 (2007).
- [132] T. Sanuki, *et al.* *Phys. Rev. D* **75**, 043005 (2007).
- [133] T. Han and D. Hooper, *New J. of Phys.* **6**, 150 (2004).
- [134] J. Alvarez-Muniz *et al.*, *Phys. Rev. Lett.* **88**, 021301 (2002).
- [135] L.A. Anchordoqui, J.L. Feng, and H. Goldberg, *Phys. Rev. Lett.* **96**, 021101 (2006).
- [136] J. Kelley, PhD Thesis, *Searching for Quantum Gravity with High Energy Atmospheric Neutrinos and AMANDA-II*, (2008).
- [137] I. Sarcevic, *arXiv:hep-ph/0508002*.